ADVANCED STEEL CONSTRUCTION

An International Journal

Volume 7 Number 3

September 2011

CONTENTS

Technical Papers

Website: *http://www.hkisc.org*
ISSN 1816-112X
Science Citation Index Expanded, Materials Science Citation Index and ISI Alerting

Cover: Hong Kong Design Institute

ADVANCED STEEL CONSTRUCTION

VOL.7, NO.3 (2011)

ADVANCED STEEL CONSTRUCTION

an International Journal

ISSN 1816-112X

Volume 7 Number 3 *September 2011*

ISSN 1816-112X

Science Citation Index Expanded, Materials Science Citation Index and ISI Alerting

Advanced Steel Construction
an international journal

Cover: Hong Kong Design Institute

General Information
Advanced Steel Construction, an international journal

Aims and scope

The International Journal of Advanced Steel Construction provides a platform for the publication and rapid dissemination of original and up-to-date research and technological developments in steel construction, design and analysis. Scope of research papers published in this journal includes but is not limited to theoretical and experimental research on elements, assemblages, systems, material, design philosophy and codification, standards, fabrication, projects of innovative nature and computer techniques. The journal is specifically tailored to channel the exchange of technological know-how between researchers and practitioners. Contributions from all aspects related to the recent developments of advanced steel construction are welcome.

Instructions to authors

Submission of the manuscript. Authors may submit double-spaced manuscripts preferably in MS Word by emailing to one of the chief editors as follows for arrangement of review. Alternatively papers can be submitted on a diskette to one of the chief editors.

Asian Pacific , African and organizing editor : Professor S.L. Chan, Email: ceslchan@polyu.edu.hk
American editor : Professor W.F. Chen, Email: waifah@hawaii.edu
European editor : Professor R. Zandonini, Email: riccardo_zandonini@ing.unitn.it

All manuscripts submitted to the journal are recommended to accompany with a list of four potential reviewers suggested by the author(s). This list should include the complete name, address, telephone and fax numbers, email address, and at least five keywords that identify the expertise of each reviewer. This scheme will improve the process of review.

Style of manuscript

General. Author(s) should provide full postal and email addresses and fax number for correspondence. The manuscript including abstract, keywords, references, figures and tables should be in English with pages numbered and typed with double line spacing on single side of A4 or letter-sized paper. The front page of the article should contain:

a) a short title (reflecting the content of the paper);
b) all the name(s) and postal and email addresses of author(s) specifying the author to whom correspondence and proofs should be sent;
c) an abstract of 100-200 words; and
d) 5 to 8 keywords.

The paper must contain an introduction and a conclusion. The length of paper should not exceed 25 journal pages (approximately 15,000 words equivalents).

Tables and figures. Tables and figures including photographs should be typed, numbered consecutively in Arabic numerals and with short titles. They should be referred in the text as Figure 1, Table 2, etc. Originally drawn figures and photographs should be provided in a form suitable for photographic reproduction and reduction in the journal.

Mathematical expressions and units. The Systeme Internationale (SI) should be followed whenever possible. The numbers identifying the displayed mathematical expression should be referred to in the text as Eq. (1), Eq. (2).

References. References to published literature should be referred in the text, in the order of citation with Arabic numerals, by the last name(s) of the author(s) (e.g. Zandonini and Zanon [3]) or if more than three authors (e.g. Zandonini et al. [4]). References should be in English with occasional allowance of 1-2 exceptional references in local languages and reflect the current state-of-technology. Journal titles should be abbreviated in the style of the Word List of Scientific Periodicals. References should be cited in the following style [1, 2, 3].

Journal: [1] Chen, W.F. and Kishi, N., "Semi-rigid Steel Beam-to-column Connections, Data Base and Modelling", Journal of Structural Engineering, ASCE, 1989, Vol. 115, No. 1, pp. 105-119.
Book: [2] Chan, S.L. and Chui, P.P.T., "Non-linear Static and Cyclic Analysis of Semi-rigid Steel Frames", Elsevier Science, 2000.
Proceedings: [3] Zandonini, R. and Zanon, P., "Experimental Analysis of Steel Beams with Semi-rigid Joints", Proceedings of International Conference on Advances in Steel Structures, Hong Kong, 1996, Vol. 1, pp. 356-364.

Proofs. Proof will be sent to the corresponding author to correct any typesetting errors. Alternations to the original manuscript at this stage will not be accepted. Proofs should be returned within 48 hours of receipt by Express Mail, Fax or Email.

Copyright. Submission of an article to "Advanced Steel Construction" implies that it presents the original and unpublished work, and not under consideration for publication nor published elsewhere. On acceptance of a manuscript submitted, the copyright thereof is transferred to the publisher by the Transfer of Copyright Agreement and upon the acceptance of publication for the papers, the corresponding author must sign the form for Transfer of Copyright.

Permission. Quoting from this journal is granted provided that the customary acknowledgement is given to the source.

Page charge and Reprints. There will be no page charges if the length of paper is within the limit of 25 journal pages. A total of 30 free offprints will be supplied free of charge to the corresponding author. Purchasing orders for additional offprints can be made on order forms which will be sent to the authors. These instructions can be obtained at the Hong Kong Institute of Steel Construction, Journal website: http://www.hkisc.org

The International Journal of Advanced Steel Construction is published quarterly by non-profit making learnt society, The Hong Kong Institute of Steel Construction, c/o Department of Civil & Structural Engineering, The Hong Kong Polytechnic University, Hung Hom, Kowloon, Hong Kong.

Subscription inquiries and change of address. Address all subscription inquiries and correspondence to Member Records, IJASC. Notify an address change as soon as possible. All communications should include both old and new addresses with zip codes and be accompanied by a mailing label from a recent issue. Allow six weeks for all changes to become effective.

The Hong Kong Institute of Steel Construction
HKISC
c/o Department of Civil and Structural Engineering,
The Hong Kong Polytechnic University,
Hunghom, Kowloon, Hong Kong, China.
Tel: 852- 2766 6047 Fax: 852- 2334 6389
Email: *ceslchan@polyu.edu.hk* Website: *http://www.hkisc.org/*
ISSN 1816-112X
Science Citation Index Expanded, Materials Science Citation Index and ISI Alerting

ISSN 1816-112X

Science Citation Index Expanded, Materials Science Citation Index and ISI Alerting

Advanced Steel Construction
an international journal

VOLUME 7 NUMBER 3 SEPTEMBER 2011

Technical Papers

BEARING CAPACITY AND ENERGY ABSORPTION CHARACTERISTICS OF THIN-WALLED CIRCULAR STEEL TUBE AND ITS APPLICATION IN RETRACTABLE ROOF STRUCTURES

Qinghua Han[1,2,*] , Yan Lu [1], Zemin Xu [1] and Yafei Chang[1]

[1]*School of Civil Engineering，Tianjin University，Tianjin 300072，China*
[2]*Key Laboratory of Coast Structure Safety (Tianjin University), Ministry of Education，Tianjin 300072，China*
**(Corresponding author: E-mail: qhhan@tju.edu.cn)*

Received: 2 August 2010; Revised: 10 November 2010; Accepted: 25 February 2011

ABSTRACT: This paper presents an experimental task in which the specimens are either single thin-walled circular stainless steel tubes or a honeycomb structure. The honeycomb structure is made up of the tubes with 4 configurations. Compressive loads are applied and deformations are recorded. The numerical and analytical analyses are also carried out with respect to the bearing capacity and energy absorption characteristics. It is shown that the average bearing capacity of single thin-walled circular steel tubes is lower than those tubes arranged in a honeycomb structure. The configuration of staggered thin-walled circular steel tubes with *R/t* values between 20 and 30 exhibits good bearing capacity. The configuration of aligned thin-walled circular steel tubes of *R/t* values between 30 and 45 exhibits good energy absorbing characteristic. The results obtained in this paper may be useful in designing a steel retractable roof structure with respect to passive collision protection.

Keywords: Thin-walled circular steel tube, Honeycomb structure, Bearing capacity, Energy absorption, Aligned configuration, Staggered configuration

1. INTRODUCTION

Many researches on the thin-walled circular tube under different loads were conducted. Abrahamson [1] firstly studied the dynamic plastic flow buckling of a cylindrical shell from uniform radial impulse procedures. And the radical impact experiment of the single cylindrical shell was carried out. The buckling wave shape was observed. His finding is buckling modal number and critical impact velocity which fit the experimental results. Lindberg [2] made further research on the dynamic plastic flow buckling of a cylindrical shell from uniform radial impulse procedures considering the strain rate influence. The buckling modal number of the cylindrical shell was further studied. Selecting aluminum spherical shells of *R/t* values between 15 and 240 axially compressed, Gupta et al. [3-4] drew the load-compression and energy-compression curves and determined the mean collapse loads. They found a simple analytical model which matched well with the experimental results. Ru and Wang et al. exploration on the plastic buckling of a cylindrical shell under radial impulse load by the energy principle acquired the equation of the critical impact velocity [5]. Gu and Liu [6] presented the assumed energy of the displacement field to study the dynamic plastic buckling of a cylindrical shell fixed at both ends under impulse load. Their conclusion is that fixed boundary condition makes plastic buckling stronger than the free boundary condition. Zeng et al. [7] conducted a series of experiment on thin-wall circular steel tube under shock wave. They acquired the modal solution based on the principle of the virtual velocity. It reports that the deformation of steel tubes are controlled by changing the material hardening, layer and inertia. Gu [8] and Du et al. [9] also conducted the experimental research and theoretical analysis about the deformation and energy absorption characteristics of multi-row cylindrical shell under explosion and shock waves, which serves as the analytical method for this paper.

At present, thin-walled circular tubes have many applications. Thin-walled circular tubes may be applied in long-span space structure design. Retractable roof structure is an advanced long-span space structure. Compared with the traditional structures, retractable roof structure is a moving system, which can be used in partially or entirely open or closed conditions. The research on the retractable roof structure is only about design principle, load, load combination and so on. Zhang and Liu [10] firstly summarized the developing trend of retractable roof structure and put forward the retractable principle and methods based on the architecture plane projection and elevation. Then Guan et al. [11] presented wire-driven track system and explained the differences of the load value and load combination between the retractable roof structure and traditional structure. Ishii [12] introduced the basic concept of retractable roof structure and building function. Then the typical construction examples are introduced. When retractable roof structure is moving，it may cause collision accidents. There is few research on the collision mechanism and passive safety protection. Passive safety protection [13] aims at reducing the damage after the collision accidents of movable elements, avoiding the casualties. And the relevant technique contains crashworthy design, personal evacuation and rescue.

The application of thin-walled circular steel tube in designing a steel retractable roof structure is discussed with respect to passive collision protection. In this paper，thin-walled circular stainless steel tube of D values between 19mm and 51mm and t values between 0.3mm and 1.4mm are selected for the research. The main mechanical parameters are shown in Table 1. An experimental task was presented in which the specimens are either single thin-walled circular stainless steel tubes or a honeycomb structure. The honeycomb structure is made up of the tubes with 4 configurations. Compressive loads were applied and deformations are recorded. The numerical and analytical analyses are also carried out with respect to the bearing capacity and energy absorption characteristics. The given numerical simulation aims at verifying the experimental results.

Table 1. Mechanical Properties of the Thin-walled Circular Steel Tube

Material	Elastic Modulus (GPa)	Yield Stress (MPa)	Density (kg/m^3)
Stainless Steel	190	347	7850

2. ANALYSIS OF THE THIN-WALLED CIRCULAR TUBE UNDER STATIC COMPRESSION

2.1 Ultimate Internal Forces of Single Circular Tube under Two-way Symmetrical Compression

Two-way symmetrical compression is the basic form for thin-walled circular tube. The corresponding simplified model is shown in Figure 1(a). [8]

Under static load, single tube under two-way symmetrical compression is a hyperstatic structure with three redundances. Based on the symmetry, a quarter of the structure is extracted , which is a hyperstatic structure with one redundance (Figure 1 (b)). The basic structure is a curved beam. In polar coordinate system, by the method of forces the final moment is shown as

$$M(\alpha) = FR(\frac{1}{\pi} - \frac{\sin\alpha}{2}) \tag{1}$$

When $\alpha = \frac{\pi}{2}$， $M(\frac{\pi}{2}) = (\frac{1}{\pi} - \frac{1}{2})FR = -0.182FR$ (2)

When $\alpha = 0$, $M(0) = \frac{FR}{\pi} = 0.318FR$. (3)

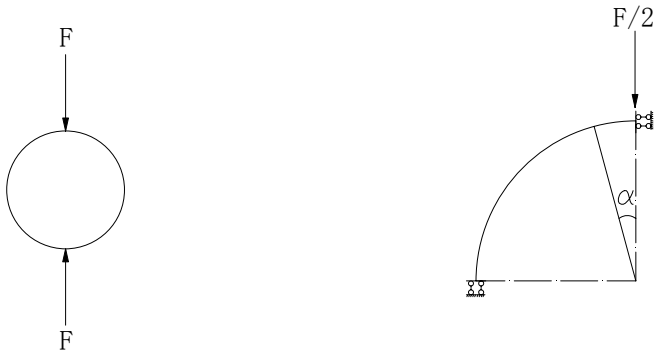

(a) Simplified Model (b) Hyperstatic Structure with One Redundance

Figure 1. Internal Forces of Single Circular Tube under Two-way Symmetrical Compression

In the compression course，there are four plastic hinges where $\alpha = 0$， $\alpha = \frac{\pi}{2}$ and the symmetrical points. The first plastic hinge appears at the point of $\alpha = 0$，which makes the tube deforming as the shape of dumbbell. This mechanical behavior leads to the failure form of four plastic hinges.

According to the formula for calculating the maximum bending stress

$$\sigma_{\max} = \frac{M_{\max}}{W} \tag{4}$$

For the rectangular section,

$$W = \frac{Lt^2}{6} \tag{5}$$

Putting Eq. 3 and Eq. 5 into Eq. 4 ,

$$F = \frac{L\sigma_{\max}}{0.546} \cdot \frac{t^2}{D} \tag{6}$$

When $\sigma_{\max} = f$, the yield load of single tube under two-way symmetrical compression is shown in Eq. 7

$$F_f = \frac{Lf}{0.546} \cdot \frac{t^2}{D} \tag{7}$$

Eq. 7 shows that the yield load of single circular tube under two-way symmetrical compression is related to $\frac{D}{t}$.

2.2 Ultimate Internal Forces of Honeycomb Circular Tubes under Compression

Thin-walled circular tubes are arranged as a honeycomb structure. The general configurations are aligned configuration and staggered configuration (Figure 2) [8].

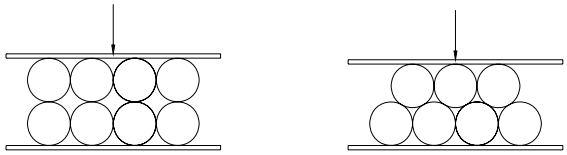

(a) Aligned Configuration (b) Staggered Configuration

Figure 2. Honeycomb Structure

2.2.1 Ultimate Internal Forces of Aligned Circular Tubes under Compression

When the configuration is aligned configuration, the mechanical mode of one tube is shown in Figure 3 (a). Based on the symmetry, a quarter of the structure is extracted, which is a hyperstatic structure with two redundances (Figure 3 (b)). The basic structure is also a curved beam [8].

(a)Simplified Model (b)Hyperstatic Structure with Two Redundances

Figure 3. Internal Forces of Aligned Circular Tubes under Compression

By the method of forces, calculate the section moment of the curved beam. And the maximum of section moment can be acquired when $\alpha = 0$.

$$M_{\max} = 0.15FR \tag{8}$$

Putting Eq. 5 and Eq. 8 into Eq. 4, the yield load of aligned circular tubes under compression is derived when $\sigma_{\max} = f$.

$$F_f = \frac{Lf}{0.9} \cdot \frac{t^2}{D} \tag{9}$$

2.2.2 Ultimate Internal Forces of Staggered Circular Tubes under Compression

When the configuration is staggered configuration, the mechanical mode of one tube is shown in Figure 4 (a). Based on the symmetry, a third of the structure is extracted, which is a hyperstatic structure with two redundances (Figure 4 (b)). The basic structure is also a curved beam [8].

(a)Simplified Model (b) Hyperstatic Structure with Two Redundances

Figure 4. Internal Forces of Staggered Tubes under Compression

Based on Figure 4，the maximum moment of staggered circular tubes under compression is as follows when $\alpha = \frac{\pi}{3}$.

$$M_{\max} = 0.19FR \tag{10}$$

The yield load of staggered circular tubes under compression is shown as

$$F_f = \frac{Lf}{0.88} \cdot \frac{t^2}{D} \tag{11}$$

3. STATIC COMPRESSION EXPERIMENT OF THIN-WALLED CIRCULAR STEEL TUBES

3.1 Experimental Research

Static compression experiments were conducted using the thin-walled circular steel tubes with 25 sizes and 4 configurations. The bearing capacity and energy absorption characteristics for thin-walled circular steel tubes under static compression were studied. The whole absorbed energy was acquired by the internal of load-displacement curve. Because the mass of the circular steel tube affects the energy absorption characteristics. Specific energy absorption was calculated. After the experiment，bearing capacity and energy absorption characteristics of the circular steel tubes were carefully analyzed so as to obtain the optimal configuration and the size of the tubes.

The experimental material was thin-walled circular stainless steel tube with 5 different diameters and 5 different thicknesses respectively. And L = 200mm. The main mechanical parameters were shown in Table 1. The load speed was 15mm/min. When the circular steel tube was flattened, load-displacement curve was recorded. The circular steel tube of each size was compressed three times. The average value was used as final experimental result.

Because the tube size of 25x0.7 is usually used in the project, this circular steel tubes consist of the honeycomb structure. The circular steel tubes with 4 configurations were compressed, and the load-displacement curves were acquired. The configurations are shown in Figure 5.

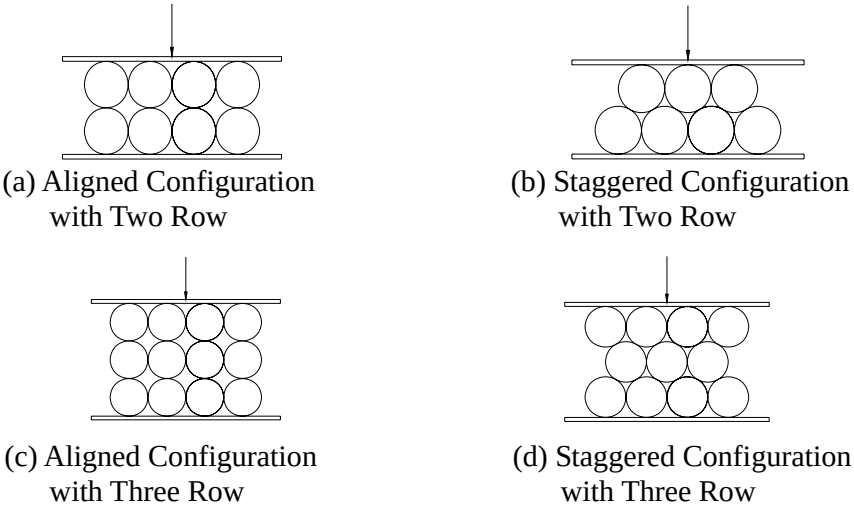

(a) Aligned Configuration with Two Row

(b) Staggered Configuration with Two Row

(c) Aligned Configuration with Three Row

(d) Staggered Configuration with Three Row

Figure 5. Configuration of Honeycomb Thin-walled Circular Steel Tubes

3.2 Experimental Results and Analysis

3.2.1 Static Compression Experiment of Single Circular Steel Tube

The states of deformation of single circular steel tube are shown in Figure 6. According to the experimental results, different sizes of single circular tubes obtained similar load-displacement curves. At the beginning, the load-displacement curve is linear, and the time duration is short. As the load increases, the single circular steel tube begins to yield, and the yield point elongation is present. At this time, the displacement increases gently. This phrase is the major energy-consuming stage. In the course of compression, there are two sharp points, which are plastic hinges. The contact zone between compression surface and the circular steel tube and that between the bearing surface and the circular steel tube gradually expands. At the end, the load increases sharply, and the circular steel tube has the shape of dumbbell. Finally the contact zone completely expands, and the process of energy absorbing is completed.

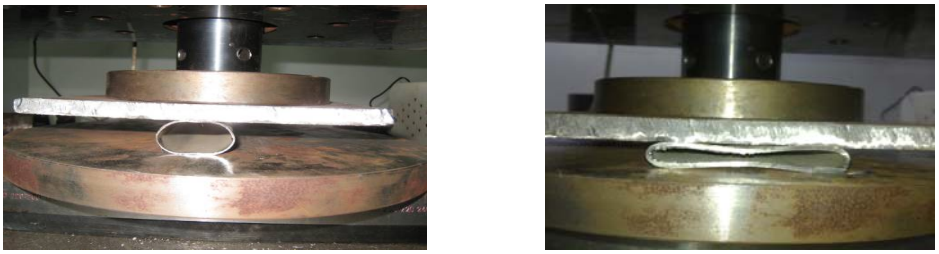

(a) Initial Stage (b) Final Stage

Figure 6. Static Compression Experiment of Single Circular Steel Tube

The load-displacement curve for 5 kinds of thin-walled circular steel tubes with the same thickness and different outer diameter selected for the experiments can be seen in Figure 7. When tube thickness keeps the same, the yield load decreases and the elongation in the yield point increases with the increment of the outer diameter. At the same time, five groups' thin-walled circular steel tubes with the same outer diameter and different thickness are selected for thickness effect (Figure 8). From the load-displacement curves, with the increment of the tube thickness, the yield load of single circular steel tube increases, but the length of the yield point elongation is the same. The total absorbing energy also increases.

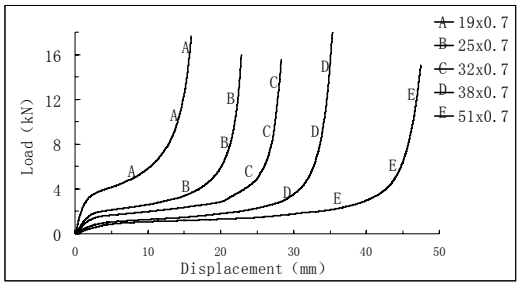

Figure 7. Load-Displacement Curve (Same Thickness)

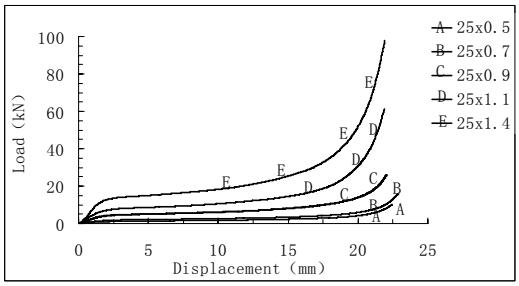

Figure 8. Load-Displacement Curve (Same Outer Diameter)

By internal calculating of the load-displacement curves, the absorbing energy curves of single circular steel tube can be seen in Figure 9. Specific energy absorption (SEA) is the absorbed energy of the unit-mass in the whole compression. From the curves, as the thickness of the circular steel tube with the same outer diameter increases, SEA increases and the increment trend of SEA tends to be slow. With the increment of the outer diameter, SEA of the tube with the same thickness decreases.

When the length of the circular steel tube is a fixed value, SEA relates to D/t. From Figure 10, the relation between the absorbing energy of single circular steel tube and D/t is approximately modeled as a power exponent function when L is a fixed value. As the value of D/t increases, SEA decreases. When the value of D/t ranges from 30 to 45, the absorbing energy of single circular steel tube is large, but the impact force is small. When the value of D/t ranges from 20 to 30, the impact force of single circular steel tube is large, but the absorbing energy is small.

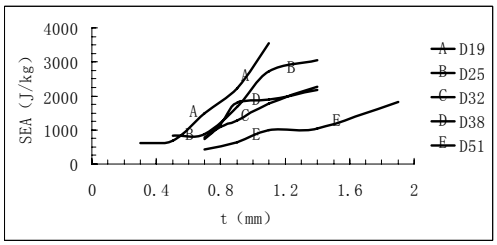

Figure 9. Curve of SEA with the Change of D and t

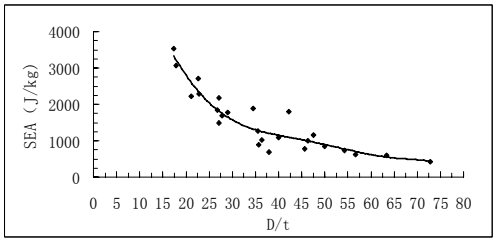

Figure 10. Curve of SEA and D/t

3.2.2 Static Compression Experiment of Honeycomb Thin-walled Circular Steel Tubes

According to the configuration shown in Figure 4, the tubes with the size of 25x0.7 were selected for the experiment. The load-displacement curve were written down. One tube's bearing capacity of honeycomb thin-walled circular steel tubes is similarly equal to the whole bearing capacity divided by the number of the bottom tubes [8]. The compression course is shown in Figure 11, taking the two-row and aligned configuration for example.

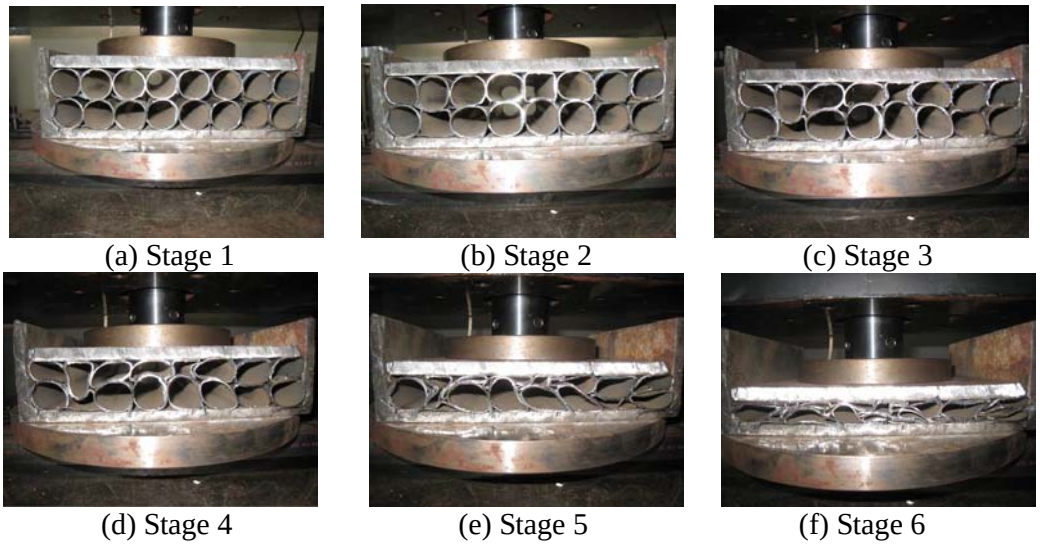

(a) Stage 1 (b) Stage 2 (c) Stage 3

(d) Stage 4 (e) Stage 5 (f) Stage 6

Figure 11. Compression Course of Honeycomb Thin-walled Circular Steel Tubes (Two-row and Aligned Configuration)

According to Figure 11, the circular steel tube yields by row. Considering the influence of the material nonuniformity and experiment condition, the yield tubes are not in the same row, but the number of the yield tubes is similarly equal to that of the tubes in the same row.

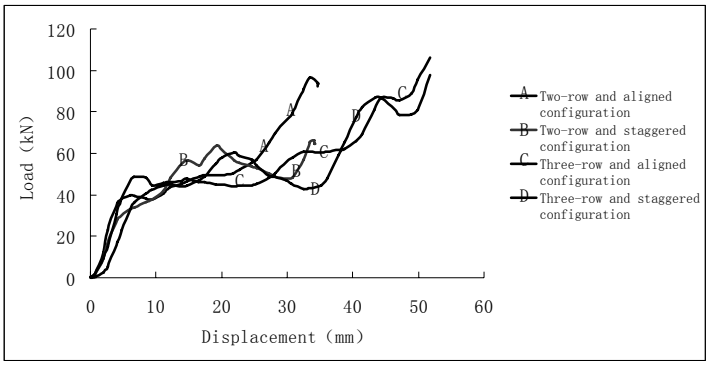

Figure 12. Load-displacement Curve of Honeycomb Thin-walled Circular Steel Tubes

Load-displacement curves of honeycomb thin-walled circular steel tubes are shown in Figure 12. And the trend of four curves is similar. At the beginning, elastic deformation occurs and the load-displacement curve is linear. When the load increases, some circular tubes begin to yield and deformation increasingly extends. As the load continues to increase, inflexion in the curve occurs and the curve increases zigzagly. The reason is that there are large gaps among the tubes and less constraint of the tubes. The deformation increases into the gaps. Finally the circular tubes are flattened. The process of energy absorbing is completed.

4. NUMERICAL SIMULATION OF STATIC COMPRESSION OF THIN-WALLED CIRCULAR STEEL TUBES AND RESULTS COMPARSION

4.1 Numerical Simulation of Static Compression of Single Circular Steel Tube and Results Comparison

The numerical simulation of the circular steel tube is made by the software ANSYS /LS-DYNA[14]. The model size is the same as the size in the experiment. The material of the steel plates is low-carbon steel. Its size is 240x100x10. Mechanical properties are shown in Table 2.

Table 2. Mechanical Properties

Material	Elastic Modulus (GPa)	Yield Stress (MPa)	Tangent Modulus (GPa)	Poisson Ratio	Density (kg/m^3)	Static Friction Coefficient	Dynamic Friction Coefficient
Stainless Steel	190	347	10	0.3	7850	0.15	0.1
Low-carbon steel	210	/	/	0.3	7850	/	/

In the numerical simulation, bilinear isotropic hardening material model is adopted for the circular stainless steel tube. The circular steel tube is simulated with SHELL163. The steel plate is simulated with SOLID164 and a rigid model. The contact between steel plate and circular steel tube is modeled as the automatic surface to surface contact. The contact between circular steel tubes is automatic single surface contact. The contact method is penalty method. This method is commonly used in analyzing the contact of shell element. In the contact analysis, the thickness change of the shell element is considered. The model is shown in Figure 13.

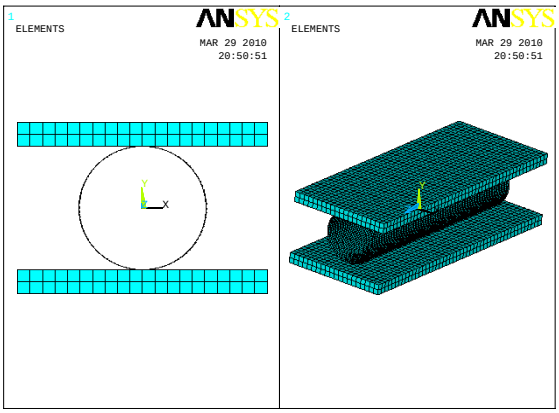

Figure 13. Numerical Analysis Model of Single Circular Steel Tube

The load-displacement curve and absorbed energy of single circular steel tube is shown in Figure 14, taking the circular tube with the size of 200x25x0.7 for example. The compression course can be divided into 3 phases: elastic phase, plastic phase, compaction and strength phase. At first, elastic deformation occurs. When the displacement is about 5mm, plastic yield phase begins and plastic level occurs. It is the main phase for absorbing energy. When the displacement is about 15mm, it is compaction and strength phase and the load sharply increases. After this phase, the tube can not absorb energy. In the numerical analysis, the yield load is 2.33kN comparing with 2.51kN in theory. The absorbed energy in the whole compression in numerical analysis can be directly acquired from the analysis result. The result in numerical analysis tallies with the experiment result. When the displacement comes to about 15mm, the stain energy is 82.65J compared with 73.8J in the experiment. When the displacement does not exceed the half of the outer diameter, the absorbing energy increases linearly.

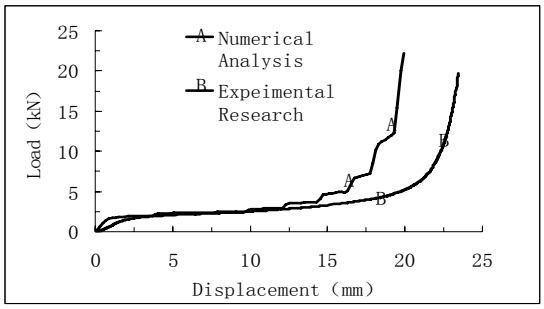

Figure 14. Load-displacement Curve of Static Compression of Single Circular Steel Tube

After theoretical analysis, experiment research and numerical simulation, results comparison about the yield load, the whole absorbing energy and SEA are listed (Table 3). Results of theoretical analysis, experiment research and numerical simulation agree well. It proves that it is suitable and reliable for the numerical simulation.

Table 3. Results Comparison of Theoretical Analysis, Experiment Research and Numerical Simulation

Size of the Tube (LxDxt)	Mass (kg)	Yield Load (An.) (kN)	Yield Load (Ex.) (kN)	Yield Load (Nu.) (kN)	Whole Absorbing Energy (Ex.)(J)	SEA (Ex.) (J/kg)	Whole Absorbing Energy (Ex.)(J)	SEA (Ex.) (J/kg)
200x19x0.3	0.03	0.61	0.61	0.74	16.85	609.05	18.01	650.92
200x19x0.5	0.05	1.69	1.43	1.78	31.06	680.79	37.22	815.85
200x19x0.7	0.06	3.31	4.00	4.06	94.58	1497.07	107.00	1693.60
200x19x0.9	0.08	5.47	6.43	7.19	178.67	2223.85	185.00	2302.65
200x19x1.1	0.10	8.16	10.16	11.03	343.96	3541.92	349.00	3593.82
200x25x0.5	0.06	1.28	1.26	1.38	50.35	833.43	58.10	961.65
200x25x0.7	0.08	2.51	2.20	2.85	73.84	880.11	74.90	892.80
200x25x0.9	0.11	4.15	4.89	6.08	180.46	1686.94	121.01	1131.20
200x25x1.1	0.13	6.21	8.20	8.09	351.96	2714.42	316.01	2437.18
200x25x1.4	0.16	10.05	11.33	13.10	498.67	3060.22	468.02	2872.11
200x32x0.7	0.11	1.96	2.02	1.98	83.77	775.19	89.80	831.02
200x32x0.8	0.12	2.56	2.47	3.13	134.72	1094.39	154.21	1252.69
200x32x0.9	0.14	3.25	3.76	4.02	175.68	1272.63	186.25	1349.18
200x32x1.1	0.17	4.85	6.06	6.01	296.59	1769.24	294.01	1753.83
200x32x1.4	0.21	7.85	9.35	9.81	481.44	2278.62	462.31	2188.07
200x38x0.7	0.13	1.65	1.50	1.53	93.30	724.52	104.12	808.55
200x38x0.8	0.15	2.16	2.45	2.98	168.54	1148.28	179.03	1219.75
200x38x0.9	0.16	2.73	4.09	3.51	296.71	1801.77	265.35	1611.31
200x38x1.1	0.20	4.08	5.12	5.59	379.57	1896.03	408.45	2040.31
200x38x1.4	0.25	6.61	7.20	8.63	550.83	2179.63	562.78	2226.93
200x51x0.7	0.17	1.23	1.01	0.76	73.93	425.70	80.81	465.35
200x51x0.9	0.22	2.04	2.67	2.48	140.29	630.86	158.12	711.02
200x51x1.1	0.27	3.04	3.48	3.74	272.04	1004.88	279.52	1032.52
200x51x1.4	0.34	4.93	5.06	6.08	353.87	1033.25	374.02	1092.10
200x51x1.9	0.46	9.07	10.73	11.30	843.61	1833.51	863.79	1877.37

(where An. refers to the results of theoretical analysis, Ex. refers to those of experiment research, Nu. refers to those of numerical simulation.)

4.2 Numerical Simulation for Static Compression of Honeycomb Thin-walled Circular Steel Tubes and Results Comparison

The numerical simulation of circular steel tubes is made. The model size is the same as the size in the experiment. The model is shown in Figure 15, taking aligned configuration for example.

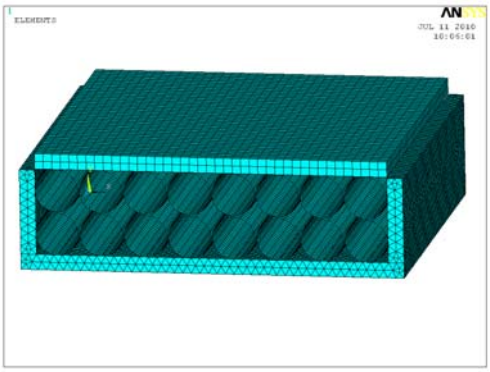

Figure 15. Numerical Analysis Model of Honeycomb Thin-walled Circular Tubes

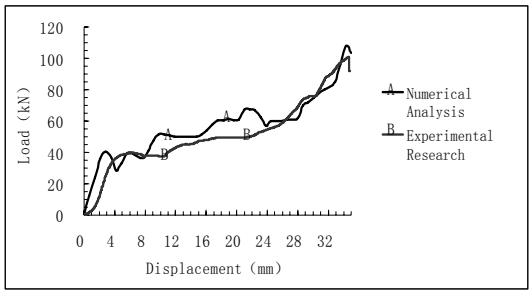

Figure 16. Load-displacement Curve of Honeycomb Thin-walled Circular Tubes (Aligned Configuration)

The load-displacement curve of honeycomb thin-walled circular tubes with aligned configuration is shown in Figure 16. The results of experiment and numerical simulation agree well. At the beginning，elastic deformation occurs and the load-displacement curve is linear. As the load increases，some tubes begin to yield and the curve is subdued. When the load continues to increase, the curve rises up. However, the result of numerical simulation is slightly larger than that of experiment research. When the circular tubes are flattened, the honeycomb tubes can not absorb energy.

From Table 4 and Table 5, the average bearing capacity of single thin-walled circular steel tubes is lower than the corresponding one that arranged in a honeycomb structure. This difference is caused by the constraint among the honeycomb circular tubes configurations. It will increase the bearing capacity of the thin-walled circular steel tube. In theory the thicker the configuration is, the more the bearing points have, the larger the bearing capacity is. The real bearing capacity of the two configurations, the value of the staggered configuration is larger than that of the aligned configuration. However the absorbed energy of the circular steel tube with aligned configuration is larger than that of the circular steel tube with staggered configuration.

Table 4. Results Comparison of Honeycomb Thin-walled Circular Steel Tubes

Configuration	Number of Tubes	Yield Load（kN）					Bearing Capacity（kN）			
		Whole Tubes（Ex.）	Whole Tubes（Nu.）	Single Tubes（An.）	Single Tube（Ex.）	Single Tube（Nu.）	Whole Tubes（Ex.）	Whole Tubes（Nu.）	Single Tube（Ex.）	Single Tube（Nu.）
Single Tube	1	2.20	2.85	2.51	2.20	2.85	8.13	8.85	8.13	8.85
Aligned Configuration with Tow Row	16	29.18	28.71	1.53	1.82	1.79	80.49	104.15	10.06	13.02
Staggered Configuration with Two Row	15	30.14	25.80	1.57	2.01	1.72	71.93	121.20	10.28	15.15
Aligned Configuration with Three Row	24	44.65	45.80	1.53	1.86	1.91	100.01	130.01	12.50	16.25
Staggered Configuration with Three Row	23	44.27	39.10	1.57	1.92	1.70	99.20	116.50	14.17	16.64

Table 5. Results Comparison of the Whole Absorbing Energy for Honeycomb Thin-walled Circular Steel Tubes

Configuration	Number of Tubes	Whole Absorbing Energy（J）			
		Whole Tubes（Ex.）	Whole Tubes（Nu.）	Single Tube (Ex.)	Single Tube（Nu.）
Single Circular Tube	1	73.84	74.90	73.84	74.90
Aligned Configuration with Tow Row	16	1595.83	1541.00	99.70	96.31
Staggered Configuration with Two Row	15	1365.00	1290.12	91.00	86.01
Aligned Configuration with Three Row	24	2513.30	1930.00	104.70	80.42
Staggered Configuration with Three Row	23	2405.30	1830.00	104.60	79.57

5. APPLICATION AND CONCLUSIONS

The results in this paper may be useful in designing a steel retractable roof structure with respect to passive collision protection. Steel grid structures are applied in retractable roof structure, whose span is over 60m. Thin-walled circular steel tubes, as the energy absorption device, are welded in the lateral contact area in Figure 17. (Black bold lines stands for thin-walled circular steel tubes) Through the numerical analysis, the collision of the moving roofs are modeled. It shows that thin-walled circular steel tubes reduce the collision response of the moving roofs. When the collision of the moving roofs occurs, the absorbed energy of the tubes increases. And the moving roofs' s initial impact force and bearing reaction decrease. Space lacks for a detailed description of it.

Single thin-walled circular steel tube and honeycomb thin-walled circular steel tubes with 4 configurations under static compression are conducted. Load-displacement curves are recorded and energy absorption is calculated. Then the numerical simulation verifies the experimental results. Based on the analytical results, the following conclusions can be drawn.

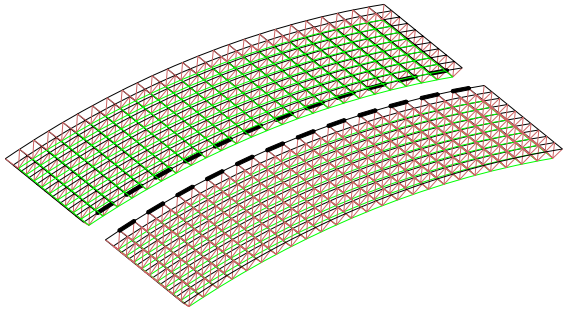

Figure 17. Retractable Roof Structures with Thin-walled Circular Steel Tube

(1) The bearing capacity of single thin-walled circular steel tube is lower than that of one circular tube average value for honeycomb thin-walled circular steel tubes.
(2) The circular steel tube yields by row. Considering the influence of the material nonuniformity and experiment condition, the yield tubes are not in the same row, but the number of the yield tubes is similarly equal to that of the tubes in the same row.
(3) The configuration of staggered thin-walled circular steel tubes with value between 20 and 30 exhibits good bearing capacity. The configuration of aligned thin-walled circular steel tubes of values between 30 and 45 exhibits good energy absorbing characteristic.
(4) With respect to the bearing capacity and energy absorbing characteristic, the numerical simulation verifies the experimental results.
(5) Steel grid structures are applied in retractable roof structure, whose span is over 60m. Thin-walled circular steel tubes can be welded in the lateral contact area. It is a technique of passive safety protection. It achieves the aim to avoid the collision accidents of movable roofs.

Nomenclature

F	static radical load which the circular steel tube bears
R	radius of the tube
$M(\alpha)$	moment of hyperstatic curved beam, $0 \le \alpha \le \frac{\pi}{2}$
$M_{\max}$	the maximum of section moment
$\sigma_{\max}$	the maximum of bending stress
L	length of the tube
t	thickness of the tube.
D	outer diameter of the tube
D/t	ratio of the outer diameter and thickness of the tube
W	section modulus
f	the yield stress of the circular steel tube
F_y	the yield load of the tube under compression
EN	the absorbed energy in the whole compression which can be calculated by integral of load-displacement curve, $EN = \int_0^l F ds$
s	the displacement of the circular steel tubes in static radical compression
Es	specific energy absorption(SEA), $E_s = \frac{EN}{m}$
m	the mass of the circular steel tube
E	elastic modulus
ρ	material density of the circular steel tube

ACKNOWLEDGEMENTS

This project is supported by the National Science Foundation of China（No. 51078259） and the Seed Foundation of Tianjin University（No. 03-19）. The support is gratefully acknowledged. The technical consultation provided by Professor Han Zhu and Xiliang Liu throughout the whole process is appreciated.

REFERENCES

[1] Abrhamson, G.R., “Dynamic Plastic Flow Buckling of a Cylindrical Shell from Uniform Radial Impulse Procedures”, Forth US National Congress of Applied Mechanics, 1962, No. 3, pp. 939-950.

[2] Lindberg, H.E., “Dynamic Plastic Buckling of Thin Cylindrical Shell Containing an Elastic Core”, J. Appl. Mech., 1965, No. 1, pp. 803-812.

[3] Gupta, N.K., Easwara, Prasad, G.L. and Gupta, S.K., “Axial Compression of Metallic Spherical Shells between Rigid Plates”, Thin-Walled Structures, 1999, Vol. 34, No.1, pp. 21-41.

[4] Gupta, N.K. and Venkatesh., “Experimental and Numerical Studies of Dynamic Axial Compression of Thin Walled Spherical Shells”, International Journal of Impact Engineering, 2004, Vol. 30, No. 8-9, pp. 1225-1240.

[5] Ru, C.Q. and Wang, R. “Two Problems about Plastic Buckling of the Cylindrical Shell from under Radial Impulse Load” (in Chinese), Chinese Journal of Solid Mechanics, 1988, No. 3, pp. 101-109.

[6] Gu, W.M., Liu, T.G., Tang, W.Y. and et al., “Dynamic Plastic Buckling of A Cylindrical Shell with Finite Length under Radical Impulse Load” (in Chinese), Chinese Journal of Applied Mechanics, 1995, No. 4, pp. 88-95.

[7] Zeng, S.Y., Yan, L.H., Chen, B. and et al., “Modal Solution of Large Plastic Deformation Problem for Multi-row Energy Absorbing Units under Shock Waves” (in Chinese), Chinese Journal of Solid Mechanics, 1999, Vol. 20, No. 3, pp. 237-244.

[8] Gu, H.J., “Structure Response of Multi-row Cylindrical Shells under Explosion and Shock” (in Chinese), Ph.D. Thesis, Nanjing University of Science & Technology, Nanjing, 2003.

[9] Du, X.W. and Song, H.W., “Impact Dynamics of the Cylindrical Shell and Crashworthiness Design” (in Chinese), Science Press, 2004.

[10] Zhang, F.W and Liu, X.L, “Research on the Development and Retractable Mechanism of Retractable Roof Structure” (in Chinese), Steel Construction, 2001, Vol. 16, No. 54, pp. 1-6.

[11] Guan, F.L, Cheng, Y., Yu, Y.H. and et al., “Structural Design of Retractable Roof Structure” (in Chinese), Journal of Building Structures, 2005, Vol. 26, No. 4, pp. 112-116.

[12] Kazuo, Ishii, “Structural Design of Retractable Roof Structures”, WIT Press, 2000.

[13] Chen, Y.Y, Jiang, X.F. and Cheng, Y.J., “Study on Extreme Cases for Large-Span Retractable Roof Structure” (in Chinese), Journal of Building Structures, 2007, Vol. 28, No. 1, pp. 21-27.

[14] He, T., Yang, J., Jin X., and et al., “A Textbook of Nonlinear Finite Element Analysis (ANSYS 10.0/LS-DYNA)” (in Chinese), China Machine Press, 2007.

RELIABILITY OF DETERIORATING STEEL BOX-GIRDER BRIDGES UNDER PITTING CORROSION

Yasser Sharifi

Department of Civil Engineering
Vali-e-Asr University of Rafsanjan, Rafsanjan, Iran
(Corresponding author: E-mail: y.sharifi@vru.ac.ir or yasser_sharifi@yahoo.com)

Received: 17 August 2010; Revised: 31 December 2010; Accepted: 5 January 2010

ABSTRACT: Deteriorated bridges are subjected to time-variant changes of resistance. Corrosion is one of the most important types of deterioration in steel bridges. The consequence is a reduction in safety of a bridge. Therefore, it is needed to evaluate procedures for an accurate prediction of the load-carrying capacity and reliability of corroded bridges, in order to make rational decisions about repair, renewal or rehabilitation. This paper presents a highway bridge reliability-based design formulation which accounts for pitting corrosion effects on steel box girder bridges. The study involves the idealization of pitting corrosion, development of resistance models for corroded steel box girders, development of load models, formulation of limit state function, development of reliability analysis method, and development of the time-dependent reliability for corroded steel girders. Numerical example illustrates the application of the proposed approach. The results of this study can be used for the better prediction of the service life of deteriorating steel box girder bridges and the development of optimal reliability-based maintenance strategies.

Keywords: Bridges, Steel box girders, Pitting corrosion, Load-carrying capacity, Time-dependent reliability, Repair and rehabilitation

1. INTRODUCTION

Bridges deteriorate over the time. The main causes of deterioration in bridges are fatigue and environment. For steel bridges one of the most important forms of deterioration is corrosion (Sharifi and Paik [1, 2]; Sharifi and Rahgozar [3-5]; Kayser and Nowak [6]). The major effect of corrosion is the loss of material section resulting in a reduction of structural load-carrying capacity and reliability. Deficient bridges are needed to be repaired or replaced. In addition, the repair or maintenances cost of a bridge is of great importance. Therefore, it is essential to develop a procedure in order to accurate prediction of load-carrying capacity for existing bridges (Sharifi and Paik [1, 2]; Czarnecki and Nowak [7]; Cheung and Li [8]). Several approaches to quantify the increasing dependency of our life and economy on civil infrastructures indicate that the service loss due to their malfunctioning would be extremely expensive. Therefore, this type of loss should be included in assessment of civil infrastructures. Performing maintenance interventions on civil infrastructures is a requirement for maintaining the safety and functionality of the ground transportation system (Kong and Frangopol [9]).

Load effect and resistance of a bridge are random variables. Therefore, it is common to measure bridge structural performance in terms of reliability and probability. The reliability methods allow for consideration of uncertainties associated with material properties, geometry and dimensions, loads and environmental conditions (Melchers and Jeffrey [10]; Melchers [11]; Kayser and Nowak [6]).

Kayser and Nowak [6] developed a damage model which evaluates the reliability of a corroded steel girder bridge over time. This model was used for a uniform corroded I-shape steel girder in different environments. It was found that a rural environment, with exposure to pure water, negligibly affects a bridge. An urban environment, with automobile and industrial pollutants, moderately environment, with salt from sea water or deicer use, significantly reduces safety over a

50-year life. In another research by Czarnecki and Nowak [7] the system and member reliability of deteriorated steel girder bridges with uniform corrosion has been evaluated, and it was found that the member reliability give conservative indices. Cheung and Li [8] investigated the serviceability reliability of damaged steel I-girder bridges that affected under uniform corrosion. It has been found that the serviceability of a corroded steel bridge may deteriorate drastically during its service life, even though the nominal maximum deflection only shows little increase in the same period. Thoft-Christensen [10] defined bridge reliability states and proposed a reliability-based approach to bridge maintenance planning.

The objective of this paper is to present an approach to quantifying the reduction in load-carrying capacity and safety for corroded steel box girder bridges. The discussion will concentrate on the pitting corrosion of simple span steel box girder bridges. A member reliability model is developed based on the bending failure mode. To illustrate the approach, reliability analysis is carried out for a steel box girder bridge. The calculations are performed for various lifetimes in a marine environment. This study highlights the problems associated with determining the latest such intervention for a sample bridge substructure. The experience gained and the difficulties faced by practicing engineers when using this method of analysis are also discussed.

2. CORROSION MODELING

There are several forms of corrosion. In this paper, pitting corrosion is considered. Corrosion affects various structural parts differently. It seriously reduces the serviceability of a bridge. In the result, there is also an increased exposure of the superstructure to a corrosive environment. The dynamic loads may also be increased. Corrosion of the superstructure may not only cause fracture, but also yielding or buckling of members. In particular, three possible changes to a steel girder bridge can be considered, an increase in stress, a change in geometric properties, and a buildup of corrosion products (Czarnecki and Nowak [7]; Kayser and Nowak [6]).

2.1 Pitting Corrosion Idealization

Figure 1 shows some of the more common types of corrosion-related damage that affect the strength of steel structures to a greater extent than other types. General corrosion (also called uniform corrosion) uniformly reduces the thickness of structural members, as shown in Figure 1(a), whereas localized corrosion (e.g., pitting or grooving) causes degradation in local regions, as shown in Figure 1(b). Fatigue cracks may sometimes arise from localized corrosion, as shown in Figure 1(c). In the present study, pitting corrosion damage idealization is considered.

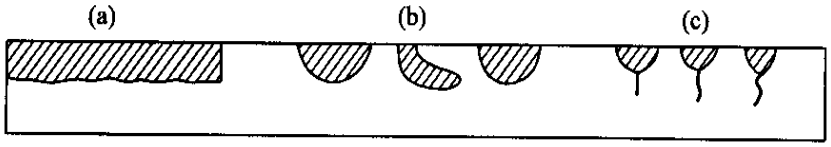

Figure 1. Typical Modes of Corrosion Damage: (a) General (Uniform) Corrosion; (b) Localized Corrosion; (c) Fatigue Cracks Arising from Localized Corrosion

To assess the scale of breakdown due to pit corrosion, a parameter denoted DOP (degree of pit corrosion intensity) is often used, where DOP is defined as the ratio percentage of the corroded surface area to the original plate surface area, namely,

$$DOP = \frac{1}{ab}\sum_{i=1}^{n} A_{pi} \times 100(\%), \tag{1}$$

where n is the number of pits, A_{pi} is the surface area of the ith pit, a is the plate length, and b is the plate breadth. Figure 2 shows samples of pit corrosion damage distribution in plates. Although the distribution of the pit corrosion on the plates is scattered, it can be seen that the shape of the corrosion is typically circular (Paik et al. [13, 14]; Nakai et al. [15]). The maximum diameter of localized corrosion may be in the range of 25-80 mm for the marine immersion corrosion of steel (Daidola et al. [16]), with the lower values more likely.

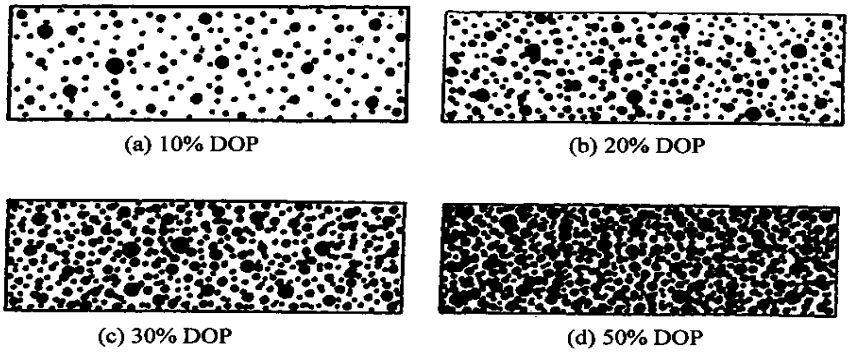

Figure 2. Pitting Intensity Diagrams (Paik et al. [13, 14])
(DOP = Degree of Pit Corrosion Intensity as a Ratio of the Pitted Surface Area to the Original Plate Surface Area): (a) 10% DOP; (b) 20% DOP; (c) 30% DOP; (d) 50% DOP

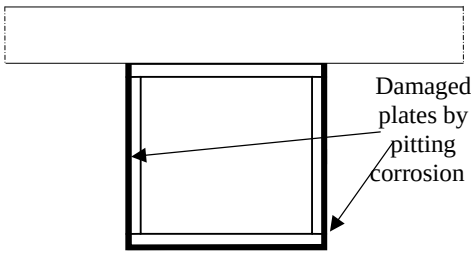

Figure 3. Model of Corroded Non-composite Steel Box Girder Cross-section

It is assumed that all sides of the girder will corrode in a localized manner, except for the upper plate, which is protected from corrosion attack by the concrete deck. It is also assumed that the interior of the box girder is protected from environmental exposure and corrosion attack, as can be seen from Figure 3. Figure 3 shows that pitting corrosion which is uniformly distributed decreases the strength of both sides and the bottom flange of the box girder section by the different degrees of intensity shown in Figure 4. Finally, it is assumed that the pit diameter varies from 10 to 80 mm, and the distance between the adjacent pits centers is constant. The depth of pit corrosion will of course vary.

2.2 Probabilistic Corrosion Rate Modeling

In reliability analysis based on the ultimate steel box girder strength of corroded bridges, a probabilistic corrosion rate estimation model needs to be established in advance. Data on corrosion performance of actual steel bridges have been collected by Kayser [17]. As expected, corrosion occurs where water is accumulated. For steel-girder bridges, this happens at leaking deck joints. Moreover, Corrosion is influenced by the environment, i.e., the amount of moisture in the air and the presence of salt. Therefore, the geographic location is of vital importance when planning the maintenance of a steel bridge. It has been observed that the rate of corrosion can be different in

different environments, and for different girders. For example, in highway overpass, girders are exposed to a mixture of salt, snow and water splashed by trucks. The highest concentration of this aggressive medium is on the exterior girder and the concentration of salt and/or water decreases in the direction of traffic (Kayser and Nowak [6]).

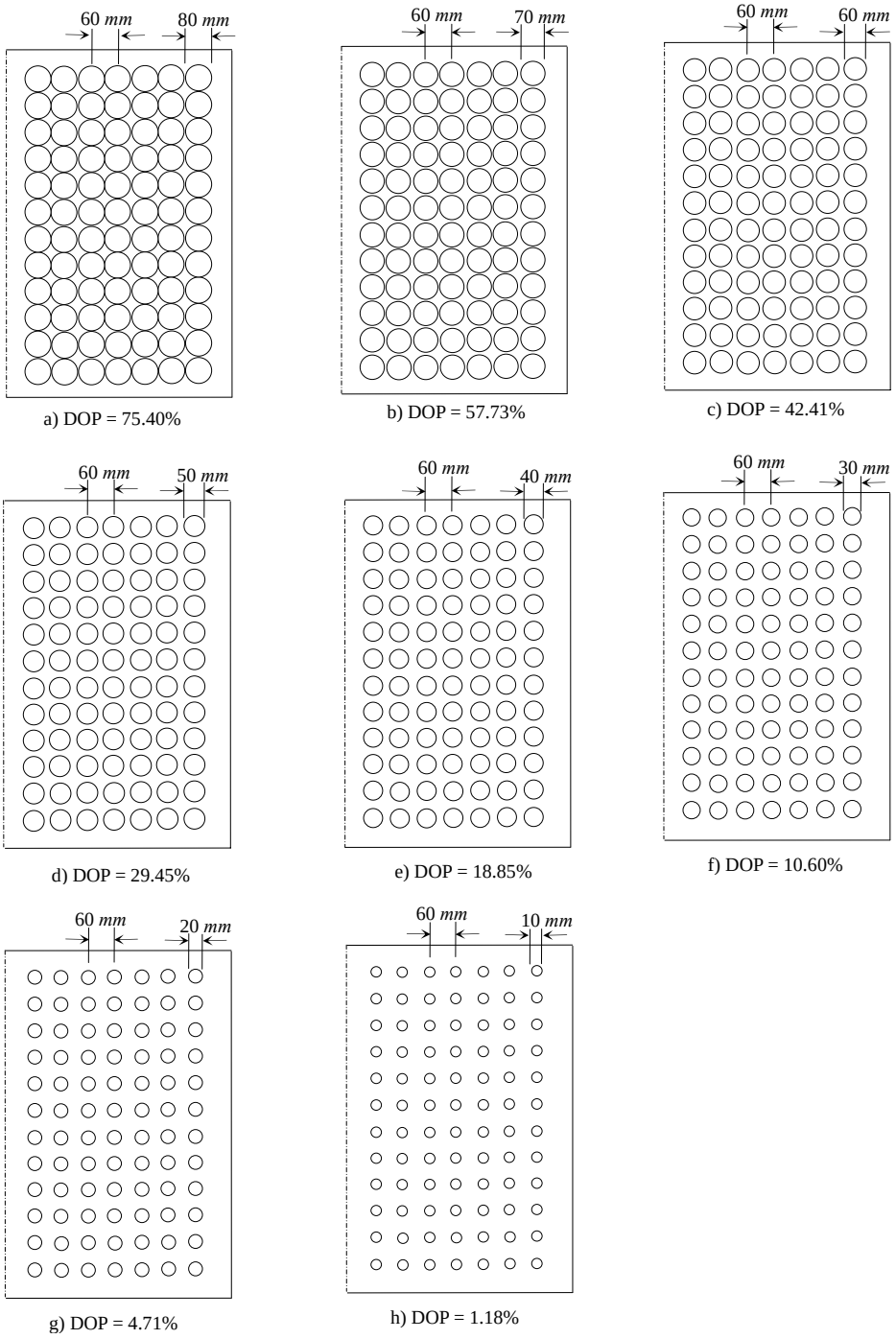

Figure 4. Typical Models of Pit Distribution

Table 1. Statistical Parameters for A and B (Sommer et al. [18])

Parameters	Carbon Steel		Weathering Steel	
	A ($\times 10^{-3}$ mm)	B	A ($\times 10^{-3}$ mm)	B
Rural Environment				
Mean value, μ	34.0	0.65	33.3	0.498
Coefficient of variation, σ/μ	0.09	0.10	0.34	0.09
Coefficient of correlation, ρ_{AB}	Not available		-0.05	
Urban Environment				
Mean value, μ	80.2	0.593	50.7	0.567
Coefficient of variation, σ/μ	0.42	0.40	0.30	0.37
Coefficient of correlation, ρ_{AB}	0.68		0.19	
Marine Environment				
Mean value, μ	70.6	0.789	40.2	0.557
Coefficient of variation, σ/μ	0.66	0.49	0.22	0.10
Coefficient of correlation, ρ_{AB}	-0.31		-0.45	

Research has shown that corrosion propagation can be modeled with a good degree of approximation with the following exponential function (Komp [19]).

$$C(t) = A\,t^{B}, \tag{2}$$

where $C(t)$ = the average corrosion penetration in micrometers (10^{-3} mm); t = the time in years; and A and B = parameters to be determined from regression analysis of the experimental data.

Table 1 gives the mean values, coefficients of variation, and coefficients of correlation for A and B. It shows, as expected that the parameters for weathering steel are smaller than for carbon steel, since corrosion develops slower in weathering steel, and it shows that in most cases the parameters are the lowest in rural environments and highest in urban environments. It was agreed that corrosion of steel is affected by several factors such as type of steel, surface protection, environmental effects, and presence of pollutants, crevices and stress (Czarnecki and Nowak [7]).

3. BOX GIRDER ULTIMATE STRENGTH MODELING

There are three possible approaches to the development of a simple formula for the prediction of box girder ultimate strength, and this formula can also be applied to estimates of the ultimate moment of box girders.

The first is an analytical approach that is based on an assumed stress distribution over the box section, from which the box's moment of resistance is theoretically calculated by taking into account buckling in the compression flange and yielding in the tension flange. The second is an empirical approach in which an expression is derived on the basis of experimental or numerical data from scaled box models. The third is a linear approach in which the behavior of the box up to the collapse of the compression flange is assumed to be linear, and the ultimate moment capacity of the box is basically expressed as the ultimate strength to yield strength ratio of the compression flange multiplied by the first yield moment of the box girder (Paik and Thayamballi [20]).

The third approach is quite simple, but its degree of accuracy is often relatively poor, because the after-buckling of the compression flange causes the neutral axis of the box to change position. Empirical formulas (the second approach) may provide reasonable solutions for a conventional box, but care must be exercised in using them for new box types or outside the limits of the data on which they are based. Analytical formulations (the first approach), in contrast, can be applied to most situations of interest.

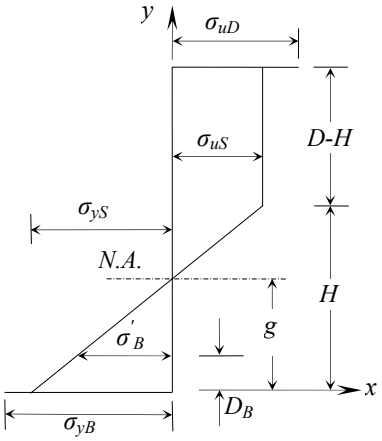

Figure 5. Longitudinal Stress Distribution Over the Box Cross-section at the Overall Collapse State Suggested by (Paik and Thayamballi [20])

This study employed the analytical approach to calculate the ultimate strength of a box under bending conditions. It is often observed in nonlinear finite element calculations that a box will reach its ultimate limit if both the collapse of the compression flange and the yielding of the tension flange occur. The side shell in the vicinity of the compression and tension flanges will also often fail, although the material around the final neutral axis will remain essentially in an elastic state. Based on these observations a credible distribution of the longitudinal stresses in the box section at the overall collapse state derived and shown in Figure 5 (Paik and Thayamballi [20]). On the basis of this distribution, they then derived an explicit analytical formula for the corresponding resistive moment. The accuracy of the formula was then verified by comparison with both experimental and numerical results. The resulting expressions for the ultimate bending strength of a double-bottomed box are given by the following.

$$\begin{aligned} M_u = & -A_D\sigma_{uD}(D-g) - \frac{A_S}{D}(D-H)(D+H-2g)\sigma_{uS} \\ & - A_B g\sigma_{yB} + \frac{A_B'}{H}(g-D_B)\left[D_B\sigma_{uS} - (H-D_B)\sigma_{yS}\right], \\ & - \frac{A_S H}{3D}\left[(2H-3g)\sigma_{uS} - (H-3g)\sigma_{yS}\right] \end{aligned} \tag{3}$$

where

$$\begin{aligned} H = & \frac{1}{2}\left\{\left(\frac{A_D\sigma_{uD} + 2A_S\sigma_{uS} - A_B\sigma_{yB} - A_B'\sigma_{ys}}{A_S(\sigma_{uS}+\sigma_{ys})}\right)D\right. \\ & \left. + \left[\left(\frac{A_D\sigma_{uD} + 2A_S\sigma_{uS} - A_B\sigma_{yB} - A_B'\sigma_{ys}}{A_S(\sigma_{uS}+\sigma_{ys})}\right)^2 D^2 + \frac{4A_B'D_B}{A_S}D\right]^{1/2}\right\}, \end{aligned}$$

$$g = \frac{\sigma_{ys}}{\sigma_{us} + \sigma_{ys}} H \quad .$$

For a single box girder, the formula can be simplified to

$$M_u = -A_D \sigma_{uD} (D - g) - \frac{A_S}{D}(D - H)(D + H - 2g)\sigma_{uS} - A_B g \sigma_{yB} - \frac{A_S H}{3D}\left[(2H - 3g)\sigma_{uS} - (H - 3g)\sigma_{yS}\right], \quad (4)$$

where

$$H = \left(\frac{A_D \sigma_{uD} + 2A_S \sigma_{uS} - A_B \sigma_{yB}}{A_S (\sigma_{uS} + \sigma_{ys})}\right) D \quad ,$$

$$g = \frac{\sigma_{ys}}{\sigma_{us} + \sigma_{ys}} H \quad .$$

To calculate the ultimate moment capacity of the box using Eq. 3 or 4, the ultimate strength of the compression flange and the side structure in the vicinity of the compression flange must be known. The ultimate strength of an imperfect unstiffened plate under compression stress may be predicted as a function of the plate slenderness ratio, as follows (Paik et al. [21]).

$$\sigma_u / \sigma_y = \begin{cases} -0.032\beta^4 + 0.002\beta^2 + 1.0 & \text{for} \quad \beta \le 1.5 \\ 1.274/\beta & \text{for} \quad 1.5 < \beta \le 3.0 \\ 1.248/\beta^2 + 0.283 & \text{for} \quad \beta > 3.0 \end{cases} . \quad (5)$$

It should be noted that the foregoing formula implicitly includes the effects of initial imperfections at a moderately large level. For convenience, the illustrative calculations presented in this study employ Eq. 5 to predict the ultimate compressive strength of the representative unstiffened plate at the compressive flange or side structure of the box.

4. PLATE ULTIMATE STRENGTH UNDER PIT CORROSION WASTAGE

Corrosion wastage can reduce the ultimate strength of bridge section's plates. The ultimate strength of a steel member with general corrosion can be easily predicted, i.e., by excluding the plate thickness loss that results from corrosion. It is proposed here, in contrast, that the ultimate strength prediction of a structural member with pit corrosion be made using a strength knock-down factor approach.

A series of nonlinear analytical and Experimental studies by Paik et al. [13] demonstrate that the ultimate strength of a plate with pit corrosion can be estimated with a strength reduction factor that can be calculated using the following formulation for axial compressive loading.

$$R_{xr} = \frac{\sigma_{xu}}{\sigma_{xuo}} = \left(\frac{A_0 - A_r}{A_0}\right)^{0.73} , \quad (6)$$

where

R_{xr} = a factor of ultimate compressive strength reduction due to pit corrosion,
σ_{xu} = ultimate compressive strength for a member with pit corrosion,
σ_{xuo} = ultimate compressive strength for an intact (uncorroded) member,
A_0 = original cross-sectional area of the intact member and
A_r = cross-sectional area involved in pit corrosion at the smallest cross-section (see Figure 6).

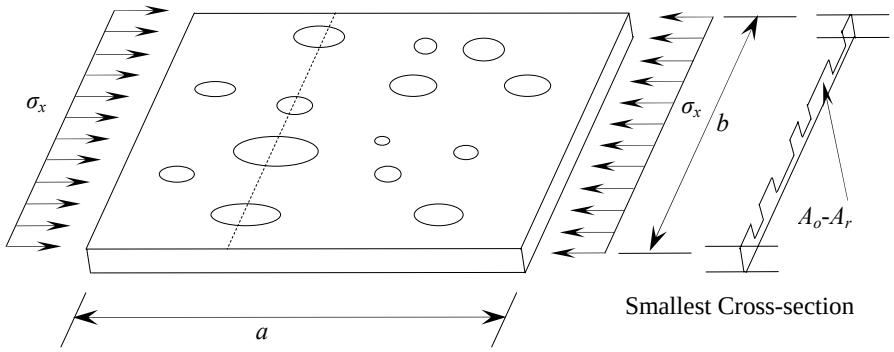

Figure 6. Schematic of Localized Pit Corrosion and Definition of the Smallest Cross-sectional Area (A_0 = Cross-sectional Area of the Intact Plate)

5. LOAD MODELING

Two load components are considered: dead load and live load (truck traffic).

5.1 Dead Load Model

Dead load is treated as the normal random variable. The basic statistical parameters are a bias factor, λ, which is the ratio of the mean to nominal value, and coefficient of variation V. Dead load includes the weight of the girders, deck slab, wearing surface, barriers, diaphragms and sidewalk, where applicable. Bias factor λ = 1.03 and V = 0.08 for factory-made components (girders, diaphragms), λ = 1.05 and V = 0.10 for cast-in-place components (deck, barriers, sidewalk), and the asphalt wearing surface is taken to have a mean value of 75 mm, with V = 0.25 (Nowak and Collins [22]; Nowak [23, 24]; Nowak and Szerszen [25, 26]).

5.2 Live Load Model

The live load on a bridge is the result of vehicular traffic. It can be considered as the sum of the static and dynamic components. The latter can be represented by an equivalent static load that is defined as the dynamic load factor. The live load effects depend on a number of parameters, including the span length, axle load, axle configuration, gross vehicle weight, position of the vehicle on the bridge (transversely and longitudinally), traffic volume, number of vehicles on the bridge (multiple presence), girder spacing and mechanical properties of the structural members (Nowak and Collins [22]; Nowak [23, 24]; Nowak and Szerszen [25, 26]). This study employed the load model developed by AASHTO LRFD [27] (Figure 7).

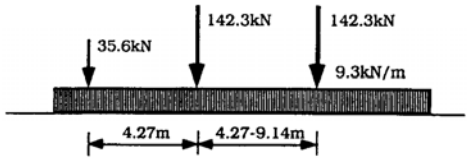

Figure 7. Proposed Nominal Live Loading (HL-93 Live Load in AASHTO LRFD [27])

It is assumed that the bias factor, λ, for the live load distribution factors specified in the design code is between 1.10 and 1.20, and that the coefficient of variation, V, is 0.18 (Barker and Puckett [28]). This study adopted a bias factor of 1.15 and a coefficient of variation of 0.18. The dynamic load factor is defined as the ratio of the dynamic load to the static live load. Field measurements show that the dynamic load factor decreases for heavier trucks (Nowak and Collins [22]; Nowak [23, 24]; Nowak and Szerszen [25, 26]). Here, the dynamic load factor (*IM*) is selected on the basis of the AASHTO LRFD specifications [27]. The design live load in AASHTO LRFD [27] is specified as the effect of the design truck shown in Figure 7 superimposed with a uniformly distributed load of 9.3 kN/m. The live load distribution for interior and exterior girders can be estimated using the AASHTO specifications (for further information, see (Barker and Puckett [28]).

6. RELIABILITY CALCULATION

In all engineering structural system design, uncertainties are unavoidable due to stochastic nature of materials and loads, and imperfect nature of mathematical model. These uncertainties can be accounted only through a reliability analysis. The aim is to calculate the probability of failure, and hence its complement, the reliability related to the ultimate strength of the bridge acted upon by the extreme total bending moment during its lifetime. The bridge strength will reduce with time because of corrosion. Thus the reliability measure will reduce with time. In probabilistic assessment, any uncertainty about a variable, which is expressed in terms of its probability density function, is explicitly taken into account. Reliability analysis begins with the formulation of a limit state function that represents the performance of a structure or element in terms of several basic random variables. Since the theory of reliability analysis is discussed in many references (Nowak and Collins [22]; Mansour [29]; Achintya and Mahadevan [30]; Lemarie [31]; Melchers [32]), only a very brief description is given here. Generally the probability of failure can be calculated as follows:

$$P_f = \int_{g(x)\le 0} p_x(X)\,dx, \tag{7}$$

where $p(X)$ is the joint probability density function of the random variables, $X = (x_1, x_2, \ldots, x_n)$, which are associated with loading, material properties, geometrical characteristics, etc., and $g(x)$ is the limit state function, defined such that negative values imply failure.

The result of such a standard reliability calculation is a reliability index γ which is related to the probability of failure by,

$$P_f = \phi(-\gamma), \tag{8}$$

where ϕ is the standard normal distribution function.

The limit state function for the steel box girders in this example is defined as follows.

$$g(x) = M_u - M_D - M_L \leq 0, \tag{9}$$

where

$g(x)$ = the limit state function,
M_u = a random variable representing the resistance ultimate strength,
M_D = a random variable representing the dead load, and
M_L = a random variable representing the live load.

The aforementioned failure condition uses the limit state function for box girder collapse as a function of the three variables. However, recall that variable M_u is actually estimated by an analytical procedure that involves the individual thicknesses, yield strength, and modulus of elasticity (t, σ_y and E) such that

$$M_u = M_u(t, \sigma_y, E). \tag{10}$$

It would appear that there are five types of random variables to be characterized. In fact, however, there are six, because the thickness value of the member at any particular time is also a function of the two parameters of the corrosion rate (A, B).

Reliability analysis can be performed through numerical integration, the simulation technique or approximate methods. Numerical integration is not performed in this case because of the large dimension and the complexity of the problem. Although the simulation technique may be time-consuming because of the small probabilities involved in the analysis, it has become popular in recent years due to the development of such variance reduction techniques as importance sampling (Sarveswaran and Roberts [33]). Therefore, the equation is normally solved through simulation techniques or approximate procedures (Nowak and Collins [22]; Mansour [29]; Achintya and Mahadevan [30]; Lemarie [31]; Melchers [32]).

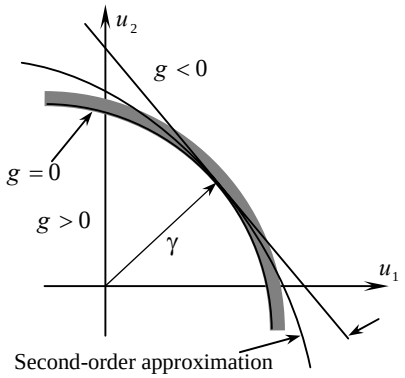

Figure 8. First- and Second-order Reliability Methods

In the approximation methods (Figure 8), the limit state surface is usually approximated at the design point by either a tangent hyper plane or hyper parabola, which simplifies the mathematics related to the calculation of failure probability. The first type of approximation results in the use of a so called first-order reliability method (FORM), and the second type is central to the so called second-order reliability method (SORM). Simulation technique consists of obtaining cumulative distribution functions for each and every random variable and simulating the ultimate strength of box plates for combinations of random variable values. It uses randomly generated samples of the input variables for each deterministic analysis, and estimates reliability after numerous repetitions of the deterministic analysis. However for simulation technique to be successful, the sample size should be very large. Hence methods have been proposed to reduce the sample size without however sacrificing any accuracy on reliability. 'Point Estimation Method', 'Response Surface Technique', 'Importance Sampling Procedure', 'Latin Hypercube Sampling' etc., are some of these methods. In this paper, a method called 'Importance Sampling Procedure is proposed for efficient reliability estimation. Since this method is used with the Importance Sampling, the number of simulation cycles required for the analysis can be much reduced.

The approximate methods, FORM and SORM, are efficient methods and known to provide sufficiently accurate results. However, it is known that these methods can in some instances become numerically unstable for complex formulations and one can not always be sure to obtain the global minimum using these methods (Sarveswaran and Roberts [33]). Therefore, the reliability analysis in this study was performed by simulation technique using importance sampling as variance reduction.

7. APPLICATION EXAMPLE

To demonstrate the application of the proposed procedure, a hypothetical steel box girder bridge is selected from an extensive parametric study aimed at the design of box girder bridge components.

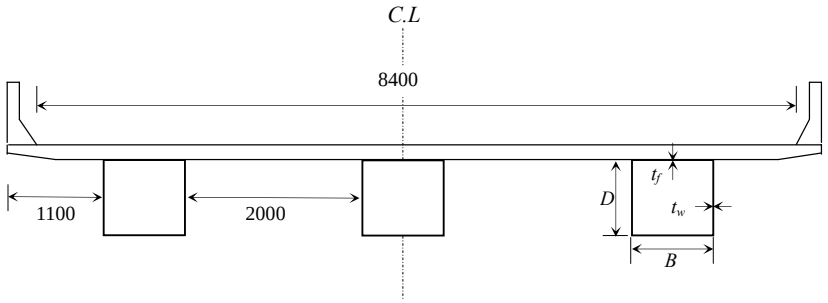

Figure 9. Typical Cross-section of Box-girder Bridge (Dimensions in mm)

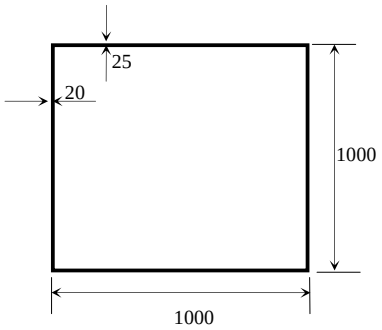

Figure 10. Dimensions (in mm) of Cross-section of Box Girder

Table 2. Values Used in Calculations (Lognormal Distributions)

Parameters	Mean μ	Standard deviation σ
Modulus of elasticity for steel, E	2.1×10^{5} N/mm^2	2.1×10^{4} N/mm^2
Yield stress in steel, σ_y	350 N/mm^2	35 N/mm^2
Corrosion parameter, A ($A < 200 \times10^{-3}$ mm)	70.6×10^{-3} mm	46.6×10^{-3} mm
Corrosion parameter, B ($B < 1.5$)	0.79	0.39

It is assumed that the bridge is not protected against corrosion. It has a simple span of 20 m and two lanes with traffic flowing in the same direction. The cross-section is shown in Figures 9 and 10. The material and corrosion parameters are assumed to be log-normally distributed (Sharifi and Paik [1,2]; Kayser and Nowak [6]; Czarnecki and Nowak [7]; Cheung and Li [8]; Kayser [17]; Sommer et al. [18]), and the mean values and standard deviations are shown in Table 2. The corrosion parameters chosen correspond to carbon steel in a marine environment (i.e., onshore near the coast) (see Table 1). The thicknesses of the deck and asphalt are 250 mm and 75 mm, respectively. The lifetime, T, chosen is 70 years. Deterministic analysis showed that, for each girder, prior to any corrosion, the nominal moment capacity is M_n = 9725 kN-m. In the probabilistic analysis, M_n is calculated using the statistical parameters shown in Table 2.

7.1 Dead Load

The mean value of the design dead load bending moment of the steel box girder is calculated, with the results shown in Table 3 for interior and exterior girders. To calculate the dead load for each girder, the dead load components for asphalt and the other components are first calculated separately, after which the equivalent dead load for each girder is calculated by estimating the mean and standard deviation of the components, as shown in Table 3.

Table 3. Dead Load for Girders (Normal Distributions)

Parameters	Mean μ	Standard deviation σ
Midspan dead load moment for interior girder, M_{DI}	15.50×10^{8} N-mm	1.44×10^{8} N-mm
Midspan dead load moment for exterior girder, M_{DE}	19.46×10^{8} N-mm	1.81×10^{8} N-mm

7.2 Live Load

Based on the specifications provided in Section 5.2, the mean and standard deviation of the live load for each girder are calculated and shown in Table 4.

Table 4. Live Load for Girders (Lognormal Distributions)

Parameters	Mean μ	Standard deviation σ
Midspan live load moment for interior girder, M_{LI}	18.58×10^{8} N-mm	3.34×10^{8} N-mm
Midspan live load moment for exterior girder, M_{LE}	22.92×10^{8} N-mm	4.13×10^{8} N-mm

7.3 Results

Probabilistic analysis was carried out to calculate the ultimate strength, reliability and probability of failure of the corroded box girders as the bridge ages. Figure 11 shows the trends of variation in the ultimate moment strength versus time. It can be seen that the ultimate bending strength of the corroded box girders is reduced with an increase in the age of the bridge. In addition, as expected, the ultimate moment decreases with an increase in the DOP at the same time.

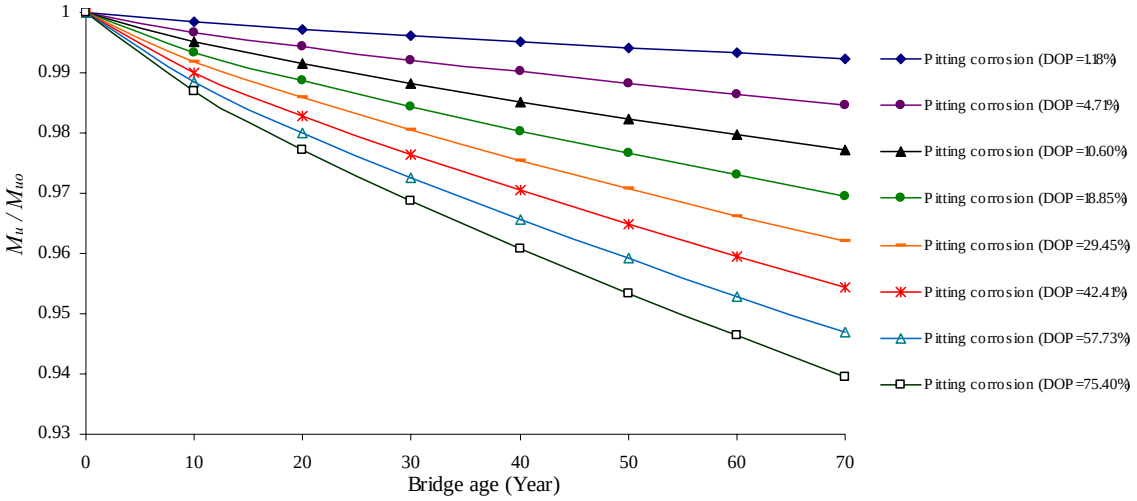

Figure 11. Variation of Box Ultimate Strength with Age

The reliability indices for two girders (interior and exterior) of a highway bridge that is assumed to be corroded localized with different DOP are demonstrated using reliability software, with the results shown in Figures 12 and 13. To derive reliability indices over time, it is usual to first find these indices for certain structural ages and then connect them together.

The reliability indices are calculated by simulation technique using the sampling analysis method for both interior and exterior girders. The results of simulation technique using sampling reliability analysis indicate that up to a bridge age of four years, there is no failure. The corresponding probabilities of failure are also calculated, and are presented in Tables 5 and 6 for interior and exterior girders, respectively. As expected, an increase in the DOP leads to an increase in the probability of failure.

Table 5. Failure Probabilities of Interior Girder

Bridge age (years)	Pitting corrosion (DOP)							
	1.18%	4.71%	10.60%	18.85%	29.45%	42.41%	57.73%	75.40%
Up to 4	No failure	No failure	No failure	No failure	No failure	No failure	No failure	No failure
4	No failure	No failure	No failure	No failure	No failure	No failure	0.00000451	0.000016
10	0.0000261	0.0000921	0.000137	0.000242	0.000306	0.000308	0.000431	0.000541
20	0.000313	0.000624	0.000851	0.001194	0.001507	0.002012	0.002579	0.002779
30	0.000739	0.001256	0.002038	0.002512	0.002979	0.003624	0.004041	0.004852
40	0.00118	0.002312	0.002868	0.003475	0.004388	0.005162	0.00591	0.006767
50	0.00169	0.002617	0.003779	0.004727	0.005697	0.006672	0.007571	0.008627
60	0.002077	0.003303	0.004733	0.005769	0.00699	0.008003	0.00913	0.009934
70	0.002331	0.003828	0.005283	0.006724	0.00819	0.008955	0.010222	0.011516

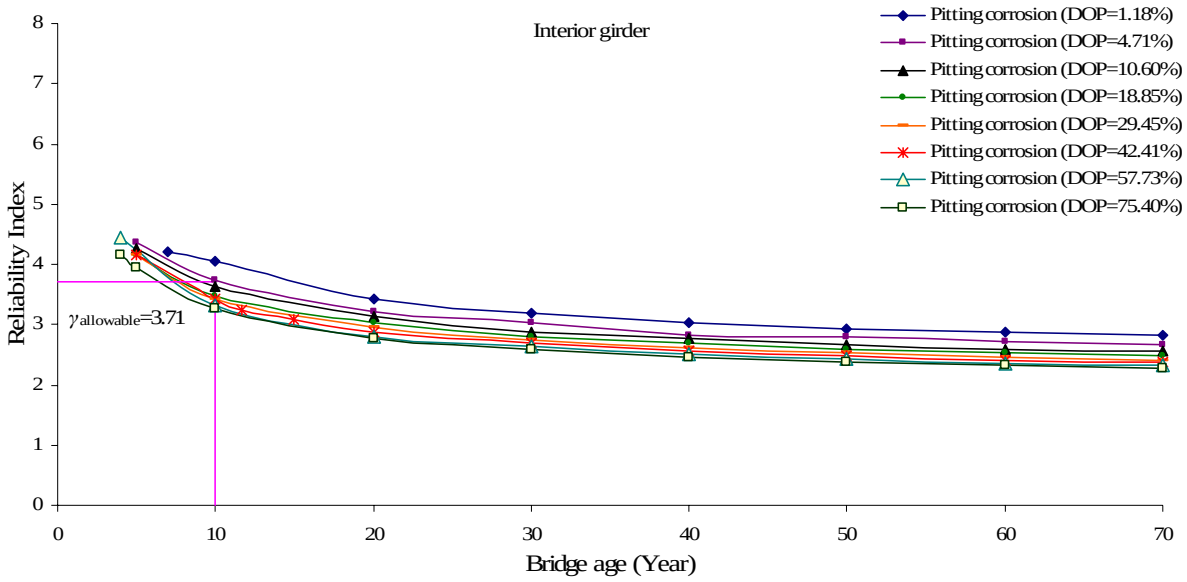

Figure 12. Variation in Reliability Index with Age for Interior Girder

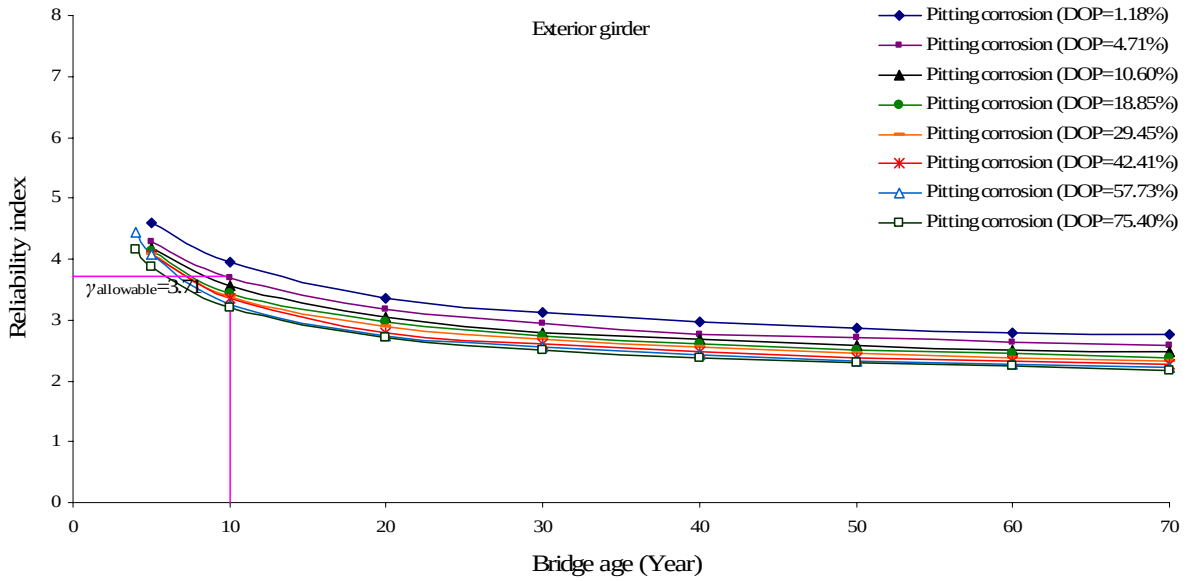

Figure 13. Variation in Reliability Index with Age for Exterior Girder

Table 6. Failure Probabilities of Exterior Girder

Bridge age (years)	Pitting corrosion (DOP)							
	1.18%	4.71%	10.60%	18.85%	29.45%	42.41%	57.73%	75.40%
Up to 4	No failure	No failure	No failure	No failure	No failure	No failure	No failure	No failure
4	No failure	No failure	No failure	No failure	No failure	No failure	0.00000451	0.000016
10	0.0000341	0.000116	0.000193	0.000309	0.000375	0.000393	0.000553	0.000699
20	0.000391	0.000768	0.001119	0.00151	0.001975	0.002589	0.003195	0.003472
30	0.000895	0.001601	0.002629	0.003084	0.003747	0.004535	0.005257	0.006015
40	0.001489	0.00291	0.003624	0.0045	0.005346	0.006444	0.007426	0.008664
50	0.002074	0.003348	0.004785	0.006077	0.007193	0.008597	0.00981	0.010807
60	0.002607	0.004307	0.005959	0.007242	0.008802	0.01022	0.011499	0.012508
70	0.002926	0.00486	0.00673	0.008617	0.010234	0.011289	0.01311	0.014607

This study considers the effects of pitting corrosion on the load-carrying capacity and reliability of a corroded steel box girder. The results of the reliability analysis plotted in Figures 12 and 13 give the minimum reliability index for assessment of the earliest time of the ultimate strength reliability of corroded steel box girder bridges.

8. ACCEPTANCE LEVEL OF RELIABILITY

To determine the latest time for the repair intervention of girders, it is first necessary to establish an acceptance level of reliability below which they may be considered unsafe. Not only the accuracy of resistance and load modeling has an influence on reliability but also there are several factors which cannot be modeled in structural reliability analysis. Practicing engineers generally prefer to quantify the reliability level that is implicit in current bridge codes and standards, which have a proven safety record, using probabilistic analysis and then employ this level as the acceptance level of reliability. This method is known as “calibration to existing codes and standards,” and is widely used to establish target reliability levels for design situations. The calibration procedure is discussed in many textbooks, e.g., Melchers [32]. It has also been applied to the quantification of the reliability levels implicit in bridge design and assessment codes (Nowak and Lind [34]; Flint et al. [35]; Chryssanthopoulos and Micic [36]). It is also recommended that acceptance levels be based on the consequences of failure and the nature of the failure mode. Therefore, the allowable reliabilities shown in Table 7, which are based on the type of failure has been used in this study.

Table 7. Target (or Acceptance) Reliability Levels (Sarveswaran and Roberts [33])

Failure consequences	Ductile failure with reserve strength	Ductile failure without reserve strength	Brittle failure
Not serious	3.09 (10^{-3})	3.71 (10^{-4})	4.26 (10^{-5})
Serious	3.71 (10^{-4})	4.26 (10^{-5})	4.75 (10^{-6})
Very serious	4.26 (10^{-5})	4.75 (10^{-6})	5.20 (10^{-7})

Corresponding Failure Probabilities are given in Parentheses.

The foregoing approaches were taken into account in selecting the time for repair intervention. For an example, the results for the worst condition of pitting corrosion (DOP = 75.40%) used in assessing the earliest time at which to order a repair. Applying the acceptance levels of the probability of failure, or a reliability index from 3.09 to 5.2, and employing reliability analysis results (Figures 12 and 13), the earliest time for the repair of both interior and exterior girders is around 10 and 4, respectively. In other words, if such a bridge is constructed now (in 2010), then it should be repaired in ten years’ time (in 2020). If it is already in existence and is older than ten years, then it is unsafe to use based on the assumptions and procedures reported here, which demonstrates that the repair intervention date.

In order to estimate the repair or renewal time in maintenance schedule of a damaged steel box girder bridge, first, the degree of intensity of pitting corrosion (DOP) must be calculated by the procedure which has been described in section 2. Then a target reliability (acceptance level of reliability below which they may be considered unsafe; e.g. Table 7) needed to be employed in order to calculate the earliest time by using the time-variant reliability profiles (Figures 12 and 13) that have been developed for the bridge.

For an instance, by a visual intervention of a corrosion damaged steel box girder plates bridge, the corroded area and hence the degree of intensity of pitting corrosion (Eq. 1) can be evaluated (e.g., DOP = 4.71%). By using Table 7, if the failure be serious and is ductile with reserve strength, the allowable reliability index will be 3.71. By employing this index for DOP = 4.71% and using Figures 12 and 13, the earliest time for both interior and exterior girders will be 10 years.

9. CONCLUDING REMARKS

This study has developed a probability-based procedure for selection of the critical time at which bridge girders should be repaired during their service life. Pitting corrosion with different degrees of intensity is considered. Reliability indices are calculated using available load and resistance models. A probabilistic ultimate strength model is developed by employing the simple analytical formulation. Bridge girders are subject to a loss in capacity over time due to pitting corrosion. The live load can be distributed to girders using the guidance formula for the highway bridge design. Time-dependent reliability indices can serve as the basis for selecting the latest time to repair or renew individual girders, with the critical components identified as those associated with the lowest reliability indices. It should be noted that, the procedure and approach that employed here in order to treat the effect of pitting corrosion on steel box girder bridges strength and reliability could be applicable and interesting.

From the developments and illustrations presented herein, the following conclusions can be drawn.

1. As expected, the ultimate strength of corroded box girders may decrease with time, although the degree of change (decrease) is greater in the first few years.

2. The ultimate limit analytical formula described in this study, and applied to the prediction of the ultimate strength of box girders, is useful for evaluating the time-variant steel box girder strength reliability of corroded bridges.

3. The numerical results reveal that the safety and reliability of the corroded steel box girders of a bridge may deteriorate during their service life (Figures 12 and 13), even though the nominal maximum moment may show little decrease in the same period. This phenomenon can be attributed to the high degree of variability in the slow mean corrosion. Even though the mean values of corrosion parameters A and B are moderate, large values close to the upper limits may have a considerable likelihood of occurrence, thus causing a significant reduction in the reliability of the corroded structures.

4. The procedures developed herein will be useful in assessing the ultimate strength reliability of aging steel box girder bridges by taking into account the degradation of plate members due to corrosion. This procedure is not only applicable to practicing engineers, but is also presented as a scientific method for estimating the longevity of bridges.

NOTATIONS

The following symbols are used in this paper:

A = corrosion parameter or cross-sectional area
A_B, A'_B, A_D = sectional area of outer bottom, inner or top
A_S = half of the sectional area of the side structure, including any longitudinal bulkhead
A_{pi} = surface area of the *ith* pit
A_0 = original cross-sectional area of the intact member
A_r = cross-sectional area involved in pit corrosion at the smallest cross-section
a = plate length
B = corrosion parameter
b = plate breadth
C = average corrosion penetration

D = height of the box
D_B = height of double bottom
DOP = degree of pit corrosion intensity as a ratio of the pitted surface area to the original plate surface area
d_r = diameter of the pit
E = Young's modulus
g = height of the neutral axis
$g(x)$ = the limit state function,
IM = dynamic live load
M_D = dead-load moment
M_L = live-load moment
M_n = nominal bending moment strength
M_u, M_{uo} = random variable representing the ultimate strength of a corroded or uncorroded box girder
n = number of pits
P_f = probability of failure
$p(X)$ = the joint probability density function of the random variables
R_{xr} = a factor of ultimate compressive strength reduction due to pit corrosion
T = lifetime of bridge
t = plate thickness of a member and time in years
V = Coefficient of variation
β = slenderness ratio of plating between longitudinal stiffeners
γ = reliability index
λ = bias factor
μ_x = mean value of random variable x_i
ρ = Coefficient of correlation
σ_B = ultimate compressive strength of a representative plate at the bottom shell
σ'_B = ultimate compressive strength of a representative plate at the inner bottom shell
σ_u = ultimate compressive strength of a plate
σ_{uD} , σ_{uS} = ultimate compressive strength of a representative plate at the upper or side shell
σ_{xi} = standard deviation of random variable x_i
σ_{xu} = ultimate compressive strength for a member with pit corrosion
σ_{xuo} = ultimate compressive strength for an intact (uncorroded) member
σ_y = mean yield strength of the material
σ_{yB} , σ_{yS} = mean yield strength of the bottom or side shell
ϕ = standard normal distribution function

ACKNOWLEDGEMENTS

The author is pleased to acknowledge the Vali-e-Asr University of Rafsanjan support.

REFERENCES

[1] Sharifi, Y. and Paik, J.K., "Ultimate Strength Reliability Analysis of Corroded Steel-box Girder Bridges", Thin-Walled Structures, 2011, Vol. 49, No. 1, pp. 157-166.
[2] Sharifi, Y. and Paik, J.K., "Environmental Effects on Ultimate Strength Reliability of Corroded Steel Box Girder Bridges", Structural Longevity, 2010, Vol. 18, No. 1, pp. 1-20.

[3] Sharifi, Y. and Rahgozar, R., “Evaluation of the Remaining Shear Capacity in Corroded Steel I-Beams”, International Journal of advanced Steel Construction, 2010, Vol. 6, No. 2, pp. 803-816.
[4] Sharifi, Y. and Rahgozar, R., “Remaining Moment Capacity of Corroded Steel Beams”, International Journal of Steel Structures, 2010, Vol. 10, No. 2, pp. 165-176.
[5] Sharifi, Y. and Rahgozar, R., “Fatigue Notch Factor in Steel Bridges Due to Corrosion”, Archives of Civil and Mechanical Engineering, 2009, Vol. IX, No. 4, pp. 75-83.
[6] Kayser, J.R. and Nowak, A.S., “Reliability of Corroded Steel Girder Bridges”, Structural Safety, 1989, Vol. 6, pp. 53-63.
[7] Czarnecki, A.A. and Nowak, A.S., “Time-Variant Reliability Profiles for Steel Girder Bridges”, Structural Safety, 2008, Vol. 30, No. 49-64.
[8] Cheung, M.S. and Li, W.C., “Serviceability Reliability of Corroded Steel Bridges”. Canadian Journal of Civil Engineering, 2001, Vol. 28, pp. 419-424.
[9] Kong, J.S. and Frangopol, D.M., “Cost–Reliability Interaction in Life-Cycle Cost Optimization of Deteriorating Structures”, Journal of Structural Engineering, 2004, Vol. 130, No. 11, pp. 1704-1712.
[10] Melchers, R.E. and Jeffrey, R.J., “Probabilistic Models for Steel Corrosion Loss and Pitting of Marine Infrastructure”, Reliability Engineering and System Safety, 2008, Vol. 93, pp. 423-432.
[11] Melchers, R.E., “The Effect of Corrosion on the Structural Reliability of Steel Offshore Structures”, Corrosion Science, 2005, Vol. 47, No. 10, pp. 2391-410.
[12] Thoft-Christensen, P., “Estimation of bridge reliability distributions.” Current and future trends in bridge design, construction, and maintenance, P. C. Das, D. M. Frangopol, and A. S. Nowak, eds., Thomas Telford, London, 1999, pp. 15–25.
[13] Paik, J.K., Lee, J.M. and Ko, M.J., “Ultimate Compressive Strength of Plate Elements with Pit Corrosion Wastage”, Journal of Engineering Maritime Environnent, 2003, Vol. 217, No. M4, pp. 185-200.
[14] Paik, J.K., Lee, J.M. and Ko, M.J., “Ultimate Shear Strength of Plate Elements with Pit Corrosion Wastage”, Thin-Walled Structures, 2004, Vol. 42, No. 8, pp. 1161-76.
[15] Nakai, T., Matsushita, H. and Yamamoto, N., “Effect of Pitting Corrosion on the Ultimate Strength of Steel Plates Subjected to In-Plane Compression and Bending”. Journal of Marine Science and Technology, 2006, Vol. 11, No. 1, pp. 52-64.
[16] Daidola, J.C., Parente, J., Orisamolu, I.R. and Ma, K.T., “Residual Strength Assessment of Pitted Plate Panels”, SSC-394, Ship Structure Committee, Washington, DC, 1997.
[17] Kayser, J.R., “The Effects of Corrosion on the Reliability of Steel Girder Bridges”. PhD thesis, University of Michigan, Ann Arbor, Mich., USA, 1988.
[18] Sommer, A.M., Nowak, A.S. and Thoft-Christensen, P., “Probability-Based Bridge Inspection Strategy”, Journal of Structural Engineering, ASCE, 1993, Vol. 119, pp. 3520-3536.
[19] Komp, M.E., “Atmospheric Corrosion Ratings of Weathering Steels-Calculation and Significance”, Material Performance, 1987, Vol. 26, No. 42-44.
[20] Paik, J.K. and Thayamballi, A.K., “Ultimate Limit State Design of Steel-Plated Structures”, John Wiley & Sons, Ltd., Hoboken, New Jersey, USA, 2003.
[21] Paik, J.K., Thayamballi, A.K. and Lee, J.M., “Effect of Initial Deflection Shape on the Ultimate Strength Behavior of Welded Steel Plates under Biaxial Compressive Loads”. Journal of Ship Research, 2004, Vol. 48, pp. 45-60.
[22] Nowak, A.S. and Collins, K.R., “Reliability of Structures”, McGraw-Hill, Thomas Casson, Boston, USA, 2000.
[23] Nowak, A.S., “Live Load Model for Highway Bridges”, Journal of Structural Safety, 1993, Vol. 13, pp. 53-66.

[24] Nowak, A.S., “Calibration of LRFD Bridge Code”, Journal of Structural Engineering, ASCE, 1995, Vol. 121, pp. 1245-1251.
[25] Nowak, A.S. and Szerszen, M.M., “Bridge Load and Resistance Models”, Engineering Structures, 1998, Vol. 20, pp. 985-990.
[26] Nowak, A.S. and Szerszen, M.M., “Structural Reliability as Applied to Highway Bridges”, Progress in Structural Engineering Materials, 2000, Vol. 2, pp. 218-224.
[27] AASHTO LRFD, “Bridge Design Specifications, American Association of State Highway and Transportation Officials”, Washington, D.C., 2004.
[28] Barker, R.M. and Puckett, J.A., “Design of Highway Bridges and LRFD Approach”, John Wiley & Sons, Inc., Hoboken, New Jersey, USA, 2007.
[29] Mansour, A.E., “An Introduction to Structural Reliability Theory”, Ship Structure Committee, Report No. SSC-351, 1990.
[30] Achintya, H. and Mahadevan, S., “Probability, Reliability and Statistical Methods in Engineering Design”, John Wiley & Sons, Inc., Hoboken, New Jersey, USA, 2000.
[31] Lemarie, M., “Structural Reliability”, John Wiley & Sons, Inc., Hoboken, New Jersey, USA, 2009.
[32] Melchers, R.E., “Structural Reliability Analysis and Prediction”, Wiley, Chichester, UK, 1999.
[33] Sarveswaran, V. and Roberts, M.B., “Reliability Analysis of Deteriorating Structures-The Experience and Needs of Practicing Engineers”, Structural Safety, 1999, Vol. 21, pp. 357-372.
[34] Nowak, A.S. and Lind, N.C., “Practical Bridge Code Calibration”, Journal of Structural Division, ASCE, 1979, Vol. 105, pp. 497-510.
[35] Flint, A.R., Smith, B.W., Baker, M.J. and Manners, W., “The Derivation of Safety Factors for Design of Highway Bridges”, Proceeding of Conference on the New Code for the Design of Steel Bridges, Cardiff, March 1980.
[36] Chryssanthopoulos, M.K. and Micic, T.V., “Reliability Evaluation of Short Span Bridges”, Proceeding of International Symposium on the Safety of Bridges, ICE/HA, London, July 1996.

BEHAVIOR OF HIGH STRENGTH CFSST STUB COLUMNS WITH INNER CFRP TUBE UNDER AXIAL COMPRESSIVE LOAD

Guochang Li[1,*], Yan Lang[2] and Zhijian Yang[3]

[1] *School of Civil Engineering, Shenyang Jianzhu University, Shenyang, 110168, China*
[2] *Department of Building Engineering, Suqian College, Jiangsu Province, 223800, China*
[3] *School of Civil Engineering, Tianjin University, Tianjin, 300072, China*
**(Corresponding author: E-mail: cegcli@sjzu.edu.cn)*

Received: 9 September 2010; Revised: 10 December 2010; Accepted: 13 December 2010

ABSTRACT: The contribution of CFRP (carbon fiber-reinforced polymer) to concrete-filled square steel tube (CFSST) is considered in this paper. Based on the experimental study of six high strength concrete-filled square steel tubular stub columns with inner CFRP circular tube (HCFSST-CFRP), the finite element software ABAQUS is employed to analyze the mechanical behaviors of HCFSST-CFRP stub column under axial compression load. Mechanism of interactions among steel tube, concrete core (includes two parts: innermost concrete and sandwich concrete) and CFRP is analyzed, and a simplified equation of loads shared by innermost concrete and sandwich concrete is given by regression analysis. Longitudinal stress distribution in the concrete section, load shared coefficient and axial load-strain relationships are presented. The confinement effect of the CFRP tube increases ductility of HCFSST stub columns remarkably. Innermost concrete suffers most of axial load after specimen reaching ultimate bearing capacity because of the confinement effect of CFRP tube. CFRP tube begins to work obviously at the descent stage after stub column reached ultimate bearing capacity.

Keywords: CFRP, Concrete-Filled square steel tube, Finite element, Test, Ultimate bearing capacity

1. INTRODUCTION

In recent years, with the development of steel and concrete composite structures, composite structures have attracted considerable attention. Because of the widely use of concrete-filled steel tube (CFST) structure, lots of research have been done by Schneider, Bridge, Han and others [1-5]. CFST members generally are divided into two types: square and circular. Zhong [6] presented that CFST has superior performance, like ductility and ultimate bearing capacity, compared with concrete-filled square steel tube (CFSST). However, CFSST structures have been used in some high-rise building in recently years [7-9]. Many solutions were presented to improve the performance of CFSST column, such as concrete-filled tube columns with confinement effect presented by Hu [10], CFSST columns with binding bars presented by Cai [11], composite-sectioned square concrete-filled steel tubes presented by Wang [12], concrete-filled square steel tubular columns reinforced by inner circular steel tube presented by Lu [13], and FRP-confined concrete-filled steel tubes presented by Tao [14]. Exploration and innovation of new material and structures is pushing the development of composite structures greatly. The research on application of carbon fiber material in CFST structures has become a popular issue.

On account of excellent mechanical properties of carbon fiber-reinforced polymer, a new type of composite column is proposed, which is constituted by inner CFRP tube, square steel tube and concrete core (includes two parts: innermost concrete and sandwich concrete) infilled. The test of six high strength concrete-filled square steel tubular stub columns with inner CFRP circular tube (HCFSST-CFRP) were conducted in this paper.

2. TEST

2.1 Specimen Preparation

Cold-formed square tube was used in the test. Width to thickness ratios range from 33 to 55, and thickness of CFRP tube ranges from 0.334 to 0.668 (thickness of adhesive excluded). The cross-section properties of specimens are listed in Table 1. The specimen number (for example: AS42) in Table 1 is labeled as follows: A stands for axial compression load; S stands for stub column; The first number stands for the thickness of steel tube, which means 3.5mm, 4.5mm and 5.8mm respectively; The second number stands for the layers of CFRP which is two or four layers. B is cross section height of square steel tube; t is the thickness of square steel tube; L is the length of specimen; α is steel ratio, expressed as $\alpha=A_s/A_c$, where A_s is steel cross-sectional area and A_c is concrete cross-sectional area; β is carbon fiber ratio, expressed as $\beta= A_f/A_c$, where A_f is CFRP cross-sectional area; ξ_s is steel confinement factor, expressed as $\xi_s=\alpha(f_y/f_{ck})$, where f_y is yield strength of steel and f_{ck} is characteristic concrete strength ($=0.4f_{cu}^{7/6}$ presented by Yu [15], where f_{cu} is cubic compressive strength). ξ_f is CFRP confinement factor, expressed as $\xi_f=\beta(f_f/f_{ck})$,where f_f is the tensile strength of CFRP. N_{ue} is experimental ultimate bearing capacity of test. N_{be} is experimental bearing capacity when CFRP ruptures.

Unidirectional carbon fiber sheets (CFS) were manufactured by Toray Industries in Japan, with weight is 300g/m^2 and width is 500mm. PVC tube with diameter of 125mm was used as mold. JGN-C adhesive manufactured by Liaoning Building Science Research Institute was used. The preparation process of the CFRP tube is shown as follows: Firstly, unidirectional carbon fiber sheet was cut into pieces as designed. Secondly, plastic membrane was wrapped around PVC tube in order to demount CFRP tube more easily. Thirdly, carbon fiber pieces were pasted around mold PVC tube with fibers oriented in the lateral direction of the PVC tube. Meanwhile gas bubbles between carbon fiber layers should be excluded in time. After air-drying for 4 hours, another carbon fiber piece was pasted over the former layer, as shown in Figure 1(a). The surface of the fabricated CFRP tube is too uneven to measure the thickness. So the thickness of adhesive wasn't considered in the fabricated CFRP tube.

Table 1. Specimen Schedules

No.	Specimen	$B\times t$	L	α	β	ξ_s	ξ_f	$N_{ue}(N_{be})$
1	AS42	200mm×4mm	600mm	0.0739	0.0107	0.369	0.748	3044kN（3089kN）
2	AS44	200mm×4mm	600mm	0.0739	0.0215	0.369	1.5	3259kN（3484kN）
3	AS52	200mm×5mm	600mm	0.0965	0.0107	0.458	0.748	3274kN（3302kN）
4	AS54	200mm×5mm	600mm	0.0965	0.0215	0.458	1.5	3299kN（3875kN）
5	AS62	200mm×6mm	600mm	0.1269	0.0107	0.689	0.748	3725kN（3694kN）
6	AS64	200mm×6mm	600mm	0.1269	0.0215	0.689	1.5	3755kN（4592kN）

With simple galvanized iron frame, the fabricated CFRP tube was fixed in the centre of the square steel tube, as shown in Figure 1(b). All the specimens were cast with one batch of ready-mixed and self-compacting concrete of designed strength of C60. After concrete curing for two weeks, angle grinding machine with diamond cutter was used to grind concrete and CFRP which were higher than the top cross-section of steel tube. This was to ensure that the load was applied evenly on the cross-section of specimen and simultaneously to the steel and concrete. Properties of steel, concrete and CFRP are shown in Table 2.

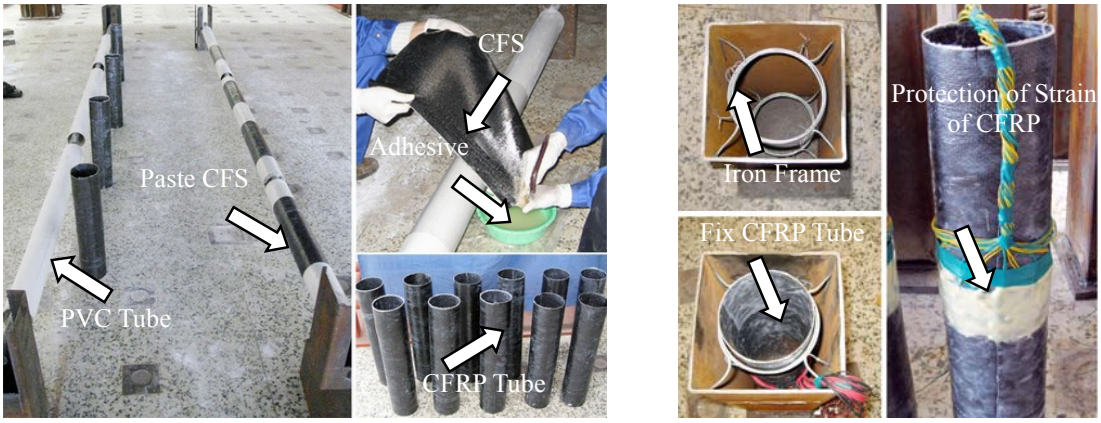

(a) The Fabrication of CFRP Tube (b) Assembly View

Figure 1. The Fabrication of Specimen

Table 2. Material Properties

Material (grade)	Yield strength	Tensile strength (Cubic Compressive strength)	Elastic modulus	Poisson's ratio
Steel (Q235)	291MPa	418MPa	201GPa	0.29
Concrete (C60)		(62.7MPa)	38.1GPa	0.184
CFRP (T700-12k/300g)		3718MPa	292GPa	0.308

2.2 Testing Equipment

All the tests were performed on a 5000kN capacity testing machine. Figure 2 gives a schematic view of the test arrangements. In order to measure exactly deformation of specimen, eight strain gauges were pasted on the surface of each steel tube, and sixteen strain gauges were pasted symmetrically around the CFRP tube. Two linear voltage displacement transducers (LVDTs) were used to measure the axial deformation, as shown in Figure 2.

Specimen and testing machine were adjusted and aligned to make sure that the cross groove on the plate of testing machine align with middle of plate of the specimen. Preload specimen according to load interval of less than 1/10 of the estimated ultimate bearing capacity until load achieved about 30% of the estimated ultimate bearing capacity. Grade loading pattern was applied in the test and each load interval was maintained for about 2–3min. The progress of deformation, the mode of failure, and the maximum load of the specimens were duly recorded.

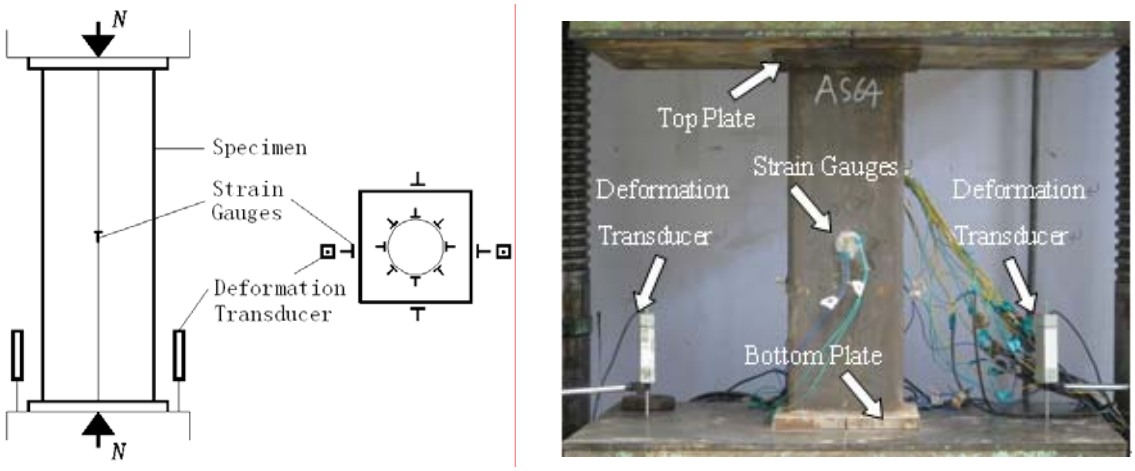

(a) Schematic View (b) Test View

Figure 2. View of the Test Setup

2.3 Test Results

In the progress of the test, deformation of specimen was not obvious, and bearing capacity (N) was in linear relation with average axial strain (ε) at preliminary stage of loading. When load attained 80% ~ 90% of ultimate bearing capacity, the growth rate of load apparently slowed. Meanwhile continuous sharp and snapping clack came from the harden colloids of CFRP in specimen. As load attained peak value followed by descend trend, steel tube began to show clear signs of wall buckling. Local buckling occurred equally on each side of the square tube and become more and more obvious, with higher apparent distortions. Then the load, rebounded back after short dropping, increased in linear relation with longitudinal strain. A sudden loud noise came from inner of the specimen indicated CFRP ruptured, right followed by indicator of testing machine dropped backwards. The bearing capacity of specimen sharply reduced, and specimen failed.

HCFSST-CFRP stub column has a good advantage in mechanical performance compared with normal column after plastic buckling of square steel tube happened. The CFRP tube can improve ductility of normal CFST column remarkably.

The loads (N) versus average axial strain (ε) curves of HCFSST-CFRP stub column are shown in Figure 3. It indicates that confinement of CFRP tube can improve ductility of normal CFST stub column, and specimen with thicker wall of CFRP tube has better ductility. The rupture bearing capacity (when CFRP start to rupture) of the HCFSST-CFRP stub column under axial compression load will rebound, and the value even exceed ultimate bearing capacity. For instance rupture bearing capacity of specimen of AS64 (thickness of CFRP is 0.668mm) was improved by 22%, and average axial strain attained 28547$\mu\varepsilon$.

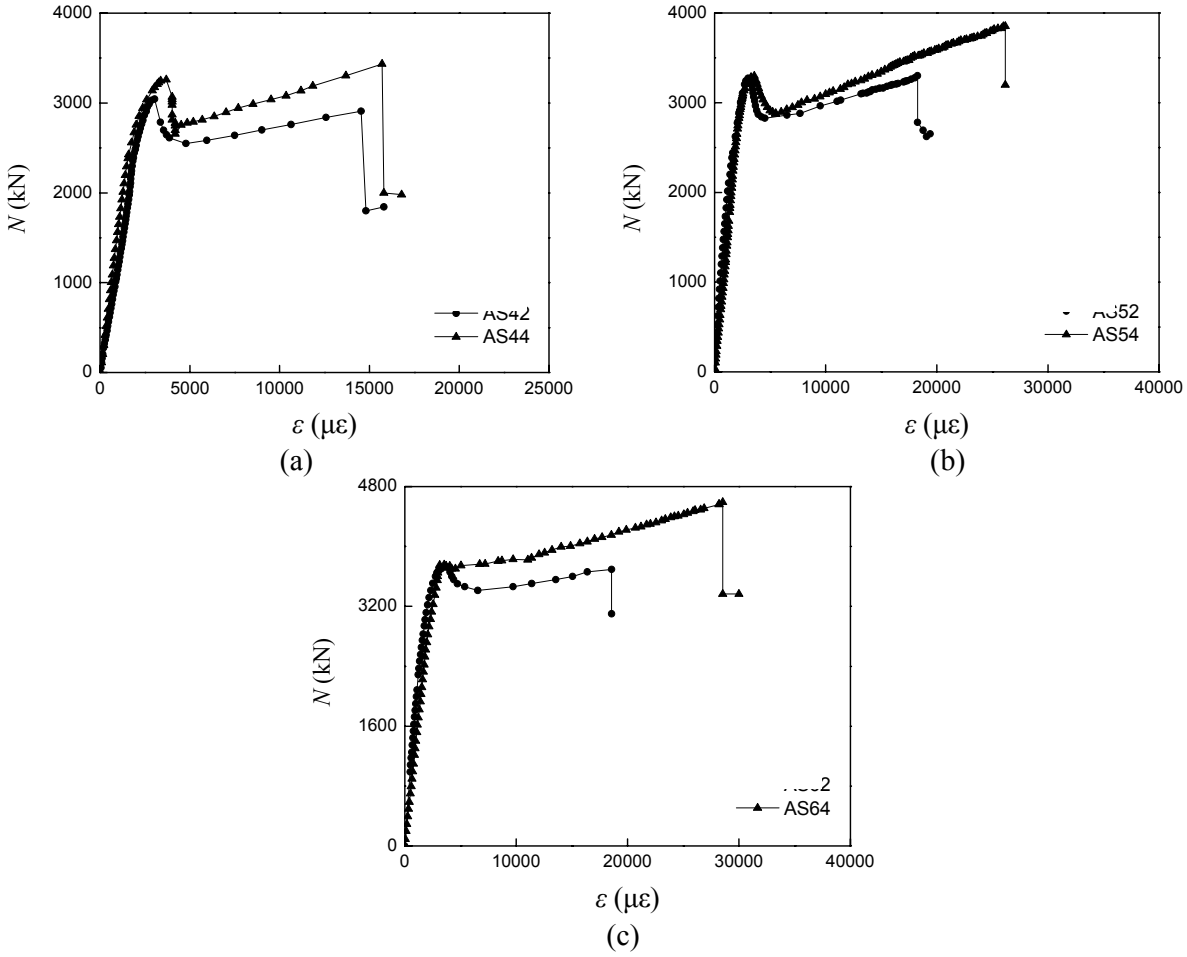

Figure 3. Experimental Axial Load (N) Versus Average Axial Strain (ε) Relationship

2.4 Analysis of Stress Distribution of CFRP

In the test, longitudinal and transverse strain gauges were pasted on CFRP tube at mid-height of specimen, with interval of 45 degrees. Changes of value of circumferential tangential strain were observed, and stress distribution of middle cross-section of CFRP tube was shown in Figure 4. According to the Figure 4, the changes of circumferential directional strain of CFRP are distributed very well, which means that tension of fiber of CFRP transferred well.

A few strain gauges were broken in processing of assembling specimen. In analysis, strain gauges that work properly were selected. It can be found that most of strain gauges work well and should have been bonding well with CFRP.

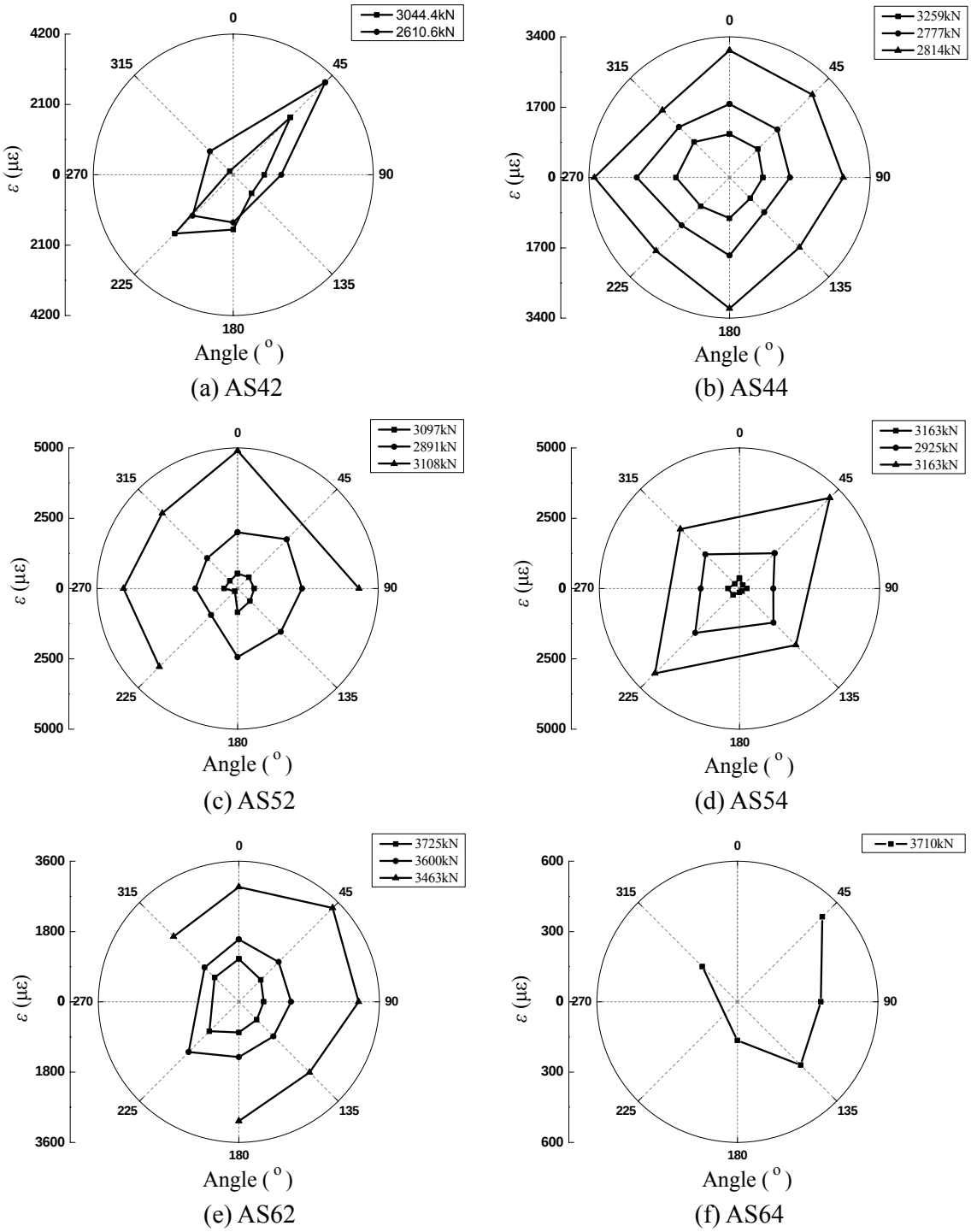

Figure 4. Stress Distribution of Middle Cross-section of CFRP Tube

3. FINITE ELEMENT ANALYSIS

3.1 Constitutive Model for Steel

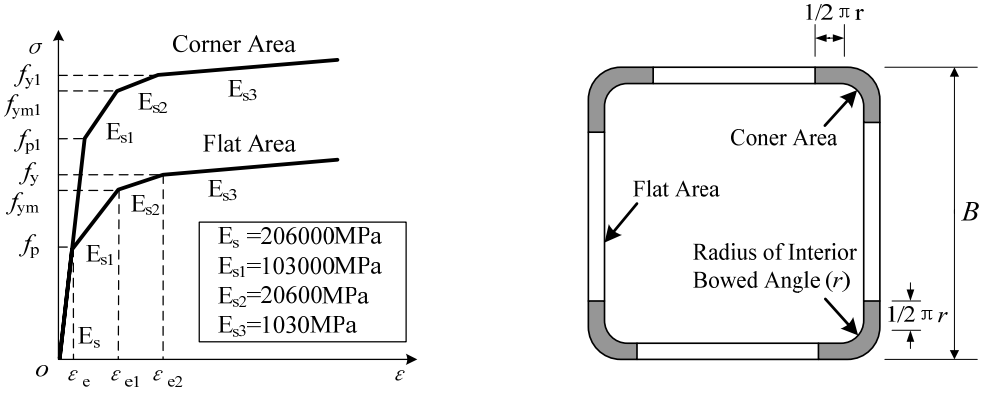

(a) Steel Stress (σ) - Strain (ε) Curves (b) Plate versus Corner Area of Steel Tube

Figure 5. Constitutive Model of Cold-formed Square Steel

Cold-formed steel tube was applied in the test, and steel tube section is divided into two zones: a corner zone and a flat zone, as shown in Figure 5. Abdel-Rahaman and Sivakumaran [16] presented the constitutive equation, which was applied to plate area of square tube, as following Eq. 1 shown.

$$\sigma = \begin{cases} E_s\varepsilon & (\varepsilon \le \varepsilon_e) \\ f_p + E_{s1}(\varepsilon - \varepsilon_e) & (\varepsilon_e \le \varepsilon \le \varepsilon_{e1}) \\ f_{ym} + E_{s2}(\varepsilon - \varepsilon_{e1}) & (\varepsilon_{e1} \le \varepsilon \le \varepsilon_{e2}) \\ f_y + E_{s3}(\varepsilon - \varepsilon_{e2}) & (\varepsilon_{e2} \le \varepsilon) \end{cases} \tag{1}$$

Where $\varepsilon_e = 0.75 f_y / E_s$, $\varepsilon_{e1} = \varepsilon_e + 0.125 f_y / E_{s1}$, $\varepsilon_{e2} = \varepsilon_{e1} + 0.125 f_y / E_{s2}$, $f_p = 0.75 f_y$, $f_{ym} = 0.875 f_y$.

According to the study of Karren and Winter [17] and Abdel-Rahman and Sivakumaran [16], following Eq. 2 is applied to calculate yield strength f_y of the corner area of square tube.

$$f_{y1} = [0.6\frac{B_c}{(r/t)^m} + 0.4] f_y \tag{2}$$

Where $B_c = 3.69(f_u / f_y) - 0.819(f_u / f_y)^2 - 1.79$, $m = 0.192(f_u / f_y) - 0.068$ and f_u is ultimate strength of steel. Therefore the format of the Equation (1) was still applied, and f_p、f_{ym} and f_y should be replaced by f_{p1}、f_{ym1} and f_{y1}.

3.2 Constitutive Model for Concrete

The concrete of concrete-filled steel tubular column is under triaxial compression while subjected to axially load. Therefore, the improvement of strength of concrete should be taken into account. Eq. 3 is applied in the paper [18].

$$y=\begin{cases}2x-x^2 & (x\leqslant 1)\\ \dfrac{x}{\beta_0(x-1)^{\eta}+x} & (x>1)\end{cases} \tag{3}$$

Where $x=\dfrac{\varepsilon}{\varepsilon_0}$, $y=\dfrac{\sigma}{\sigma_0}$, $\sigma_0=f_c^{'}$ ($f_c^{'}$ is cylinder compressive strength of concrete, which is expressed as $f_c^{'}=f_{cu}-8$), $\varepsilon_0=\varepsilon_c+800\cdot\xi_s^{0.2}\cdot 10^{-6}$, $\varepsilon_c=(1300+12.5\cdot f_c^{'})\cdot 10^{-6}$.

$\eta=1.6+1.5/x$, and $\beta_0=\dfrac{(f_c^{'})^{0.1}}{1.2\sqrt{1+\xi_s}}$.

3.3 Constitutive Model for CFRP

CFRP was considered as linear elasticity material in this paper. When the strain of carbon fiber achieves limited value ε_f, fiber rupture and CFRP lose load bearing capacity. The characteristic is expressed as following equation.

$$\begin{aligned}&\sigma_f=E_f\varepsilon && \varepsilon\leqslant\varepsilon_f\\ &\sigma_f=0 && \varepsilon>\varepsilon_f\end{aligned} \tag{4}$$

As Eq. 4 shows，when $\varepsilon=\varepsilon_f$, a value singularity occurs that value of strain change rapidly from limited value of ε_f to zero. However, for iterative calculation converge more easily, sudden change of value always be avoided. Therefore, the concept of damage was applied to model mechanism of CFRP. When strain of carbon fiber gets close to limited strain ε_f, the elastic-plastic characteristic is not obvious, and then CFRP ruptures suddenly. Plastic characteristic was not taken into account, and CFRP was considered as linear elasticity, as shown in Figure 6(a).

Unidirectional CFS along the hoop was used to fabricate the CFRP tube. "1" represents the direction along the fibers, "2" represents the direction perpendicular to the fibers on the plane of CFS and "3" represents the direction perpendicular to the plane of CFS, as shown in Figure 6(b). Lamina [19] model was applied in the finite element analysis (FEA) model of CFRP in elastic stage, and Hashin [19] damage model was applied to model mechanism of CFRP in the stage of rupture.

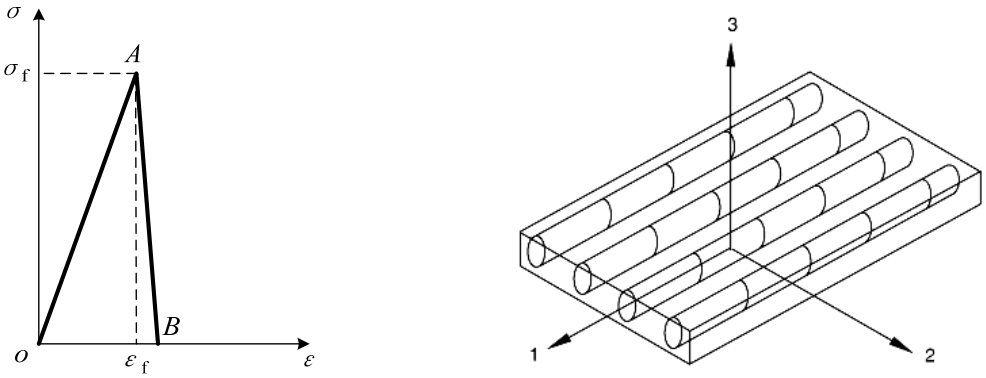

(a) CFRP Stress (σ) - Strain (ε) Curve (b) Sketch of Unidirectional Carbon Fiber Sheet (CFS)

Figure 6. CFRP Model

3.4 Results Comparison between FEM and Test

The results between FEM and test were compared. Figure 7 shows the load (N) and longitudinal strain (ε) curves of FEM and test. The FEM results are in agreement with the test results.

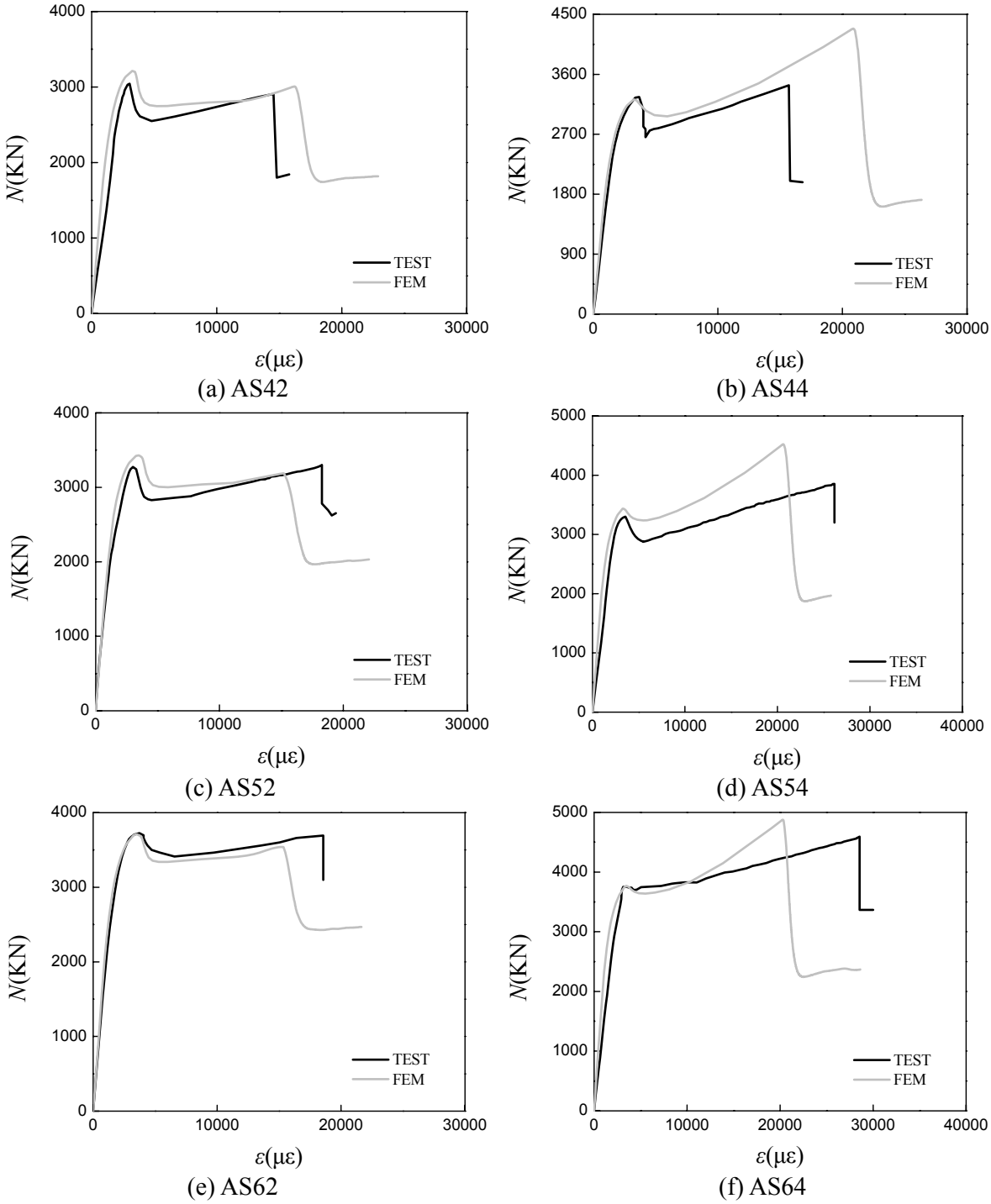

Figure 7. The Load (N) -Longitudinal Strain (ε) Curves of FEM and Test

3.5 Strain Field Analysis of Concrete Core

As Figure 8 shows, the typical axial load N versus longitudinal strain ε curve of HCFSST-CFRP stub column includes four line segments, which are first straight line, parabola, second straight line and break line.

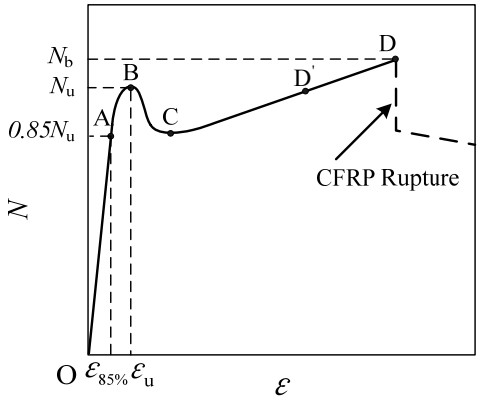

Figure 8. Typical Axial Load N Versus Longitudinal Strain ε Curve

(1) Elastic stage (OA): During this stage, steel tube and concrete core work alone, there is no obvious interaction among them. Tangential tension of CFRP is small. Point A represents the end of elastic stage, and also is the beginning of elastic-plastic stage.

(2) Elastic-plastic stage (AB): During this stage, crack in sandwich concrete keep developing under external load, and Poisson ratio of sandwich concrete begin to dominate steel. Restraint effect of steel tube to concrete core improved greatly. Cracks were found in the innermost concrete, all of the cracks were slight, because innermost concrete is restrained by steel tube and CFRP tube.

(3) Degraded stage (BC): Point B is a first extremum of N and ε curve. During this stage, load keep falling while longitudinal train increased.

(4) Rebound stage (CD): While longitudinal strain keep increasing, Poison ratio of innermost concrete increase rapidly. Therefore, during this stage, confinement effect of CFRP tube to innermost concrete increases, and the bearing capacity increases. The load rebounds to point D of the curve, and CFRP tube begins to rupture, load decrease sharply. To avoid conflicting with bearing capacity N_{ue} (point B), rupture bearing capacity N_{be} (point D) was defined. And, point D′ was also defined in order to avoid singularity of point D for FEM analysis.

Figure 9 shows the longitudinal concrete stress distribution of AS52 at characteristic point A, B, C, and D′ in Figure 8. It can be seen that concrete stress distribution is in elastic range, when load is small (according to point A). When specimen attains ultimate load (according to point B), Poisson ratio of concrete exceed steel due to the plastic deformation of concrete. As load continue to decrease to point C, discontinuity of sandwich concrete and innermost concrete is obvious. Concrete features are: longitudinal stress distribution is not even and discontinuous, like phenomenon fault in geotechnical engineering. As load rebound to near point D′, discontinuity becomes more serious and stress of innermost concrete is larger.

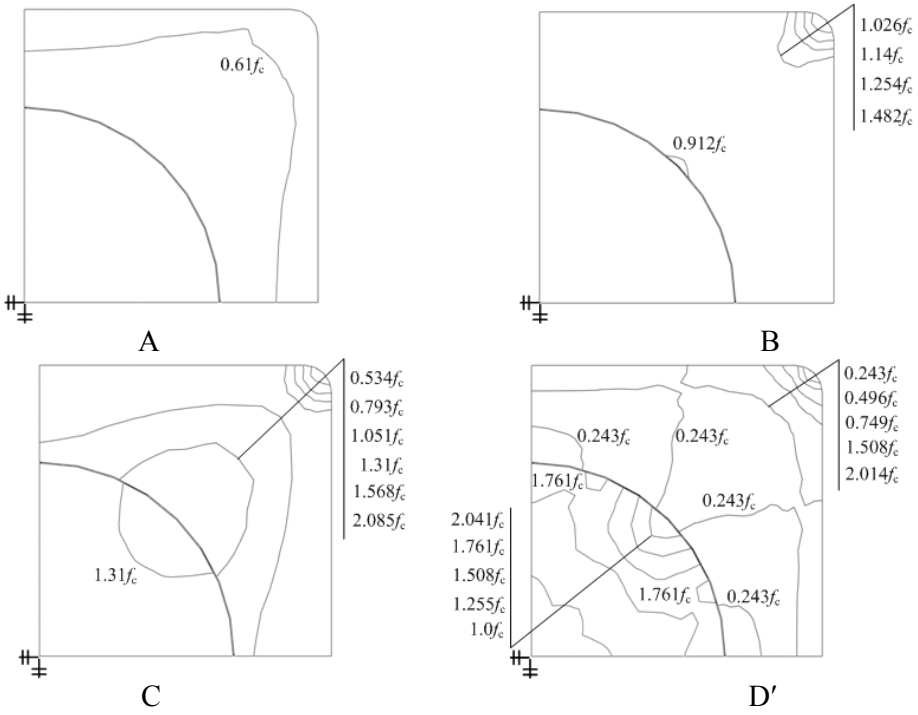

Figure 9. Longitudinal Concrete Stress Distribution of HCFSST-CFRP of A S52

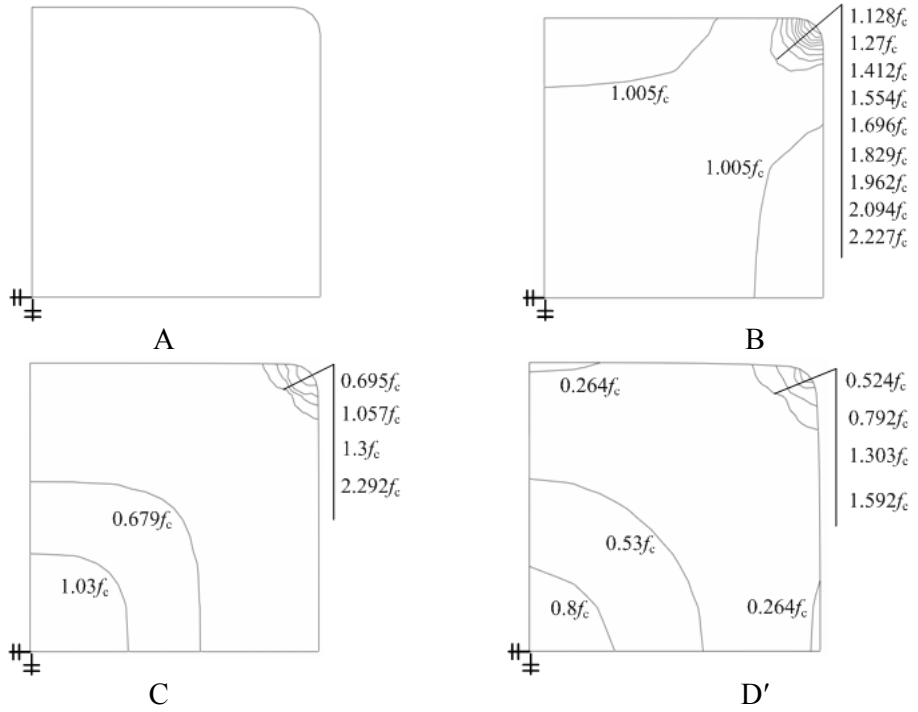

Figure 10. Longitudinal Concrete Stress Distribution of CFST of AS50

The longitudinal concrete stress distribution of CFST is shown in Figure 10. The longitudinal concrete stress distribution of CFST is relatively small, corresponding to point C on the N and ε curve. Because the confinement of concrete core subjected to steel tube is small after point C, longitudinal concrete stress distribution of CFST seems smaller.

The analysis results indicate that confinement effect of CFRP tube to innermost concrete mainly begins to work after steel tube buckling. Refinement of CFRP can improve the ductility of CFST remarkably in the beginning of degraded stage.

3.6 Analysis of Steel Tube

Because of characteristic of cold-formed steel tube, improvement of stress of the corner was taken into account. Model of steel tube in FEM was divided into corner area and plate area, and was assigned corresponding property. Figure 11 shows that Von Mises stress distribution of steel tube for 1/2 model. When load is small (according to point C of the curve), the value of Von Mises stress is within elastic limit. When load is bigger at point C of the curve, most part of the steel tube is in the plastic stage.

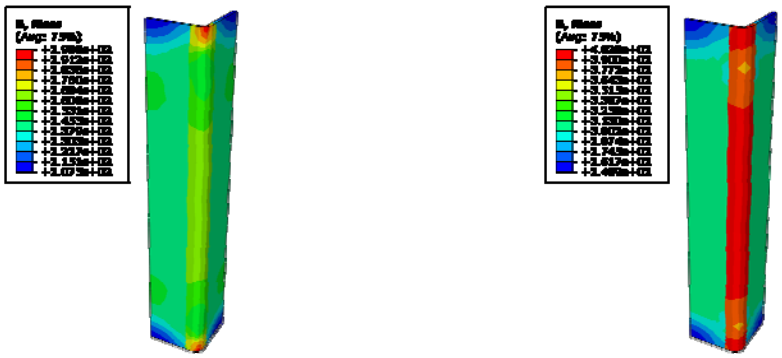

A B

Figure 11. Von Mises Stress Distribution of Steel Tube

3.7 Analysis of CFRP

Principle vector distributions of CFRP tube are shown in Figure 12, including four figures according to point A, B, C and D. Figure 12 shows that the orientation of principle vector is along tangential of CFRP. Principle stress distributions for CFRP tube are shown in Figure 13. When load is small, according to point A of typical curve, principle vector distributed dispersedly and principle stress was within 104.5 MPa. When load attains limit capacity, according to point B of typical curve, principle stress attains 571.8MPa, equivalent to 1/7 of limit value. According to point C of the typical curve, principle vector gathers in the middle area of CFST tube and maximum principle stress exceeds 1000MPa. With loading, maximum principle stress keeps increasing and stress distribute evenly in the whole area of CFRP tube.

It is plastic stage when CFRP starts to affect the ductility of specimen and works significantly around point C of typical curve. And when steel tube is in elasto-plastic stage, the hoop-tangential stress of CFRP is small.

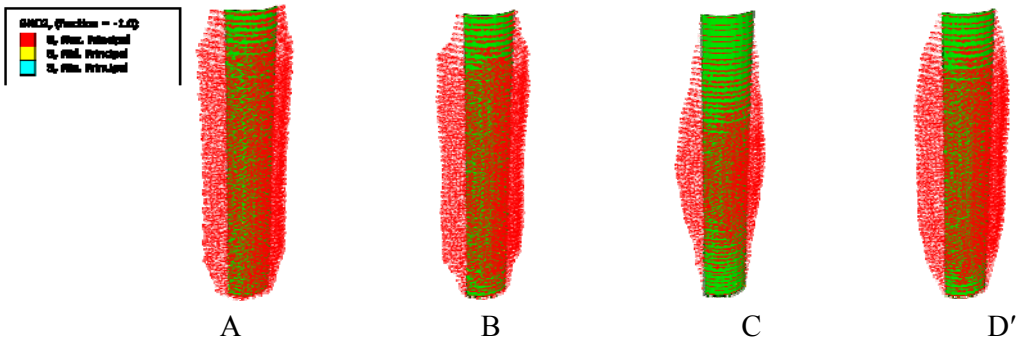

Figure 12. Principle Vector Distribution of CFRP for 1/2 Model

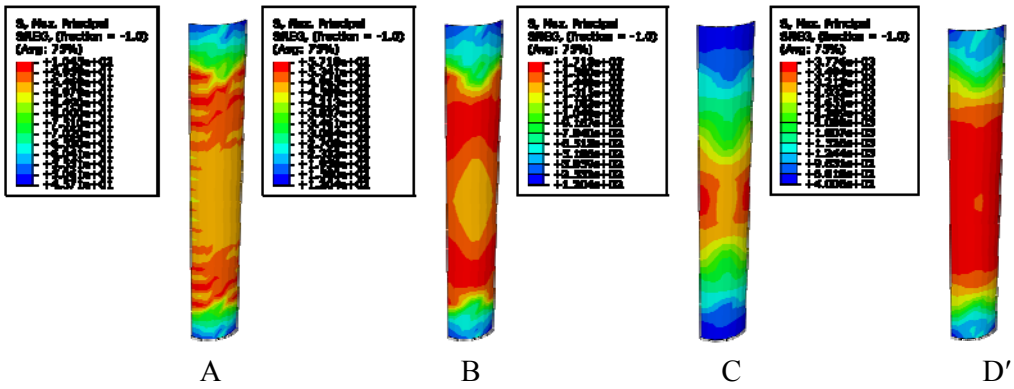

Figure 13. Maximum Principle Stress Distribution of CFRP for 1/2 Model

4. Analysis of Interactions among Steel, Concrete and CFRP

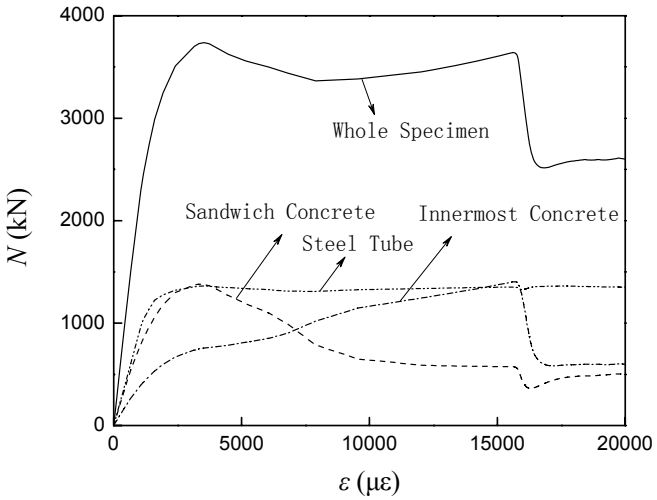

Figure 14. Load versus Longitudinal Stress Curve

Load (N) versus stress (ε) curve is shown in Figure 14. The load versus stress curve of steel shows that steel enters plastic stage after limit point. The load versus stress curve of sandwich concrete shows that the load shared by sandwich concrete decreases after peak of the curve. The load versus stress curve of innermost concrete shows that the load shared by innermost concrete increases after short plastic flow following peak of curve.

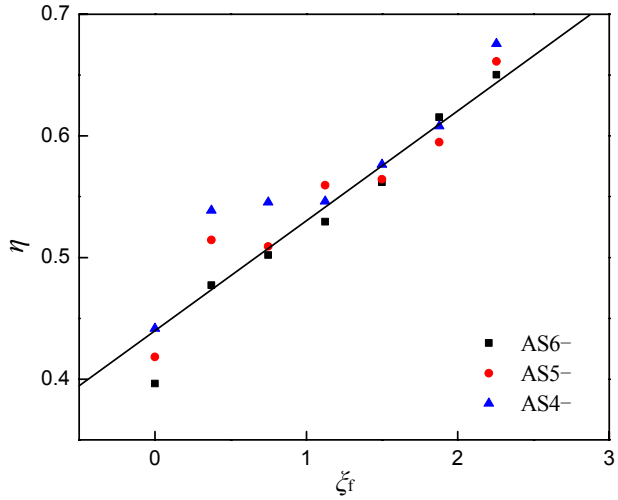

Figure 15. Load Shared Coefficient (η) – constraining Factor (ξ_f) when Load got Bearing Capacity

Based on the validity and reasonability of FEM, more finite element model was made to be calculated. Load shared coefficient (η)-constraining factor (ξ_f) at load achieved bearing capacity data distribution, as shown in Figure 15. Where η is the ratio of load shared by innermost concrete and sandwich concrete which is expressed as $\eta=N_{ic}/N_{sc}$. Where N_{sc} is load shared by sandwich concrete and N_{ic} is load shared by innermost concrete. Considering η is linear correlated with ξ_f , linear regression method is applied to deal with the distribution of data. The results of regression method show that load shared by innermost concrete (N_{ic}) increases with increase of restraining factor (ξ_f) of CFRP, as shown in the Eq. 5.

$$\eta = 0.09\xi_f + a \tag{5}$$

Where: $a=0.367+0.15\xi_s$

Load shared by sandwich concrete N_{sc} and load shared by innermost concrete N_{ic} relations can be established based on the following assumptions: (1) CFRP can not work under pressure and longitudinal load is totally shared by concrete core and steel tube. (2) Strengthening of steel is neglected after specimen attain limit capacity. According to assumptions, Load shared by sandwich concrete N_{sc} and load shared by innermost concrete N_{ic} of the member can be expressed as:

$$N_{sc} = \frac{1}{0.09\xi_f + a}(N_u - A_s f_{ya}) \tag{6}$$

$$N_{ic} = N_u - N_{sc} \tag{7}$$

Where f_{ya} is the weighted mean value of cross-section of cold-formed steel square tube can be calculated by $f_{ya} = Cf_{y1} + (1-C)f_y$, C is ratio of area of cross-section of corner and whole cross-section; f_{y1} is yield stress of steel of corner; N_u is bearing capacity; A_s is area of whole cross-section.

5. CONCLUSIONS

(1) CFRP tube can improve the ductility and bearing capacity of CFST column under axial compression. HCFSST-CFRP stub columns totally failed with CFRP rupture.

(2) CFRP tube begins to work obviously at the descent stage after stub column attained ultimate bearing capacity. Namely confinement effect of CFRP tube to innermost concrete mainly begins to work after steel tube buckled

(3) Longitudinal stress distribution of innermost concrete and sandwich concrete is discontinuous, and innermost concrete under confinement of CFRP suffers most of axial load.

(4) CFRP tube works well in the concrete of HCFSST-CFRP stub column. That means tension of circumferential directional fiber of CFRP transferred well.

(5) This paper presents a calculating formula to analyze the load shared by innermost concrete and sandwich concrete. And the experimental work in this paper lays a good foundation for further research on HCFSST-CFRP column.

ACKNOWLEDGEMENTS

This project was supported by National Science Foundation of China (50678106), Shenyang Talent Development Fund (2009140403038), Liaoning BaiQianWan Talents Program (2009921095), Technology Program of Ministry of Housing and Urban-Rural Development (2011-k3-23).

REFERENCES

[1] Schneider, S.P., “Axially Loaded Concrete-filled Steel Tubes”, Journal of Structural Engineering, ASCE, 1998, Vol. 124, No. 10, pp. 1125-1138.
[2] Han, L.H., “Tests on Stub Columns of Concrete-filled RHS Sections”. Journal of Constructional Steel Research, 2002, Vol. 58, No. 3, pp. 353-372.
[3] Bridge, R.Q., “Concrete Filled Steel Tubular Columns”, Rep. No. R283, School of Civil Engineering, University of Sydney, Sydney, Australia, 1976.
[4] Furlong, R.W., “Columns Rules of ACI, SSLC, and LRFD Compared”, Journal of the Structural Division ASCE, 1983, Vol. 109, No. 10, pp. 2375-2386.
[5] Shakir-Khalil, H. and Zeghiche, J., “Experimental Behavior of Concrete Filled Rolled Rectangular Hollow Section Columns”, The Structural Engineering, 1989, Vol. 67, No. 19, pp. 346-353.
[6] Zhong, S.T., “The Comparison of Behaviors and Economics for Concrete-filled Steel Tube (CFST) with Circular and Square Cross-sections”. Journal of Harbin Institute of Technology, 2003, Vol. 35, No. 8, pp. 27.
[7] Forbes, D., “Three Tall Buildings in Southern China”, Structural Engineering International, 1997, Vol. 7, No. 3, pp. 157-159.
[8] Mc Graw-Hill, “Structural System for Tall Buildings”, Council on Tall Buildings and Urban Habitat, New York, 1995.
[9] Han, L.H., “Some Recent Applications and Researches in Concrete-filled Steel Tubular Structures”, Siencepaper Online, Beijing, 2005.

[10] Hsuan, T.H., Huang, C.S., Wu, M.H. and Wu, Y.M., "Nonlinear Analysis of Axially Loaded Concrete-Filled Tube Columns with Confinement Effect", Journal of Structural Engineering, ASCE, 2003, Vol. 129, No. 10, pp. 1323.
[11] Cai, J. and He, Z.Q., "Eccentric-loaded Behavior of Square CFT Columns with Binding Bars", Journal of Building Structures, 2007, Vol. 28, No. 4, pp. 25-35.
[12] Wang, Z.H. and Cheng, R., "Axial Bearing Capacity of Composite-sectioned Square Concrete-filled Steel Tubes", Journal of Tsinghua University (Science and Technology), 2005, Vol. 12, pp. 1596-1597.
[13] Lu, T.Q. and Zhao, G..F., "Numerical Method for Analysis of Ultimate Strength of Concrete-filled Square Steel Tubular Columns Under Eccentric Compression Reinforced by Inner Circular Steel Tube", Journal of Dalian University of Technology, 2001, Vol. 41, No. 5, pp. 612.
[14] Tao, Z. and Zhuang, J.P., "Mechanical Behavior of Stub Columns of FRP-confined Concrete-filled Steel Tubes", Industrial Construction, 2005, Vol. 35, pp. 9.
[15] Yu, Z.W. and Ding, F.X., "Unified Calculation Method of Compressive Mechanical Properties of Concrete", Journal of Building Structures, 2003, Vol. 24, No. 5.
[16] Abdel-Rabman, N., "Sivakumaran K.S. Material Properties Models For Analysis of Cold-Formed Steel Members", Journal of Structural Engineering, 1997, Vol. 123, No. 9, pp. 113-1143.
[17] Karren, K.W. and Winter, G.., "Effects of Cold-Forming on Light-Gauge Steel Members", Journal of the Structural Division, ASCE, 1967, Vol. 93, No. 1, pp. 433-469.
[18] Liu, W., "Research on Mechanism of Concrete-Filled Steel Tubes Subjected to Local Compression", Fuzhou: Fuzhou University, 2005.
[19] ABAQUS Theory Manual, ABAQUS Analysis User's Manual.

SECOND-ORDER ANALYSIS OF 2-D STEEL FRAMES AT ELEVATED TEMPERATURES

J.Y.K. Chan [1], S.S.H. Cho [2] and F.G. Albermani [1,*]

[1] *School of Civil Engineering, The University of Queensland, Australia*
[2] *Department of Civil and Structural Engineering, The Hong Kong Polytechnic University, Hong Kong*
**(Corresponding author: E-mail: f.albermani@uq.edu.au)*

Received: 24 November 2010; Revised: 16 February 2011; Accepted: 25 February 2011

ABSTRACT: At elevated temperatures, the stress-strain relationship of steel will be nonlinear. When one of the columns of a steel frame is subject to a local fire, the material properties of the column will deteriorate locally. Although the column is weakened, the steel frame will not collapse immediately if the frame is robust enough so that the excessive internal forces of the column can be redistributed by its connecting members. Structural design with robustness consideration can prevent a steel building under local fire from collapse. This paper is to propose a second-order analysis and design method for 2-D steel frames considering the nonlinear stress-strain relationship of the material under elevated temperatures. Results are found to be in line with the Eurocode 3 predicted failure loads.

Keywords: Steel, Column, Frame, Fire, Elevated temperature, Second-order analysis

1. INTRODUCTION

There is an increasing trend of constructing skyscrapers today because of the scarcity of lands and the rapid growth of population. Because of the huge amount of construction materials required to build a skyscraper, the construction materials are bound to be light-weight. Therefore, among the common construction materials, steel is most widely used due to its light weight and high strength. However, the height of the skyscraper and the huge amount of occupants it accommodates make the evacuation more difficult in case of fire. Steel is particularly vulnerable to high temperature. Its material properties start to deteriorate at temperature as low as 100°C. At 600°C its design strength is almost reduced to half and at 1200°C it will lose all its strength. Although intense local fire weakens structural member rapidly, progressive collapse can be avoided if the structure is designed properly so that it is robust to the local failure. For instance, redundant members can provide an alternative load path in case of fire. Therefore, it is important to study the structural behaviour of steel structures under fire. The structural behaviour of a steel structure under fire is rather complicated not only because of the strength degradation of steel at elevated temperatures, but also because of the change in geometry due to thermal expansion. If free expansion is prevented, thermal stress will also be developed. Eurocode 3 Part 1-2 [1] provides reduction factors of yield strength and modulus of elasticity for the stress-strain relationship for steel at elevated temperatures. To determine the strength of steel columns at a specific temperature, the same formulas for calculating the buckling strength at ambient temperature [2] can be adopted. In this paper, a two-dimensional steel frame is made up to demonstrate the effect of a localized fire with different temperatures at a column to the global frame using second-order analysis in which the P-Δ and the P-δ effects are taken into account. Although research on finite element modelling of steel columns and framed structures at elevated temperatures has been carried out extensively over the past three decades, this paper aims to develop a simplified fire engineering approach based on the design values of the material properties given in Eurocode 3 Part 1-2 [1].

2. LITERATURE REVIEW

Extensive research on large-scaled laboratory tests on unprotected or protected steel structures under fire has been carried out over the past few decades. In general, there are two types of tests. In the first type, the test is carried out in a transient state in which a constant load is applied to the column while the temperature is increased; while in the second type, the test is carried out in a steady state that the temperature is held constant at a pre-determined level and the load is applied incrementally until the column fails. The majority of the fire tests focus on structural behaviour of individual steel members under fire conditions. For example, Franssen et al. [3], Yang et al. [4] and Yang and Hsu [5], etc, carried out laboratory tests on isolated steel columns under fire condition. While most of the design codes [1,6,7] provide design recommendations for fire condition, they are developed mainly based on experimental observations. However, since these tests are carried out on isolated members mainly with concentric loads and simple end conditions, the true interaction between the column and its adjacent members cannot be reflected. Janss [8] conducted research on estimating the effective lengths of steel columns from the experimental data from Janss and Minne [9]. Statistical analysis was carried out to estimate the effective length factors which were found to be in good accordance with the values given in Eurocode 3 Part 1-2 [1] which are 0.5 for continuous columns and 0.7 for columns in the top storey. Ali and O'Connor [10] carried out parametric experimental investigation on rotationally and axially restrained steel columns in fire which were connected to steel plates. With the rotational and axial restraints, additional force is generated during the fire condition. Based on the results, values of effective length factors were proposed for steel columns with different degrees of restraints. Wang and Davies [11] conducted fire tests on column assemblies in which two restraining beams are connected to the web of the column so that rotational restraint about principal major axis is provided. It was concluded that the estimated effective lengths of the steel columns were shorter than that assuming pinned at both ends. Tan et al. [12] also carried out similar research on the structural responses of restrained steel columns over a range of slenderness ratio at elevated temperatures. In their study, the initial crookedness and load eccentricity were carefully examined. Their results pointed out that the presence of these initial imperfections posed an important factor to the failure temperatures of the steel columns. Wald et al. [13] carried out experimental research on full-scale fire tests, known as the Cardington fire tests, which involved an eight-storey steel framed building. Through the laboratory test, the structural behaviours of the beams, columns, connections and composite slabs of the steel-framed structure as a typical office building under fire conditions were carefully studied.

Since full-scale fire tests on structures are expensive and time consuming, numerical methods are more preferable. Wang [14] carried out numerical analysis of the global structural behaviour using the finite element computer program FIREFRAME researched by Wang and Moore [15] and compared the experimental results from the Cardington fire tests. Although numerical results suggested that the slab tensile membrane action enhanced the fire resistance of the steel columns which agreed with the experimental results, structural behaviour of columns could not be assessed due to the relatively low temperature. Chen and Young [16] studied the structural behaviour of high strength steel columns at elevated temperatures using the finite element program ABAQUS [17] with both pinned-end and fixed-end conditions considered. In the analysis, the initial imperfections were taken into account and model for stress-strain relationship of high-strength steel was proposed. The results of the finite element modelling were verified against experimental data of columns at ambient and elevated temperatures available in the literature. It was shown that the European and American specifications [1,7] conservatively predicted the column strengths of high strength steel at elevated temperatures.

3. MECHANICAL PROPERTIES OF STEEL AT ELEVATED TEMPERATURES

This paper adopts the idealized stress-strain relationship of steel at elevated temperatures given in Eurocode 3 Part 1-2 [1]. As shown in Figure 1, at the beginning a linear elastic range is observed with the slope $E_{a,\theta}$ before the proportional limit $f_{p,\theta}$ is reached. After that proportional limit the slope starts to be gentler and finally flatten out at effective yield strength $f_{y,\theta}$ where the strain reaches yield strain. The stress σ and the tangent modulus $E_{t,\theta}$ at the nonlinear range are given by the following equations.

$$\sigma = f_{p,\theta} - c + \frac{b}{a}\sqrt{a^2 - \left(\varepsilon_{y,\theta} - \varepsilon\right)^2} \tag{1}$$

$$E_{t,\theta} = \frac{b}{a}\frac{\varepsilon_{y,\theta} - \varepsilon}{\sqrt{a^2 - \left(\varepsilon_{y,\theta} - \varepsilon\right)^2}} \tag{2}$$

where $\varepsilon_{y,\theta} = 0.02$

$$a^2 = \left(\varepsilon_{y,\theta} - \varepsilon_{p,\theta}\right)\left(\varepsilon_{y,\theta} - \varepsilon_{p,\theta} + \frac{c}{E_{a,\theta}}\right)$$

$$b^2 = c\left(\varepsilon_{y,\theta} - \varepsilon_{p,\theta}\right)E_{a_\theta} + c^2$$

$$c = \frac{\left(f_{y,\theta} - f_{p,\theta}\right)^2}{\left(\varepsilon_{y,\theta} - \varepsilon_{p,\theta}\right)E_{a,\theta} - 2\left(f_{y,\theta} - f_{p,\theta}\right)}$$

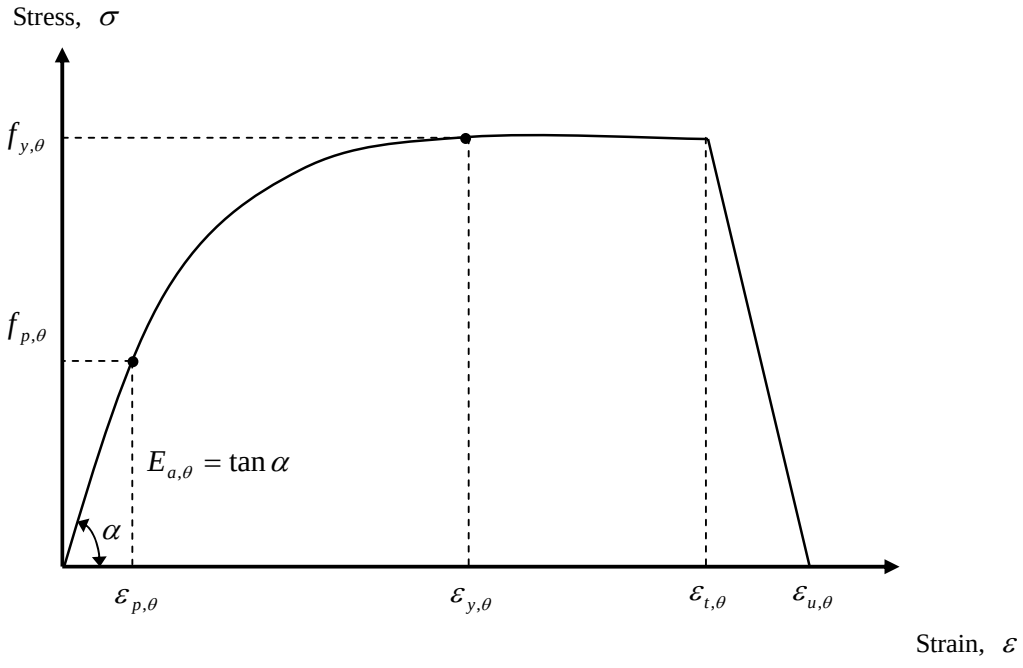

Figure 1. Stress-strain Relationship for Carbon Steel at Elevated Temperatures

Notations: $f_{p,\theta}$: proportional limit
$f_{y,\theta}$: effective yield strength
$E_{a,\theta}$: slope of the linear elastic range
$\varepsilon_{p,\theta}$: strain at proportional limit
$\varepsilon_{y,\theta}$: yield strain
$\varepsilon_{t,\theta}$: limiting strain for yield strength
$\varepsilon_{u,\theta}$: ultimate strain

The mechanical properties of carbon steel at 20°C, 200°C, 400°C, 600°C, 800°C , 1000°C and 1200°C given in Eurocode 3 Part 1-2 [1] are summarized in Table 1. For temperatures below 400°C, an alternative stress-strain relationship for carbon steel allowing for strain hardening is provided. However, for simplicity as allowed in the design code [1], strain-hardening of steel is not considered in the investigation. With these properties, the exact stress-strain relationship at the nonlinear range where $\varepsilon_{p,\theta} < \varepsilon < \varepsilon_{y,\theta}$ at different heat levels can be calculated by the above formulas. It should be noted that the nonlinear stress-strain relationship applies to both tension and compression. For thermal properties, in Eurocode 3 Part 1-2 [1], the relative thermal elongation is given by Eqs. 3a–3c. However, in this paper, a coefficient of linear thermal expansion of 1.4×10^5 is adopted for simplicity.

For $20°\text{C} \le \theta_a \le 750°\text{C}$,

$$\Delta l/l = 1.2\times10^{-5}\theta_a + 0.4\times10^{-8}\theta_a^2 - 2.416\times10^{-4} \tag{3a}$$

For $750°\text{C} \le \theta_a \le 860°\text{C}$,

$$\Delta l/l = 1.1\times10^{-2} \tag{3b}$$

For $860°\text{C} \le \theta_a \le 1200°\text{C}$,

$$\Delta l/l = 2\times10^{-5}\theta_a - 6.2\times10^{-3} \tag{3c}$$

where l is the length at ambient temperature
Δl is the temperature induced elongation
θ_a is the steel temperature (°C)

Table 1. Mechanical Properties of Steel at Elevated Temperatures

Steel Temperature θ (°C)	Effective Yield Strength $f_{y,\theta}/f_y$	Proportional Limit $f_{p,\theta}/f_y$	Slope of the Linear Elastic Range $E_{a,\theta}/E_a$
20	1.000	1.000	1.000
200	1.000	0.807	0.900
400	1.000	0.420	0.700
600	0.470	0.180	0.310
800	0.110	0.050	0.090
1000	0.020	0.025	0.045
1200	0.000	0.000	0.000

4. THE SECOND-ORDER ANALYSIS BY NIDA

NIDA [18] is a commercial nonlinear analysis and design software developed by the Hong Kong Polytechnic University which can achieve performance-based design. By considering the second-order P-Δ and P-δ effects with allowance for the initial member imperfections during analysis, the failure load of the structure can be accurately determined without considering the effective length for individual column members. In the current study, the analysis adopts a similar approach carried out by Burgess et al. [19] where a secant stiffness matrix, instead of a tangent stiffness matrix, is used to trace the equilibrium path of the structure under fire with the following modifications in NIDA [18]:

4.1 The Modified Modulus of Elasticity

In each load cycle during the analysis, the secant stiffness is updated using the modified modulus of elasticity $\overline{E}$ to account for the material strength degradation. Considering a column is stocky enough that the deformation is insensitive to the initial imperfection, at any load level, the applied stress σ can be calculated as

$$\sigma = \frac{F_c}{A} \tag{4}$$

When the applied stress σ is greater than the proportional limit $f_{p,\theta}$ but smaller than the effective yield strength $f_{y,\theta}$, the stress-strain relationship is no longer linear and the equivalent strain can be calculated by rearranging terms from Eq. 1 as

$$\varepsilon = \varepsilon_{y,\theta} - \sqrt{a^2 - \frac{a^2}{b^2}\left(\sigma + c - f_{p,\theta}\right)^2} \tag{5}$$

At the nonlinear range, the tangent modulus can thus be calculated by substituting ε into Eq. 2 while the modified modulus of elasticity $\overline{E}$ for a member under pure compression can be calculated by dividing σ in Eq. 4 by ε in Eq. 5 as

$$\overline{E} = \frac{\sigma}{\varepsilon} \tag{6}$$

Next, considering a beam subject to uniform bending moment, the strains are zero at the neutral axis and vary linearly with distance from the neutral axis. At elevated temperatures when the beam is stressed beyond the proportional limit, the moment M_θ at a given curvature is calculated from the integration of the exact stress calculated from Eq. 1 times the distance from the neutral axis as in Eq. 7 and the moment capacity $M_{c,\theta}$ is taken as the moment where the extreme fiber reaches the effective yield strength.

$$M_\theta = \int_A \sigma y dA \tag{7}$$

Alternatively, since the stress distribution is symmetric about the neutral axis for doubly symmetric sections, the moment in Eq. 7 can be rewritten in terms of strain ε as follows.

$$M_\theta = 2\left(\frac{D/2}{\varepsilon_{\max}}\right)^2\left[\int_0^{\varepsilon_{p,\theta}} t(\varepsilon)\varepsilon^2 \cdot E_{a,\theta} d\varepsilon + \int_{\varepsilon_{p,\theta}}^{\varepsilon_{\max}} t(\varepsilon)\cdot\sigma\cdot\varepsilon d\varepsilon\right] \tag{8}$$

where D is the depth of the section
$t(\varepsilon)$ is the thickness of the web or width of the flange
$\varepsilon_{\max}$ is the maximum strain at the outermost fibre of the section

Therefore, the modified modulus of elasticity $\overline{E}$ will be given by

$$\overline{E} = \frac{M_\theta}{\rho \cdot I} \tag{9}$$

where ρ is the curvature of the beam.

With a similar approach, the modified modulus of elasticity for element under both axial force and moment can be calculated using Eqs. 7 and 9. However, special attention has to be made to the unsymmetrical stress distribution across the section due to the presence of the axial force. The modified modulus of elasticity $\overline{E}$ is incorporated into NIDA [18] to achieve the fire design.

4.2 The PEP Element

When performing second-order analysis using NIDA [18], the PEP (Pointwise Equilibrating Polynomial) element which was well researched by Chan and Zhou [20,21] is used. As shown in Figure 2, the shape function of the lateral displacement v along one principal plane of the element is assumed to be a fifth-order polynomial as follows.

$$v = a_0 + a_1 x + a_2 x^2 + a_3 x^3 + a_4 x^4 + a_5 x^5 \tag{10}$$

The initial imperfection along the member is also included in the PEP element as follows.

$$v_0 = \delta_0\left(1 - \frac{4x^2}{L^2}\right) \tag{11}$$

where $-\frac{L}{2} \le x \le \frac{L}{2}$

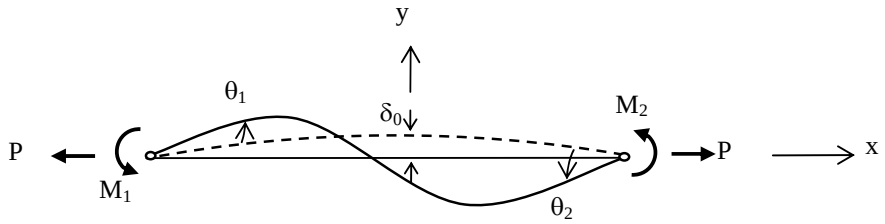

Figure 2. The PEP Element Model

The detailed mathematical derivation of the tangent stiffness matrix and the secant stiffness matrix from the total potential energy function are well documented in references [20] and [21]. In some design codes [2,22], when performing second-order analysis, the inclusion of initial curvature is mandatory. Originally, this PEP element fulfils the requirement because the initial curvature is already included in the shape function. However, it should be noted that for members under fire condition subject to a non-uniform moment distribution, since stress levels along the member are different, the modified modulii of elasticity along the member are therefore different, they should be split into a number of elements small enough that uniform bending moment can be assumed for each element and the initial curvature should be considered carefully by adjusting the coordinates of each node along the member.

4.3 Analysis Procedure

In a conventional second-order elastic analysis under normal condition, since the material is assumed to be perfectly elastic throughout the analysis, only the geometry change is considered. Since the final geometry is unknown during the initial formulations, numerical solution technique must be adopted in which the analysis is carried out in an incremental-iterative manner. In short, the load is applied incrementally and in each load increment, iteration is repeatedly carried out until an equilibrium point is reached. In the next load cycle, the stiffness is calculated based on the updated geometry from the preceding cycle. In the present study, since the nonlinearity of the material under fire is considered, when the stress is beyond the proportional limit, the material properties are to be updated in each load cycle. Among various numerical schemes available in NIDA [18] for carrying out a second-order analysis, the load-control Newton-Raphson method is widely used today for both design and research purposes because of its simplicity. The main feature of this method is the numerical procedure iterates at a constant load level in each cycle; therefore it may result in divergence when the applied load is reaching the limit point. However, in the present study, the Newton-Raphson method is adequate since the failure load occurs before the limit point is reached. Figure 3 schematically shows the incremental-iterative scheme of the conventional Newton-Raphson method. A simple flowchart in Figure 4(a) highlights the key steps of the iteration process. For a conventional second-order elastic analysis under ambient temperature condition where only one plastic hinge is allowed to form, the section capacity check in Eq. 12 is always required to indicate when a member fails. When φ is equal to unity, the applied load is considered as the failure load of the structure and the structural behaviour after the failure load is considered meaningless. Although member by member section capacity check is still required, the member resistance check involving manual calculation of effective length is no longer needed since the second-order moments can be accurately calculated at the instant the analysis is performed.

$$\frac{F_c}{A \cdot p_y} + \frac{\overline{M}_x + F_c\left(\delta_x + \Delta_x\right)}{M_{cx}} + \frac{\overline{M}_y + F_c\left(\delta_y + \Delta_y\right)}{M_{cy}} = \varphi \tag{12}$$

where F_c is the axial compression force

A is the gross section area

p_y is the design strength

M_{ci} is the moment capacity about i-axis

$\overline{M}_i$ is the first-order moment about i-axis

δ_i and Δ_i are the relative and the global displacements about the major axis contributing to the second-order moments

φ is the section capacity factor

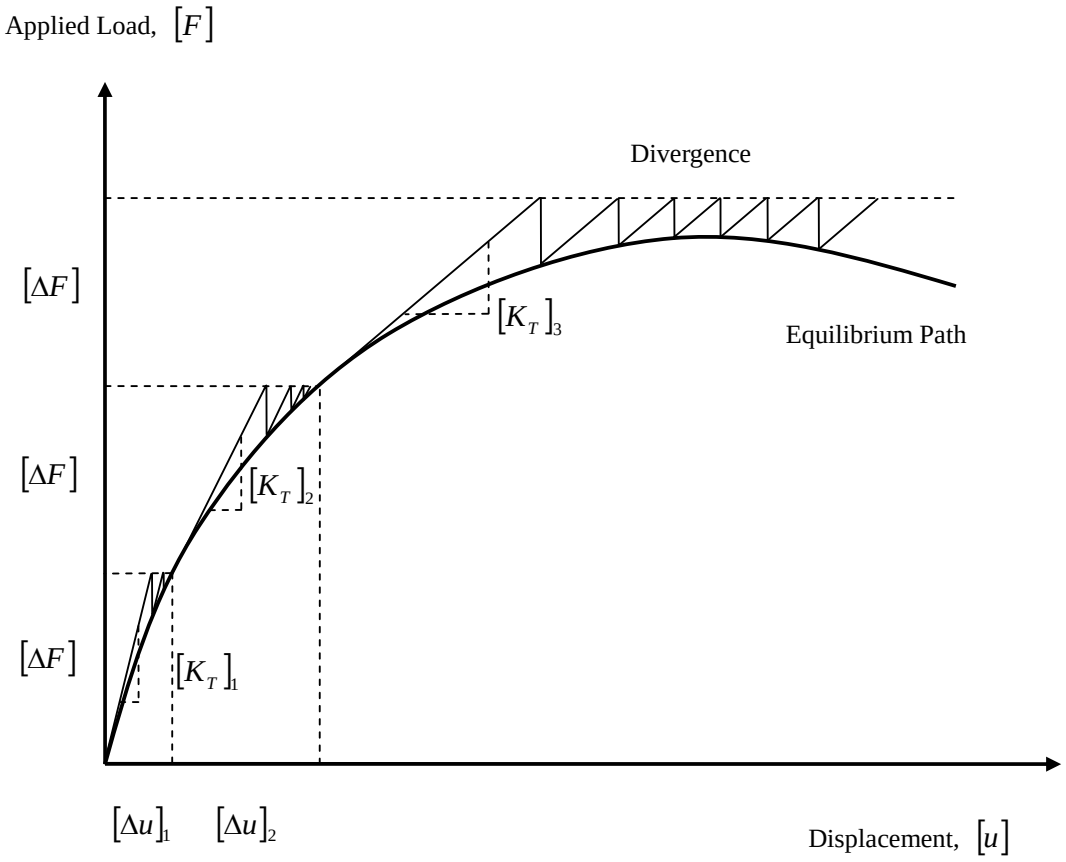

Figure 3. The Newton-Raphson Numerical Procedure

For second-order elastic analysis under fire condition, considering only one principal plane, Eq. 12 can be modified to Eq. 13 as follows to indicate the material across the section starts to behave nonlinearly at elevated temperatures.

$$\frac{F_c}{A \cdot f_{p,\theta}} + \frac{\overline{M}_x + F_c\left(\delta_x + \Delta_x\right)}{f_{p,\theta} \cdot Z_x} = \varphi' \tag{13}$$

where Z_x is the elastic modulus of the section

While ϕ in Eq. 12 greater than 1.0 means failure, φ' in Eq. 13 greater than unity indicates the slope of the stress-strain curve of the material is no longer constant. The modified modulus of elasticity $\overline{E}$ in the secant stiffness has to be updated in each load cycle. To achieve this, firstly, a curvature ρ is assumed by dividing the moment at that load cycle by the flexural rigidity EI from the previous load cycle. Secondly, the strain across the section can be calculated by multiplying the curvature times the distance y from the neutral axis. Thirdly, the stress at distance y can be calculated from Eq. 1 and thus the moment can be found by Eq. 7. At this point, the moment is unbalanced. Therefore, iterations are performed to obtain the value of the modified modulus of elasticity $\overline{E}$ so that the moment calculated from Eq. 7 is equal to the applied moment. Similar to the conventional second-order analysis, failure occurs when the maximum stress reaches the effective yield strength. The flowchart in Figure 4(a) is modified to Figure 4(b) to demonstrate the key steps of the second-order analysis dealing with elevated temperatures.

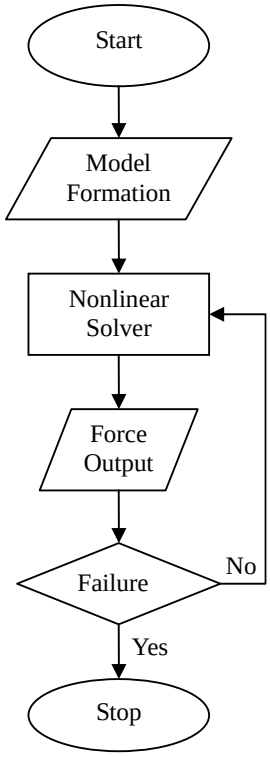

Figure 4(a). Flowchart of Second-order Elastic Analysis at Room Temperature

4.4 Illustrative Examples

The following examples demonstrate the structural performances of members or frames incorporating material nonlinearity at elevated temperatures ranging from 20°C to 600°C. Temperatures above 600°C are not considered since the effective yield strength is already reduced dramatically. The following assumptions are made.

1. Sections are doubly-symmetric.
2. Uniform heat distribution along the member is assumed so no temperature zone is divided along the member.
3. Residual stress is not considered.
4. The self-weight of the material is ignored.
5. The connections are fully protected against fire so that they are unaffected by elevated temperatures.
6. The frames are two-dimensional so out-of-plane buckling is not considered.
7. Planes of cross-section remain plane after deformation.
8. Local buckling failure mode is not considered.

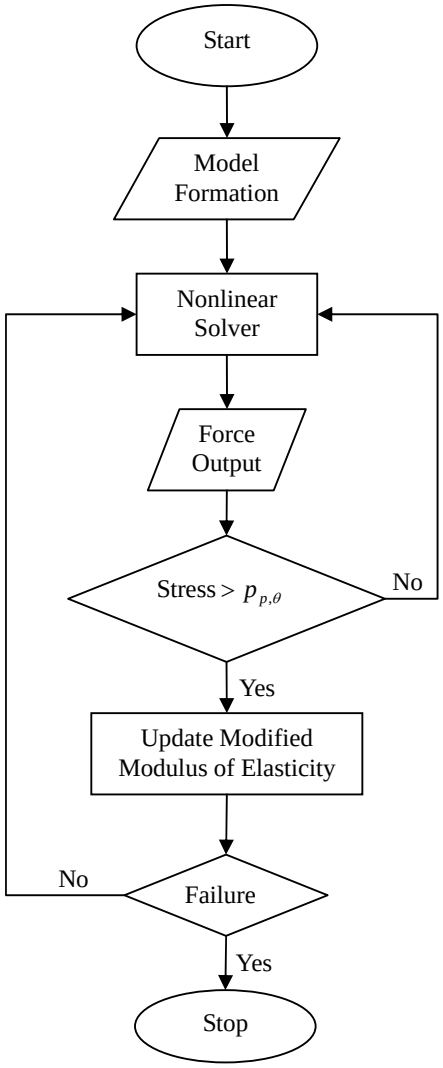

Figure 4(b). Flowchart of Second-order Analysis at Elevated Temperature

4.4.1 Example 1 – A very stocky column

A 1m-long pin-ended column of section 203×203×46 UC ($I_x = 4570cm^4$, $Z_x = 450cm^3$, $A = 58.7cm^2$) in S275 is used as a benchmark example to verify the structural analysis under the effect of elevated temperatures. In this case, since the column is free to expand, thermal stress will not be developed. The column is stocky enough so that it is insensitive to the initial imperfection and the deformation is mainly due to axial shortening. Since the stress along the member is uniform so one PEP element per member is enough to capture the structural behaviour of a stocky column under uniform elevated temperature. The column is compressed at a constant temperature at 20°C, 200°C, 400°C and 600°C respectively. The failure load can be simply taken as the squash load as

$$P_{y,\theta} = A \cdot p_{y,\theta} \tag{14}$$

Before the proportional limit is reached, the equilibrium path can be traced using the conventional numerical approach with the Young's modulus replaced by the slope of linear elastic range $E_{a,\theta}$ given in Table 1. Once the proportional limit is reached, with the modified modulus of elasticity $\overline{E}$

calculated from Eq. 6 updated in the secant stiffness in the load cycle, the load-deflection relationship after the proportional limit can be traced using the modified numerical procedure. Figure 5 presents the load-deflection curves at different temperatures from the results calculated numerically by the modified second-order analysis and theoretically from Eq. 1. The numerical solutions are in line with the theoretical results showing that the modified second-order analysis is able to capture the nonlinear behaviour when the column is under axial force with negligible second-order moment.

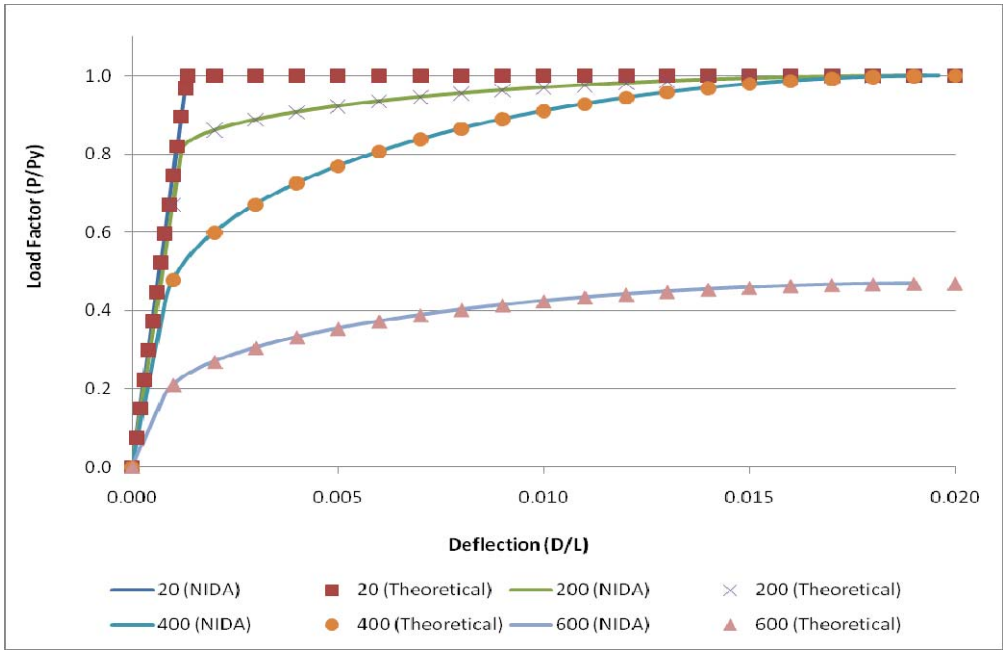

Figure 5. Load-deflection Curve of 203×203×46UC at Elevated Temperatures

4.4.2 Example 2 – A simply supported beam subject uniform moment

A 3m-long simply supported beam of section 203×133×30 UB ($I_x = 2900cm^4$, $Z_x = 280cm^3$, $S_x = 314cm^3$, $A = 38.2cm^2$) in S275 subject to uniform bending moment is used in this example. The beam is assumed to be laterally fully restrained so that the failure mode of lateral-torsional buckling can be ignored. Similar to Example 1, since the bending stress along the member is uniform, one PEP element per member is adequate to capture the structural behaviour of the beam under elevated temperatures. When the bending stress of the outermost fibre reaches proportional limit given in Table 1, the modified modulus of elasticity $\overline{E}$ calculated from Eq. 9 is adopted across the whole section in each load cycle. The moment-curvature relationships at 20°C, 200°C, 400°C and 600°C are plotted in Figure 6. Results suggest that the replacement of the slope of the linear elastic range $E_{a,\theta}$ by the modified modulus of elasticity $\overline{E}$ at elevated temperatures provides a reasonable estimate on the moment-curvature relationship. However, for beam subject to non-uniform moment, it is unwise to use one single value of effective young modulus along the whole member because when the axial strain varies along the member the corresponding tangent modulus also varies. Therefore, more elements should be used so that different values of tangent modulii can be observed along the member and thus the result will be more accurate. Burgess et al. [19] suggested that for practical purposes the optimal number of elements to obtain satisfactory accuracy is between 10 and 20.

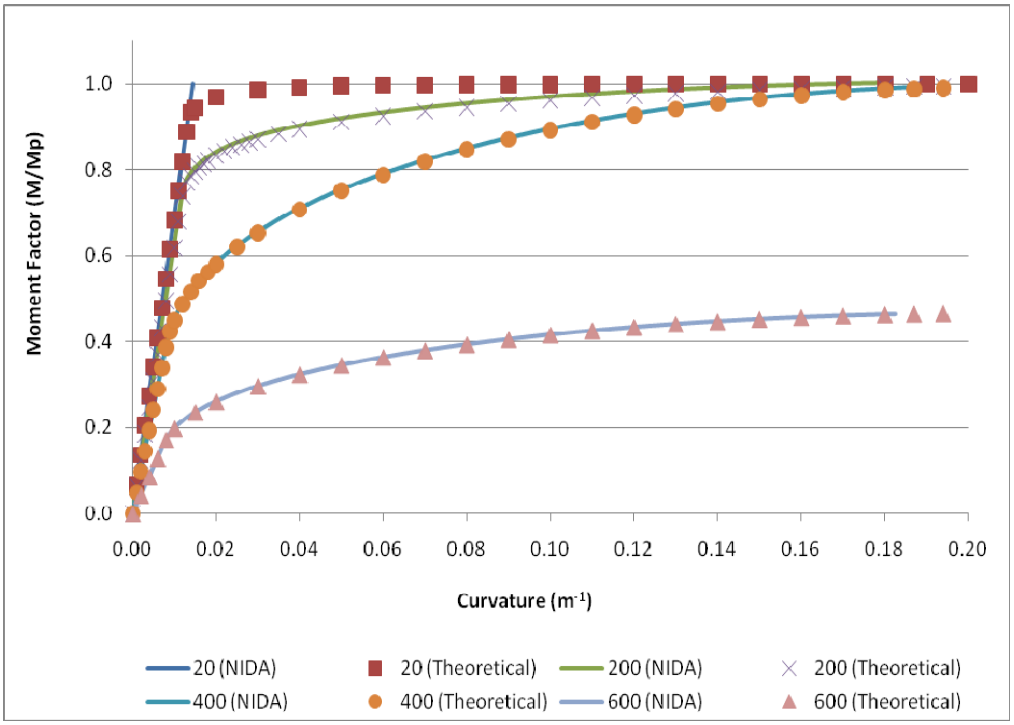

Figure 6. Moment-curvature Relationship of 203×133×30UB at Elevated Temperatures

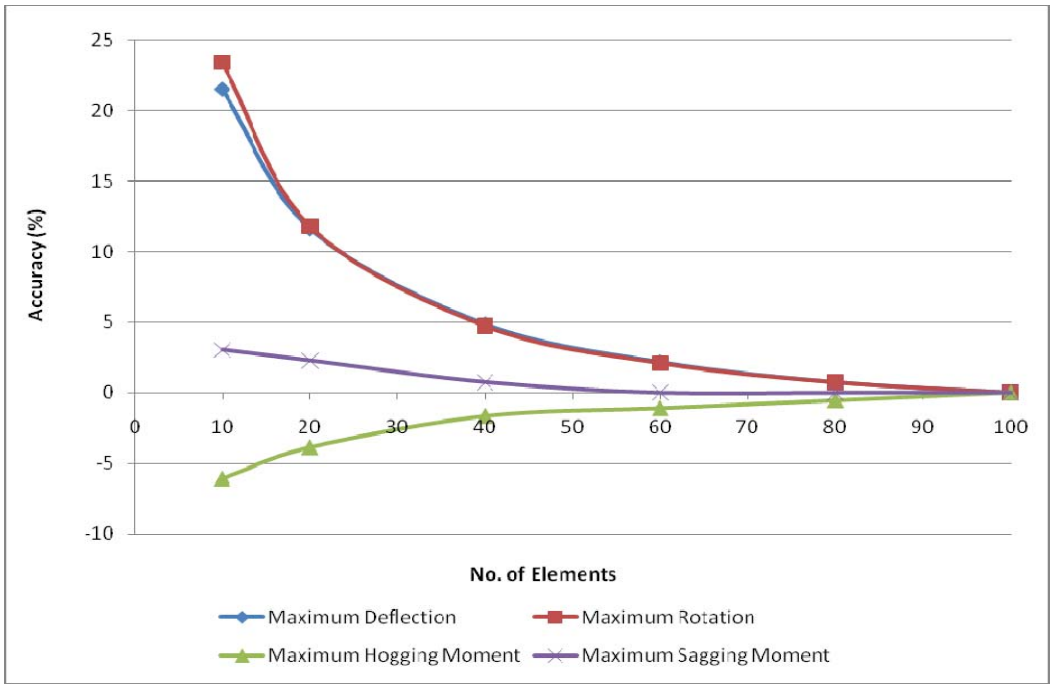

Figure 7. Percentage of Accuracy against No. of Elements of a Propped Cantilever

4.4.3 Example 3 – A propped cantilever with uniformly distributed load

A 5-m propped cantilever under uniformly distributed load of section 457×153×60 UB is used in this example. Unlike the previous example, this member is statically indeterminate so the bending moment diagram and the material properties mutually affect each other. The bending moment is based on the deformation compatibility of the beam; at the mean time, the deformation depends on the flexural rigidity of the beam. Therefore, the accuracy of the fire analysis will largely depends on the number of elements used per member. Figure 7 shows the accuracy against number of elements of the beam at 600°C. As can be seen from the results, when the number of elements is 20, the percentage of accuracy of the maximum hogging and sagging moments fall into a reasonable range of less than 4.0% which is acceptable for practical design purposes.

4.4.4 Example 4 – A non-slender column with axial load

A 3-m 203×203×46UC column is subject to an axial load. In this case, the failure load is influenced by the magnitude of the initial curvature. The presence of the initial curvature will induce a second-order moment. The slenderness ratio falls into a non-slender range about 34.0 so that the column is subject to predominately axial force. To obtain a satisfactory accuracy, the column is split into 20 elements. It should be noted that under normal circumstances when one element per member is used, the initial curvature is already taken care of by the PEP element. However, since in this example the member is split into a number of elements, the magnitude of the initial curvature given in the CoPHK [21] is considered by adjusting the coordinates of the nodes. It should be also noted that according to BS5950-8:1990 [6], when calculating the structural performance in fire, one should consider the strain limit. Depending on the condition of the member, the strain should be limited to 0.5%, 1.5% or 2.0%. In this case the limiting strain of an unprotected column should be taken as 0.5%. However, for research purposes, strain limit of 2.0% is used in this example. Figures 8(a) and 8(b) respectively show the load against vertical deflection at the upper column end and the load against horizontal deflection at the mid-length of the column at elevated temperatures. Unlike the stocky column used in Example 1, the initial curvature is important here to trigger the bending once the load is applied; bending stress is developed across the section and the magnitude of the stress varies along the member as the P-δ moment is zero at the end supports and maximum at the mid-length. Therefore, more elements per member are used to account for the changing material properties along the member under different stress levels.

4.4.5 Example 5 – A multi-storey frame

A three-storey four-bay frame consisting of 203×133×30UB as beams and 203×203×46UC as columns is shown in Figure 9 with the dimensions indicated. Axial forces of $0.5F$ are applied at nodes (11) and (15) and F at nodes (12), (13) and (14) and no force is applied to the beam members. A localized fire starts at column C8 and it is assumed to be contained in the region. Similar to Example 4, C8 is divided into 20 elements to achieve a satisfactory accuracy of modelling of the material nonlinearity while the rest of the structure remains one element per member. Figures 10(a) and 10(b) respectively show the relationship of the applied load against vertical deflection at the top and horizontal deflection at the mid-length of column C8 at 20°C, 200°C, 400°C and 600°C. It is found that the column in Example 5 can sustain a greater applied force than that in Example 4 especially at higher temperatures despite both columns are the same. Figure 11 plots the beam tension over column load at faiure vs temperature. The ratio increases rapidly at higher temperature. It is suggested when the load is applied gradually at elevated temperatures a large displacement occurs which induces tensile membrane action. In other words, the excessive load from the column is redistributed to the members adjoining the column.

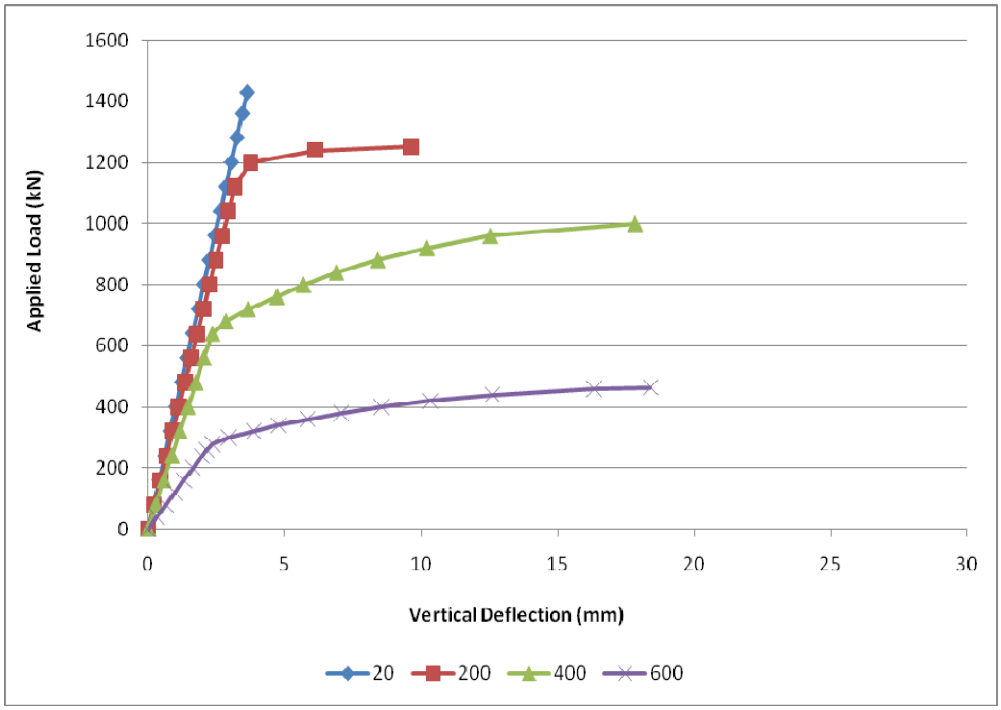

Figure 8(a). Applied Load versus Vertical Deflection of 203×203×46UC at Elevated Temperatures

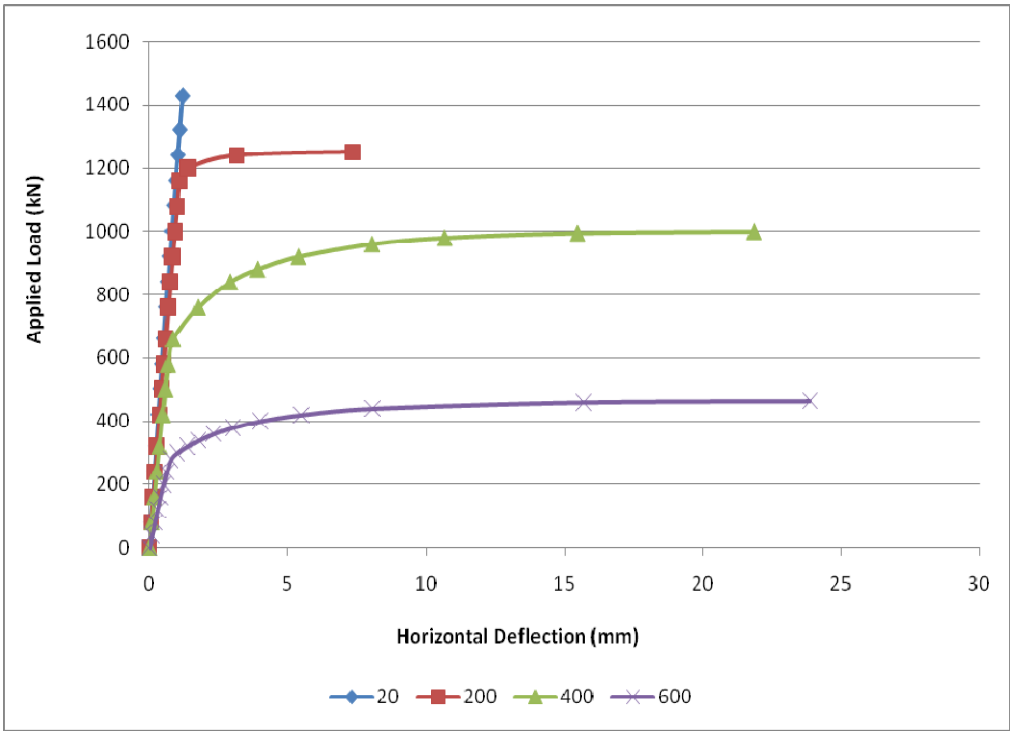

Figure 8(b). Applied Load versus Horizontal Deflection of 203×203×46UC at Elevated Temperatures

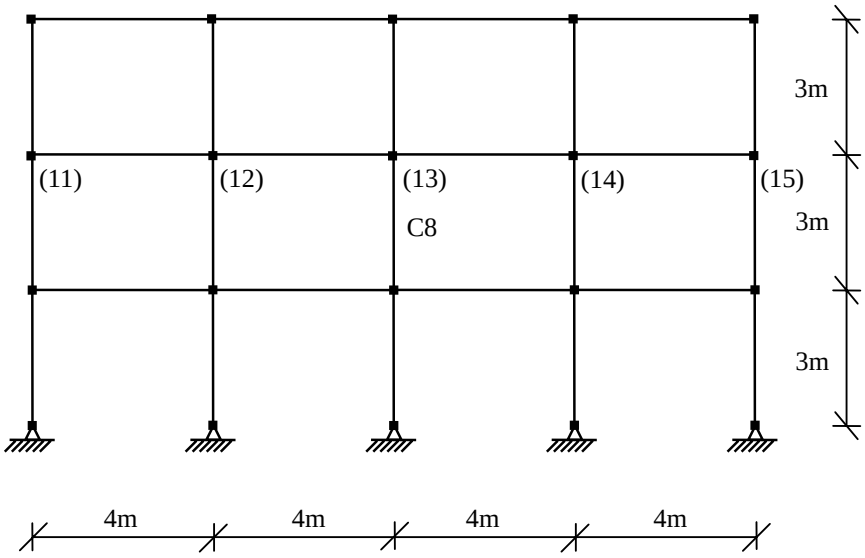

Figure 9. A Three-storey Four-bay Frame

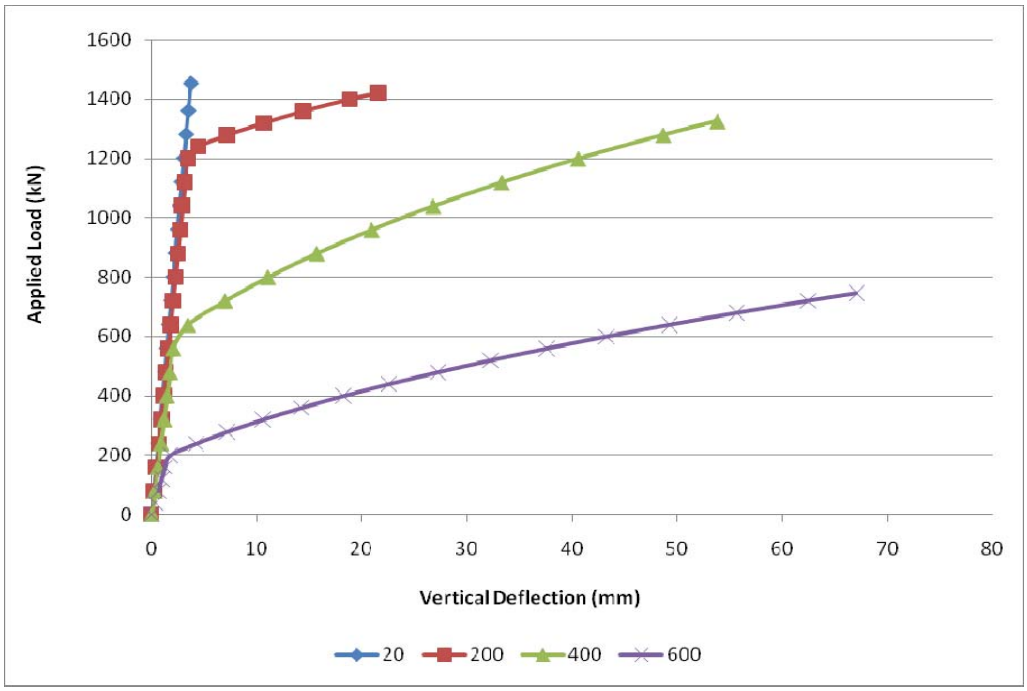

Figure 10(a). Applied Load versus Vertical Deflection of Column “C8” at Elevated Temperatures

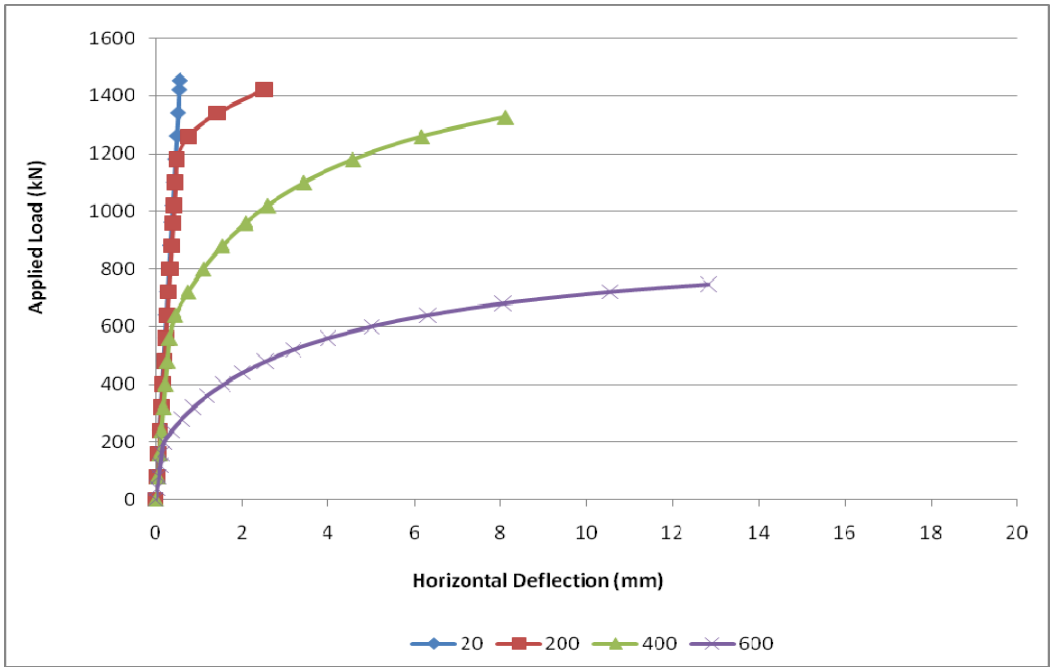

Figure 10(b). Applied Load versus Horizontal Deflection of Column "C8" at Elevated Temperatures

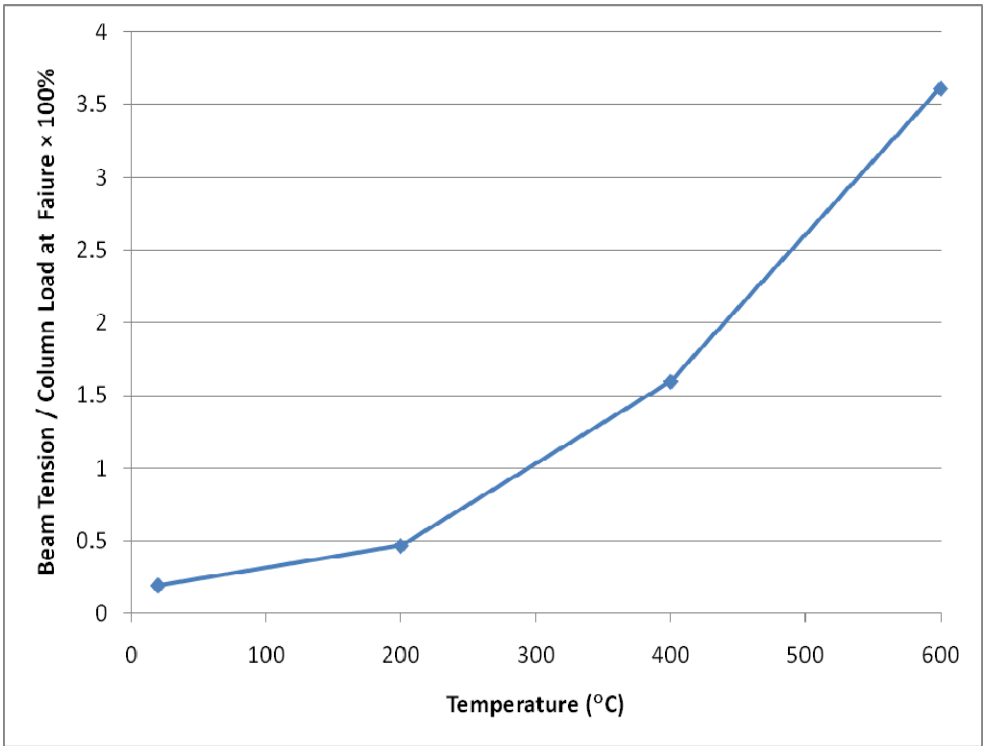

Figure 11. Beam Tension over Column Failure Load vs Temperature

5. COMPARISON AND DISCUSSION

In the study, the analysis is carried out with increasing load under constant temperature. It is found that at higher temperatures a column in a frame is able to take a higher applied force than it is alone because the applied force is actually shared by the connecting members in the form of tensile membrane action. Figure 12 plots the failure load versus temperature of the steel columns in Example 4 and 5. It can be seen that the columns in Example 5 have higher failure loads than those in Example 4 especially at higher temperatures suggesting that the presence of adjoining unheated members greatly increases the failure load of the column. In the mean time, the failure loads are estimated according to Eurocode 3 [1] taking $0.5L$ as the effective length of the steel column are also shown in Figure 12. Comparing the failure loads found by the proposed method using NIDA [18] and Eurocode 3 [1], it can be seen that the proposed method provides a reasonable estimates for column failure loads under fire condition except when the temperature is at 200°C, NIDA [18] slightly overestimates the failure load. The discrepancy between the Eurocode 3 [1] and the NIDA [18] estimates ranges from -1.6% to 6.8%.

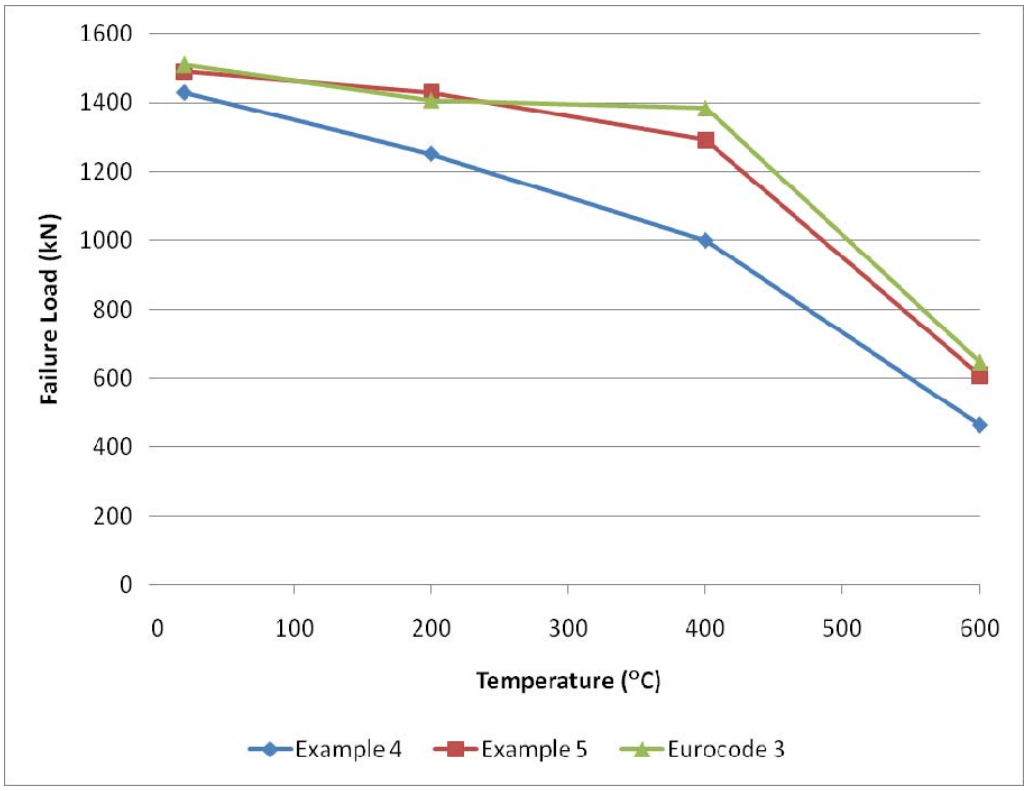

Figure 12. Comparison between NIDA and Eurocode 3 Results

6. CONCLUSIONS AND FUTURE WORKS

Unlike the complicated finite element modelling of steel columns and framed structures at elevated temperatures which has been carried out extensively over the past few decades, this paper aims to develop a simplified approach on fire resistance design using computer program NIDA [18] with the design strength and Young's modulus of the steel replaced by those given in Eurocode 3 Part 1-2 [1]. The aim is to present a modelling approach that can be handled easily by practical engineers using commercially available second-order analysis and design programs. With proper design against fire resistance, a building can be robust that it is insensitive to collapse under localized fire. However, in a realistic fire analysis, the structure under fire condition should be under constant service load with increasing temperature. So, in future study, the analysis should be extended to deal with realistic fire condition by splitting the analysis into two sequences. In the first sequence, the load is applied incrementally at normal condition until the service load is reached; in the second sequence, the load is remained constant while the temperature is increased incrementally and in each temperature increment the thermal response along the member and the mechanical response of the materials in each element are adjusted accordingly. Therefore, the actual tensile membrane action at large deflections can be studied.

REFERENCES

[1] CEN, "Eurocode 3 Design of Steel Structures – Part 1-2: General Rules – Structural Fire Design, BS EN 1993-1-2", British Standards Institution, London, 2005.

[2] CEN, "Eurocode 3 Design of Steel Structures – Part 1-1: General Rules and Rules for Buildings, BS EN 1993-1-1", British Standards Institution, London, 2005.

[3] Franssen, J.M., Talamona, D., Kruppa, J. and Cajot, L.G., "Stability of Steel Columns in Case of Fire: Experimental Evaluation", Journal of Structural Engineering, ASCE, 1998, Vol. 124, No. 2, pp. 158-163.

[4] Yang, K.C., Lee, H.H. and Chan, O., "Performance of Steel H columns Loaded under Uniform Temperature", Journal of Constructional Steel Research, Elsevier, 2006, Vol. 62, No. 3, pp. 262-270.

[5] Yang, K.C. and Hsu, R., "Structural Behavior of Centrally Loaded Steel Columns at Elevated Temperature", Journal of Constructional Steel Research, Elsevier, 2009, Vol. 65, No. 10-11, pp. 2062-2068.

[6] BSI, "Structural Use of Steelwork in Building – Part 8: Part 8: Code of Practice for Fire Resistant Design, BS5950-8", British Standards Institution, London, 2003.

[7] AISC. "Specification for Structural Steel Buildings, ANSI/AISC 360-05", American Institution of Steel Construction, Chicago (IL), 2005.

[8] Janss, J., "Statistical Analysis of Fire Tests on Steel Beams and Columns to Eurocode 3, Part 1.2", Journal of Constructional Steel Research, Elsevier, 1995, Vol. 33, No. 1, pp. 39-50.

[9] Janss, J. and Minne, R., "Buckling of Steel Columns in Fire Conditions", Fire Safety Journal, Elsevier, 1982, Vol. 4, No. 4, pp. 227-235.

[10] Ali, F. and O'Connor, D., "Structural Performance of Rotationally Restrained Steel Columns in Fire", Fire Safety Journal, Elsevier, 2001, Vol. 36, No. 7, pp. 679-691.

[11] Wang, Y.C. and Davies, J.M., "An Experimental Study of Non-sway Loaded and Rotationally Restrained Steel Column Assemblies under Fire Conditions: Analysis of Test Results and Design Calculations", Journal of Constructional Steel Research, Elsevier, 2003, Vol. 59, No. 3, pp. 291-313.

[12] Tan, K.H., Toh, W.S., Huang, Z.F. and Phng, G.H., "Structural Responses of Restrained Steel Columns at Elevated Temperatures. Part 1: Experiments", Engineering Structures, Elsevier, 2007, Vol. 29, No. 8, pp. 1641-1652.

[13] Wald, F., “Simoes da Silva, L., Moore, D.B., Lennon, T., Chladna, M., Santiago, A., Benes, M. and Borges, L., “Experimental Behaviour of a Steel Structure under Natural Fire, Fire Safety Journal, Elsevier, 2006, Vol. 41, No. 7, pp. 509-522.

[14] Wang, Y.C., “An Analysis of the Global Structural Behaviour of the Cardington Steel-framed Building during the Two BRE Fire Tests”, Engineering Structures, Elsevier, 2000, Vol. 22, No. 5, pp. 401-412.

[15] Wang, Y.C., Moore, D.B., “Steel Frames in Fire: Analysis”, Engineering Structures, Elsevier, 1995, Vol. 17, No. 6, pp. 462-472.

[16] Chen, J. and Young, B., “Design of High Strength Steel Columns at Elevated Temperatures”, Journal of Constructional Steel Research, Elsevier, 2008, Vol. 64, No. 6, pp. 689-703.

[17] “ABAQUS Analysis User’s Manual, Version 6.5”, ABAQUS, Inc, 2004.

[18] NIDA, “Non-linear Integrated Design and Analysis User’s Manual, NAF-NIDA series, Version 8”, Department of Civil and Structural Engineering, The Hong Kong Polytechnic University, Hong Kong, 2009. (http://www.nida-naf.com)

[19] Burgess, I.W., El-Rimawi, J.A. and Plank, R.J., “A Secant Stiffness Approach to the Fire Analysis of Steel Beams”, Journal of Constructional Steel Research, Elsevier, 1988, Vol. 11, No. 2, pp 105-120.

[20] Chan, S.L. and Zhou, Z.H., “Pointwise Equilibrating Polynomial Element for Nonlinear Analysis of Frames”, Journal of Structural Engineering, ASCE, 1994, Vol. 120, No. 6, pp. 1703-1717.

[21] Chan, S.L. and Zhou, Z.H., “Second-order Elastic Analysis of Frames Using Single Imperfect Element per Member”, Journal of Structural Engineering, ASCE, 1995, Vol. 121, No. 6, pp. 939-945.

[22] BD, “Code of Practice for Structural Use of Steel 2005”, Buildings Department, Hong Kong SAR Government, 2005.

SEMI-RIGID ELASTO-PLASTIC POST BUCKLING ANALYSIS OF A SPACE FRAME WITH FINITE ROTATION

K.S. Lee[1] and S.E. Han[2,*]

[1] *Research Assistant Professor, Department of Architectural Engineering, Inha University, 253 Yonghyundong, Nam-gu, Incheon, 402-751, South Korea*
[2] *Professor, Department of Architectural Engineering, Inha University, 253 Yonghyundong, Nam-gu, Incheon, 402-751, South Korea*
**(Corresponding author : E-mail: hsang@inha.ac.kr)*

Received:4 December 2010; Revised: 17 January 2011; Accepted: 24 January 2011

ABSTRACT: In this study, large-deformation and small-strain elasto-plastic analysis of space frames with symmetric cross sections and semi-rigid connections are presented. The effect of axial forces on the bending moment and lateral buckling are included. However, axial-torsional and warping effects are omitted. The Eulerian equations for a beam-column with finite rotation taking into account bowing effects are adopted for an elastic system and are extended to an inelastic system with a plastic hinge concept. The derived tangent stiffness matrix is asymmetric due to the finite rotation. The joint connection elements were introduced for semi-rigidity using a static condensation technique. The arc-length method was applied to trace the post-buckling range of elastic and elasto-plastic problems with semi-rigid connections. Nonlinear buckling and elasto-plastic collapse analyses were carried out for the proposed space frame to demonstrate the potential of the developed method in terms of accuracy and efficiency.

Keywords: Space frame, Large deformation, Beam-column, Plastic hinge, Semi-rigid

1. INTRODUCTION

Commonly, steel frames are analyzed and designed assuming ideal rigid joint or pin joint connections, however, testing shows that the connection behavior is semi-rigid. Hence, there may be problems or differences with the conventional design and analysis approach compared to the actual structural behavior. The structural post-buckling response of a semi-rigid space frame in the collapsed regime of deformation is still challenging and is an interesting area for analysis and structural design.

General theoretical formulations and computational algorithms have been developed for planer and space frames. Both a beam-column approach, based on the member's basic force and deformation relationships [1-17], and a finite element approach [18-60] have been used in developing the nonlinear governing equations. The cubic Hermite element is a finite element formulation that uses an energy principle and assumed shape functions for the displacement fields. This simple method for developing a nonlinear formulation for a space frame is widely used [18-29]. The large-deformation geometrically nonlinear analysis is carried out by various methods of treatment of the non-vectorial nature of rotations, the selection of coordinate systems of the stress-strain tensor and the linearization of variational equations. Large rotations are usually represented by Euler's finite theory [30,38] and applied to both beam-column and finite element theory. Agyris et al. [30-34] introduced so-called semi-tangential rotations to circumvent the non-vectorial or non-commutative behavior of successive finite rotations about fixed axes. A total or updated Lagrangian method by degenerated continuum equations is developed [35,36]. Some formulations are derived directly from the weak form of nonlinear rod-type equations by introducing appropriate kinematics [37-46]. The model is often called the 'geometrically exact finite-strain beam theory', and many modern finite element developments of three-dimensional beam theories based their approach on the so-called geometrically exact beam theory [37,38]. An alternative way of deriving efficient non-linear finite element models is the co-rotational approach [47-54]. The main idea of

this approach is to decompose the motion of the element into rigid body and pure deformational parts through the use of a reference system that continuously rotates and translates with the element. The procedure for the co-rotational approach is similar to the Eulerian finite rotation of a beam-column element [3,9-15]. Izzuddin [55] adopted the Eulerian approach for large displacement analysis of thin-walled frames. Most of these finite element nonlinear analysis techniques are based on assumed displacement fields and require a large number of elements to model a structure with large deformation. There are some mixed hybrid elements for the objective of using one element to model each member [56-58] that are based on the complementary energy principle and abandon the assumed displacement shape for an element. There are also stress-based Cauchy formulations [59,60].

The material nonlinearity in a space frame has been described by means of plastic hinge (concentrated or lumped) [4-6,9-11,16-17,21-23,57,58] and plastic zone (distributed or spread of plasticity) [34,46,54,61-66] models. In the plastic hinge approach, the effect of the material yielding is concentrated or lumped into a dimensionless plastic hinge located at the end of the member. There are fewer required elements in this approach, and it eliminates the integration process on the cross-section for each member. The plastic hinge approach requires less computational effort and is less costly than the plastic zone analysis. However, the nonlinear material laws are valid only for limited specific geometries of the cross section. In the case of the plastic zone model, the member needs to be subdivided into several elements along its length and cross-section to model the material nonlinearity. In the literature, the material nonlinearity is often evaluated at a fixed number of cross sections, or moment-curvature-thrust relations [22,61] are derived for each cross-section.

Usually, the joint flexibilities of semi-rigid components are installed by the zero length spring connection element at the end of member [4-6,17,58,67-71]. A procedure of static condensation is used to asses the effect on the element stiffness matrix and equivalent nodal forces. The minimized number of elements in the space frame is required to evaluate the semi-rigidity. Therefore, the one-element-per-member approach is usually used in the semi-rigid analysis of space frame formulation in elastic or elasto-plastic analysis.

Studies that consider nonlinear semi-rigid connection properties in steel frames have been successfully conducted by many researchers. Studies by Chen and coworkers [4-6] are representative work in this area. In his research, he and his coworkers have performed semi-rigid elasto-plastic analysis with the plastic hinge concept for beam-column elements.

Kato et al. [67,68] carried out semi-rigid elasto-plastic analysis of three-dimensional (3D) steel reticulated domes using semi-rigid and elasto-plastic springs located at both ends and at mid-span for each 3D beam-column element in conjunction with an updated Lagrangian formulation.

Recently, Liu et al. [69] and Sekulovic [70] performed the inelastic semi-rigid analysis in static and dynamic case. Chiorean [71] performed the inelastic and large deflection analysis of steel space frames with non-linear flexible joint connections. However, these formulations were based on two-dimensional plane frames or small deformation theory, thereby assuming small member chord rotations and not considering the effect of finite rotation and bowing for large deformations in beam-column element formulations.

In this paper, a method for large deformational post-buckling analysis of semi-rigid elasto-plastic space frames is presented. To develop a space frame element that reflects the rigid body motion and relative deformation are calculated according to the theory of Spiller [12] and Levy and Spiller [15] for Eulerian finite rotation of a 3D space frame. The elastic beam-column formulations of

Kassimali and Abbasnia [8] are also adopted. For the material nonlinearity, the equation for a lumped plastic hinge concept on a beam-column Abbasnia and Kassimali [11] is included. The effects of axial force on the member bending moment (bowing effect) in the elastic and plastic moment capacity are included in the analysis. The asymmetric geometric stiffness matrix, derived by Spiller [12], is used to include some buckling mechanisms of lateral buckling in physical situations. Additionally, the elastic semi-rigid connection spring formulation with the element static condensation procedure developed by Kato et al. [67,68] is adopted to represent the proper semi-rigid joint connection characteristics of beam-column elements. However, the effect of axial force on the member's torsional stiffness (Wagner effect) and warping effect are omitted for simplicity. Finally, nonlinear elastic, plastic beyond limit, or critical point analyses were performed using the arc-length method [72-75]. Analysis of numerical examples for nonlinear elastic and plastic analysis were carried out for the proposed simple and efficient space frame element with a joint connection element to demonstrate accuracy and efficiency.

2. EULERIAN FORMULATION FOR FINITE ROTATION

In the nonlinear analysis of space frames, the assumption that rotations of a body are additive has been widely adopted by researchers in updating the end rotations of frame elements at each incremental step. Such an assumption remains valid only for incremental steps with small rotations. For the cases with finite rotations, it is necessary to consider the non-commutative nature of rotations in three dimensions, such as post-buckling or bifurcation, which makes these space frames more difficult to analyze than trusses or plane frames in nonlinear analysis. In this paper, we used the previous work of Spiller [12] and Levy and Spiller [15] for the Eulerian finite rotation of 3D space frames, which is briefly described as follows.

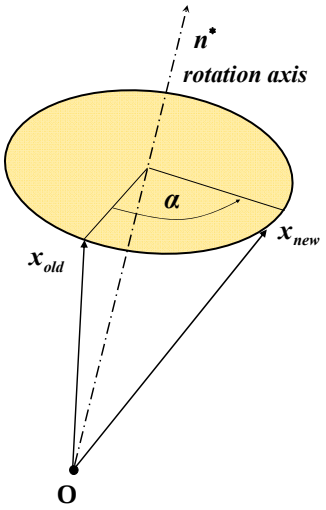

Figure 1. Rotation about an Axis

If an old position $\mathbf{x}_{old}$ of a body is rotated to new position $\mathbf{x}_{new}$, Euler's Theorem of rigid body motions implies that any finite rotation (or sequence of rotations) can be described as a single rotation α about some fixed axis described by a unit vector, $\mathbf{n}^* = \{n_1^*, n_2^*, n_3^*\}$, as shown in Figure 1. The new position vector $\mathbf{x}_{new}$ is described by the old position vector $\mathbf{x}_{old}$, the rotation α and the fixed axis unit vector $\mathbf{n}^*$ as follows:

$$\mathbf{x}_{new} = \mathbf{x}_{old} - (1-\cos\alpha)\{\mathbf{x}_{old} - (\mathbf{x}_{old}\mathbf{n}^*)\mathbf{n}^*\} + \sin\alpha(\mathbf{n}^* \times \mathbf{x}_{old}) \tag{1}$$

We can obtain the following matrix representation of finite rotations:

$$\mathbf{x}_{new} = \widetilde{\mathbf{R}}\mathbf{x}_{old} \tag{2}$$

$$\mathbf{x}_{old} = \mathbf{R}\mathbf{x}_{new} \quad (\mathbf{R}\widetilde{\mathbf{R}} = \mathbf{I}) \tag{3}$$

where $\mathbf{R}$ is the rotation matrix in terms of the α and the components of $\mathbf{n}^*$ as follows:

$$\widetilde{\mathbf{R}} = \begin{bmatrix} \cos\alpha + \mu n_1^2 & -n_3\sin\alpha + \mu n_1 n_2 & n_2\sin\alpha + \mu n_1 n_3 \\ n_3\sin\alpha + \mu n_1 n_2 & \cos\alpha + \mu n_2^2 & -n_1\sin\alpha + \mu n_2 n_3 \\ -n_2\sin\alpha + \mu n_1 n_3 & n_1\sin\alpha + \mu n_2 n_3 & \cos\alpha + \mu n_3^2 \end{bmatrix} \tag{4}$$

with $\mu = 1 - \cos\alpha$.

Based on Euler's finite rotation formula, the rotation matrix is necessary to describe both joint rotations and member rigid body rotations. The matrix can be derived from the so-called Rodriguez rotation vector, a rotation about a fixed axis represented by a unit vector, and a scalar angle of rotation. Thus, a 3D rotation can be represented by a vector-like entity, but such entities cannot be added like vectors. Furthermore, it is assumed that these vector-like entities possess Taylor series expansions whose increments are the small rotation vectors of linear structural analysis [12,15]. To separate the large rigid body deformations of a member from its relative deformations, which are assumed to be small, a Eulerian or local member coordinate system was used, as shown in Figure 2.

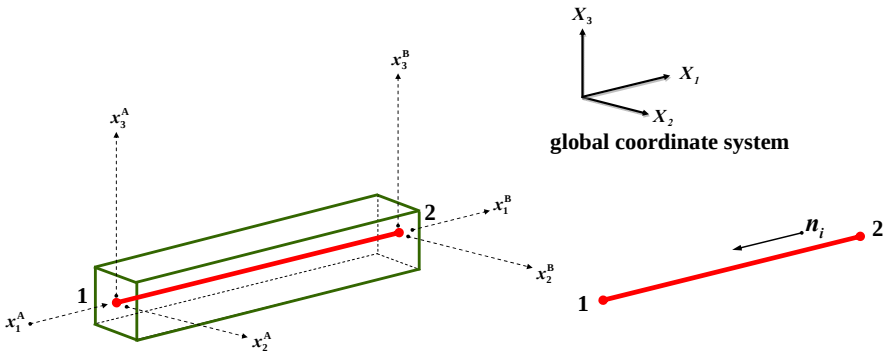

(a) Un-deformed Member

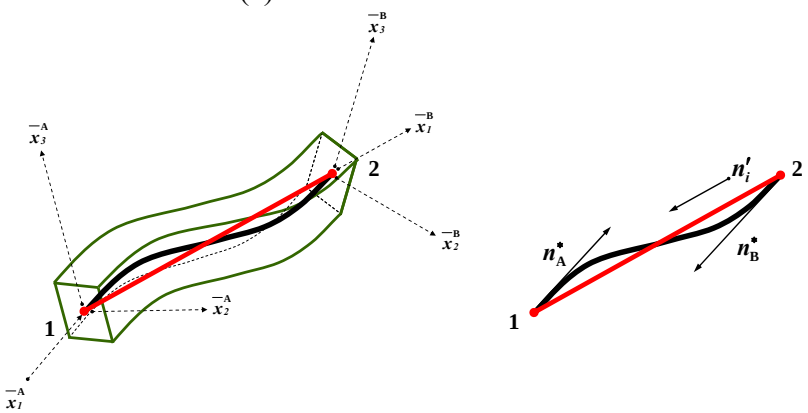

(b) Deformed Member

Figure 2. Relative Member Deformations

In Figure 2, the unit vector of the non-deformed member axis is $\mathbf{n}_i$, and the unit vector of the deformed member axis is $\mathbf{n}_i'$.

Furthermore, the unit vectors of the deformed member axis at joints 1 and 2, $\mathbf{n}_1^*$ and $\mathbf{n}_2^*$, can be represented by Euler's joint rotation matrices, $\mathbf{R}_1$ and $\widetilde{\mathbf{R}}_2$. The unit vector of the non-deformed member axis, $\mathbf{n}_i$, can be represented as follows.

$$\mathbf{n}_1^* = \widetilde{\mathbf{R}}_1 \mathbf{n}_i \tag{5}$$

$$\mathbf{n}_2^* = \widetilde{\mathbf{R}}_2 \mathbf{n}_i \tag{6}$$

The rotation vector at joint 2, θ_2, can be represented by the cross product of the member unit vector, $\mathbf{n}_i$, and the deformed member unit vector, $\mathbf{n}_2^*$, at joint 2 with properties as follows:

$$\theta_2 \cong \mathbf{n}_i \times \mathbf{n}_2^* \tag{7}$$

$$\left|\theta_2\right| = \cos^{-1}\left(\mathbf{n}_i \mathbf{n}_2^*\right) \tag{8}$$

The end of member rotation vector for joint 1, θ_1, is represented as follows:

$$\theta_1 = \theta_2 + \theta_{12} \tag{9}$$

where θ_{12} is the rotation of joint 1 with respect to joint 2. This equation simply describes the vector form of the matrix product, $\mathbf{R}\widetilde{\mathbf{R}}_2$.

From this simple and exact formulation of Euler's finite rotation [12,15], we can calculate the exact member end rotations, θ_1, θ_2 which is separated the rigid body rotations. In the case of geometrically nonlinear large displacement analysis of space frame, the exact member rotational deformation is relatively small, because of its large rigid body rotation occurrence. The formulation of this study is valid for the elastic, elasto-plastic large deformation analysis of space frame element with beam-column equations. The accuracy and efficiency are demonstrated in verification examples lately.

3. ELASTIC SPACE FRAME ELEMENT

To analyze the plastic collapsing and post-buckling of the space frame, one should include the formulation of a large deformational effect. In this study, the beam-column element with a bowing effect [3,8,9] was used as the basic element equation, and then those 2D beam-column element equations were expanded to incorporate the element tangent stiffness matrix. The direct 3D beam-column elements that account the lateral-torsional effect are described in the literature [13-15]; however, these formulations are too complex for the elasto-plastic post-buckling analysis of a semi-rigid space frame. Therefore, in this study, the well-known two-dimensional (2D) beam-column equations are adopted for numerical efficiency. The coupling effect of the member axial-torsional and warping effects are omitted.

3.1 Beam-column Equation

The member force of the space frame element shown in Figure 3 can be written by the 2D beam-column equations [3,8,9], which include the effect of member displacement upon the bending moment to the end. As a result, the member stiffness becomes a function of the axial load.

$$M_{1j} = \frac{EI_j}{L}\left(c_{1j}\theta_{1j} + c_{2j}\theta_{2j}\right) \quad (j = 2,3) \tag{10}$$

$$M_{2j} = \frac{EI_j}{L}\left(c_{2j}\theta_{1j} + c_{1j}\theta_{2j}\right) \quad (j = 2,3) \tag{11}$$

$$M_t = \frac{GJ}{L}\varphi_t \tag{12}$$

$$Q = EA\left(\frac{u}{L} - \sum_{j=2}^{3} c_{bj}\right) \tag{13}$$

$$c_{bj} = b_{1j}\left(\theta_{1j} + \theta_{2j}\right)^2 + b_{2j}\left(\theta_{1j} - \theta_{2j}\right)^2 \tag{14}$$

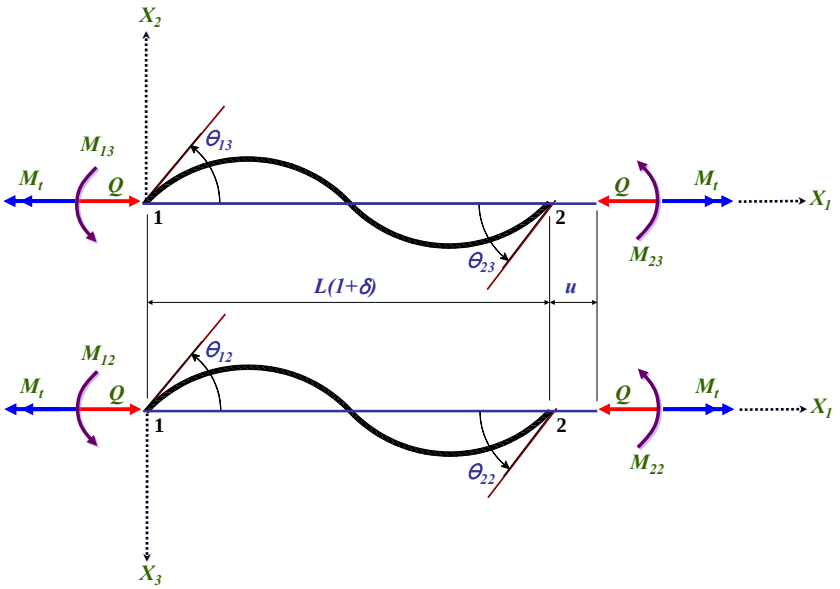

Figure 3. Relative Member Deformations and Corresponding Forces

As is shown in Figure 3, θ_{1j} and θ_{2j} are the relative member end rotations calculated by Eqs. 7 and 9, where φ_t is linear axial twist, u is axial displacement, A is the area of cross section, E is the modulus of elasticity, I_j is the moment of inertia about the X_j-axis, GJ is the torsional rigidity, c_{1j} and c_{2j} are the stability functions for bending about the X_j-axis, c_{bj} is the length correction factor caused by flexural deformation (bowing) about the X_j-axis, and b_{1j} and b_{2j} are the bowing functions of the axial force parameter q, defined in Eq. 15.

$$q = \frac{Q}{Q_{Euler}} = Q\frac{L^2}{\pi^2 EI_j} \tag{15}$$

The expression for the member axial force, Q in Eq. 13 contains bowing functions b_{1j} and b_{2j}, which are functions of the axial force parameter, q. Therefore, Eq. 13 is a nonlinear function. A computational difficulty arises in determining Q from the axial displacement, u. An iterative

procedure must be employed to compute the axial force of a member and can be solved using the following process.

Noting that q is the only unknown quantity in Eq. 13, let a new function, $K(q)$, be defined as follows:

$$K(q) = \frac{\pi^2}{\lambda^2} q + \sum_{j=2}^{3} c_{bj} - \frac{u}{L} = 0 \tag{16}$$

A new value of q_{i+1} is obtained from the first order Taylor series expansion,

$$q_{i+1} = q_i + \Delta q_i = q_i - \frac{K(q_i)}{K'(q_i)} \tag{17}$$

where $K'(q)$ is the derivative of $K(q)$ with respect to the axial force parameter, q, and represented as follows:

$$K'(q) = \frac{dK(q)}{dq} = \frac{\pi^2}{\lambda^2} + \sum_{n=2,3}^{3} \frac{1}{\varepsilon_j} \left\{ b'_{1j} \left(\theta_{1j} + \theta_{2j}\right)^2 + b'_{2j} \left(\theta_{1j} - \theta_{2j}\right)^2 \right\} \tag{18}$$

where $\lambda = L / \sqrt{I / A}$ and $\varepsilon_j = I_j / I$, in which I is an arbitrary reference moment of inertia and b'_{ij} is a differentiation of the bowing function with respect to q. An approximate solution to this equation for q_i is initially assumed, and the iteration is performed until $|\Delta q_i|$ is sufficiently small. After determining the axial force Q by the iterative process, member end moments were computed from Eqs. 10-12. A detailed description of Eqs. 10-18 and the corresponding variables are explained in references [3,8,9].

3.2 Approximate Beam-Column Equation

Computational difficulties are occasionally encountered in post-buckling analysis when the closed form of the stability and bowing functions and their derivatives become singular at $q = 0$. The explicit expressions for the stability function, c_{1j} and c_{2j}, and the bowing function, b_{1j} and b_{2j}, in terms of the axial force parameter q can be written as a series expression [9]. By using the following series expressions, these difficulties can be avoided. However, these equations are only theoretically valid for low absolute values of axial force.

$$c_{1j} \cong 4 - \frac{4}{15}\pi^2 q - \frac{11}{6300}\pi^4 q^2 - \frac{1}{27000}\pi^6 q^3 \tag{19}$$

$$c_{2j} \cong 2 + \frac{1}{30}\pi^2 q + \frac{13}{12600}\pi^4 q^2 + \frac{11}{378000}\pi^6 q^3 \tag{20}$$

$$b_{1j} \cong \frac{1}{40} + \frac{1}{2800}\pi^2 q + \frac{1}{168000}\pi^4 q^2 + \frac{11}{388080000}\pi^6 q^3 \tag{21}$$

$$b_{2j} \cong \frac{1}{24} + \frac{1}{720}\pi^2 q + \frac{1}{20160}\pi^4 q^2 + \frac{11}{604800}\pi^6 q^3 \tag{22}$$

The approximate beam-column equation can be obtained by substituting Eqs. 19-22 for the member force equations Eqs. 10-13.

By substituting Eq. 19 and 20, the member force equation of the approximate beam-column equation can be obtained as follows:

$$M_{1j} = \left(\frac{4EI_j}{L} + \frac{2QL}{15} \right) \theta_{1j} + \left(\frac{2EI_j}{L} - \frac{QL}{30} \right) \theta_{2j} \quad (j = 2,3) \tag{23}$$

$$M_{1j} = \left(\frac{2EI_j}{L} - \frac{QL}{30} \right) \theta_{1j} + \left(\frac{4EI_j}{L} + \frac{2QL}{15} \right) \theta_{2j} \quad (j = 2,3) \tag{24}$$

$$M_t = \frac{GJ}{L} \varphi_t \tag{25}$$

$$Q = EA \left\{ \frac{u}{L} + \frac{1}{30} \left(2\theta_{12}^2 - \theta_{12}\theta_{22} + 2\theta_{22}^2 \right) + \frac{1}{30} \left(2\theta_{13}^2 - \theta_{13}\theta_{13} + 2\theta_{13}^2 \right) \right\} \tag{26}$$

Teh [52] called the finite element formulated beam element that used the approximate beam-column equation as co-rotational cubic element. And these formulations were used in some references [47,48]. Though, this expression is an approximated expression of the closed form of Eqs. 10-13, it has shown satisfying results compared to a beam-column element with one element per member [47] or two elements per member [48] with a symmetric tangent stiffness matrix and joint rotation matrix. Lately, several formulations have been proposed in the literature [52,76-79] to improve the shortcomings of the cubic element and the conventional stability-based beam-column element. The improved formulation of co-rotational cubic elements by Teh and Clarke [52] used the asymmetric tangent stiffness matrix and shows more accurate results. Liew et al. [79] used the symmetric portion of the induced moment matrix alone, which is referred to as the joint moment matrix and needs to be assembled to form the structure tangent stiffness matrix.

3.3 Tangent Stiffness Matrix for Large Deformation

In this study, the beam-column approach in section 3.1 is applied to elastic and elasto-plastic post-buckling problems, and the so-called approximate beam-column element in section 3.2, which is similar to the formulation of the co-rotational form of cubic element, is applied to the analysis of elastic problems alone. The non-commutative nature of finite rotation in section 2 yields an asymmetric tangent stiffness matrix in both cases.

The member force-deformation relationships of Eqs. 10-13 may be rewritten as follows:

$$\mathbf{S}^T = \left\{ Q, M_t, M_{12}, M_{13}, M_{22}, M_{23} \right\} \tag{27}$$

$$\bar{\mathbf{u}}^T = \left\{ u, \varphi_t, \theta_{12}, \theta_{13}, \theta_{22}, \theta_{23} \right\} \tag{28}$$

And the incremental form of the member equation is written as follows:

$$\Delta \bar{\mathbf{s}} = \mathbf{t} \Delta \bar{\mathbf{u}} \tag{29}$$

Where t is the element stiffness matrix according to the incremental member displacement $\Delta \bar{\mathbf{u}}$ in the local coordinates, as shown previously in Eqs. 10-13 and 23-26. By using the incidence matrix $\bar{\mathbf{B}}$, the element nodal force and nodal displacement can be written as follows:

$$\bar{\mathbf{d}} = \bar{\mathbf{B}}\bar{\mathbf{u}} \tag{30}$$

$$\bar{\mathbf{f}} = \bar{\mathbf{B}}\bar{\mathbf{s}} \tag{31}$$

Conventionally, the element nodal force in global coordinates $\mathbf{F}$ can be written from the rotation matrix $\mathbf{R}$:

$$\mathbf{F} = \mathbf{R}\bar{\mathbf{f}} = \mathbf{R}\bar{\mathbf{B}}\bar{\mathbf{s}} \tag{32}$$

Eq. 32 could be interpreted as a member equilibrium equation in a global coordinate system. The tangent stiffness matrix of the beam-column can be obtained from the differential form with respect to the incremental displacement [12,15]:

$$\begin{aligned}\Delta\mathbf{F} &= \Delta\left(\mathbf{R}\bar{\mathbf{B}}\bar{\mathbf{s}}\right) = \mathbf{R}\bar{\mathbf{B}}\left(\Delta\bar{\mathbf{s}}\right) + \mathbf{R}\left(\Delta\bar{\mathbf{B}}\right)\bar{\mathbf{s}} + \left(\Delta\mathbf{R}\right)\bar{\mathbf{B}}\bar{\mathbf{s}} \\ &= \left(\mathbf{K}_E + \mathbf{K}_G^S + \mathbf{K}_G^R\right)\delta\mathbf{d}\end{aligned} \tag{33}$$

The first term in Eq. 33 becomes the elastic stiffness matrix. The second and third terms become the geometric stiffness matrix. $\mathbf{K}_G^S$ and $\mathbf{K}_G^R$ indicate the stretching and rotational terms of the geometric stiffness. The rotational geometric stiffness matrix, $\mathbf{K}_G^R$, is asymmetric [12,15] due to the non-commutative nature of finite rotation, and this geometric stiffness matrix is responsible for the lateral-torsional buckling and the buckling mode shape at the critical point (limit or bifurcation). However, the geometric stiffness matrix does little to affect the material nonlinear problems.

4. INELASTIC EFFECT

The plastic hinge concept was applied to account for the material nonlinearity. The material was assumed to be ideally elasto-plastic without strain-hardening or unloading effects. The yielding is concentrated at the member's ends in the forms of plastic hinges.

The members were assumed to remain elastic between plastic hinges with the large deformation formulation as mentioned in the previous section, and the yielding criterion [11] of the plastic hinge assumed to be as follows:

$$g_n = \left[\left(\frac{\overline{M}_t}{M_{p1}}\right)^2 + \sum_{j=2}^{3}\left(\frac{\overline{M}_{ij}}{M_{pj}}\right)^2\right]^{0.5} + \left(\frac{\overline{Q}}{Q_y}\right)^2 = 1 \quad \left(i = 1,2 \quad j = 2,3\right) \tag{34}$$

where Q_y, M_{p1} and M_{pj} are the axial yielding force, the plastic torsional moment capacity in the absence of axial force and bending moments, and the uniaxial plastic moment capacity for bending about the X_j-axis, respectively. $\overline{Q}$, $\overline{M}_t$ and $\overline{M}_{ij}$ are the axial force, torsional moment and moment at end *i* about the X_j-axis when the plastic hinge forms, respectively.

When plastic hinges are present, the member end rotations at the released ends are obtained from the relative member force-deformation relationships instead of the orientation matrices of the adjacent joints [11]. In each of the foregoing cases, the relative twisting of the member ends is given as follows:

$$\varphi_t = \frac{L\overline{M}_t}{GJ} \tag{35}$$

Eq. 35 performs an important role in plastic analysis when the torsional moment governs the structural behavior, such as in Example 6.4, a horizontal bent frame.

A more comprehensive explanation and numerical results are discussed below. As explained above, the axial force and bending moment are coupled when beam-column equations are employed, and the member end release effect may occur and influence the member equilibrium when the plastic hinges occur. Therefore, the iterative procedures of Eqs. 16-17 are required with the modification of Eq. 18, which accounts for the release end effect by the following equation:

$$K'(q) = \frac{\pi^2}{\lambda^2} + \sum_{j=2}^{3} c'_{bj} \tag{36}$$

$$\begin{aligned} c'_{bj} &= b'_{1j}\left(\theta_{1j} + \theta_{2j}\right)^2 + b'_{2j}\left(\theta_{1j} - \theta_{2j}\right)^2 + 2b_{1j}\left(\theta_{1j} + \theta_{2j}\right)\left(\theta'_{1j} + \theta'_{2j}\right) \\ &+ 2b_{1j}\left(\theta_{1j} - \theta_{2j}\right)\left(\theta'_{1j} - \theta'_{2j}\right) \quad (j = 2,3) \end{aligned} \tag{37}$$

5. SEMI-RIGID CONNECTION ELEMENT

To consider the semi-rigid connection characteristics of member ends, the elastic connection spring formulation of Kato [67] was adopted as shown in Figure 4. The overall stiffness matrix of the compound element can be computed with the static condensation technique.

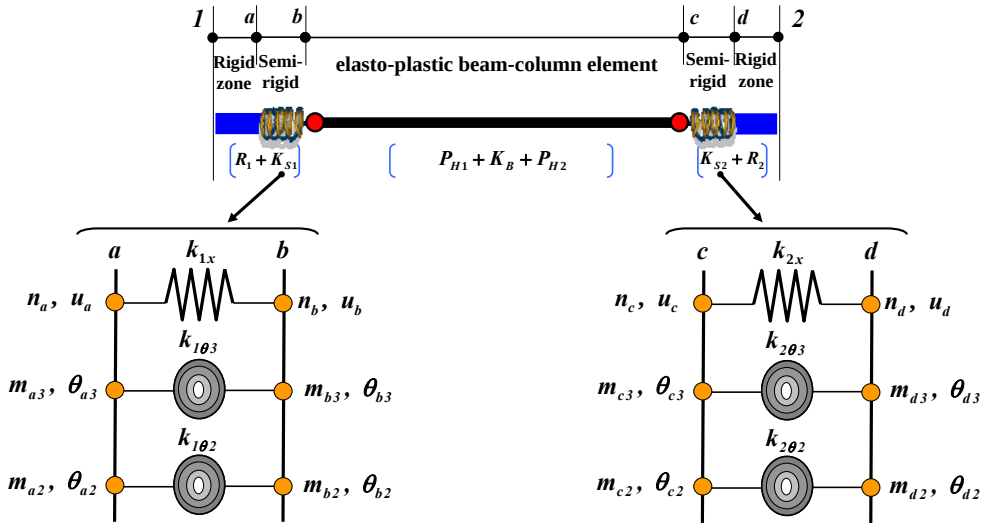

Figure 4. Semi-rigid Connection Spring Element

The member is modeled to be composed of the elements in the order as follows: (1) a rigid panel element of (1-a); (2) an elastic spring (K_{s1}) to represent the left end semi-rigid joint connection(a-b); (3) an elastic beam-column element (K_B) between nodes b and c to include the large deformation behavior of the member with plastic hinges (P_{H1} , P_{H2}) (b-c); (4) an elastic spring (K_{s2}) to represent the left end semi-rigid joint connection (c-d); and (5) a rigid panel element (d-2).

Equilibrium equations for elastic springs, denoted by a-b and c-d at both ends of each member, can be given by specific kinematics for outer and inner nodes. At the left connection a-b with K_{s1}, for example, the relationship of force-deformation can be written as follows:

$$n_b = -n_a = k_{1x}(u_b - u_a) \tag{38-a}$$

$$m_{b2} = -m_{a2} = k_{1\theta 2}(\theta_{b2} - \theta_{a2}) \tag{38-b}$$

$$m_{b3} = -m_{a3} = k_{1\theta 3}(\theta_{b3} - \theta_{a3}) \tag{38-c}$$

Where u_a, θ_{a2}, θ_{a3} and u_b, θ_{b2}, θ_{b3} are the axial displacements and the rotations about the X_j-axes, respectively. The elastic constants, k_{1x}, $k_{1\theta 2}$ and $k_{1\theta 3}$, are the axial rigidity and the bending rigidities of the spring, $\mathbf{K}_{s1}$. Thus, the matrix form of Eq. 38 is as follows:

$$\begin{Bmatrix} n \\ m_2 \\ m_3 \end{Bmatrix} = \mathbf{K}_{s1} \begin{Bmatrix} u \\ \theta_2 \\ \theta_3 \end{Bmatrix} = \begin{bmatrix} k_{1x} & 0 & 0 \\ 0 & k_{1\theta 2} & 0 \\ 0 & 0 & k_{1\theta 2} \end{bmatrix} \begin{Bmatrix} u_b - u_a \\ \theta_{b2} - \theta_{a2} \\ \theta_{b3} - \theta_{a3} \end{Bmatrix} \tag{39}$$

Usually, the elastic constants, k_{1x}, $k_{1\theta 2}$ and $k_{1\theta 3}$ of the spring $\mathbf{K}_{s1}$ would be determined by experimentation or with a previously proposed model [5].

The extended form of Eq. 39 for 12-dof of the spring end node a-b can be written as follows:

$$\mathbf{F}_{ab} = \mathbf{K}_{s1}\mathbf{d}_{ab} \tag{40}$$

Where the force and displacement vectors $\mathbf{F}_{ab}$, $\mathbf{d}_{ab}$ and spring stiffness matrix $\mathbf{K}_{s1}$ are written as follows:

$$\mathbf{F}_{ab} = \{n_{a1}, q_{a2}, q_{a3}, m_{a1}, m_{a2}, m_{a3}, n_{b1}, q_{b2}, q_{b3}, m_{b1}, m_{b2}, m_{b3}\}^T \tag{41}$$

$$\mathbf{d}_{ab} = \{u_a, v_a, w_a, \theta_{a1}, \theta_{a2}, \theta_{a3}, u_b, v_b, w_b, \theta_{b1}, \theta_{b2}, \theta_{b3}\}^T \tag{42}$$

$$\mathbf{K}_{s1} = \begin{bmatrix} \mathbf{K}^*_{s1} & -\mathbf{K}^*_{s1} \\ -\mathbf{K}^*_{s1} & \mathbf{K}^*_{s1} \end{bmatrix}, \quad \mathbf{K}^*_{s1} = \begin{bmatrix} k_{s1} & 0 & 0 & 0 & 0 & 0 \\ 0 & 0 & 0 & 0 & 0 & 0 \\ 0 & 0 & 0 & 0 & 0 & 0 \\ 0 & 0 & 0 & 0 & 0 & 0 \\ 0 & 0 & 0 & 0 & k_{1\theta 2} & 0 \\ 0 & 0 & 0 & 0 & 0 & k_{1\theta 3} \end{bmatrix} \tag{43}$$

The stiffness matrix of member end node 1, 2 is represented from the rigid zone-spring displacement relationship matrix b_1 and b_2 for each end node 1 and 2, respectively:

$$\mathbf{K}_1 = \mathbf{b}_1^T \mathbf{K}_{s1} \mathbf{b}_1, \quad \mathbf{K}_2 = \mathbf{b}_s^T \mathbf{K}_{ss} \mathbf{b}_s \tag{44}$$

Where b_1 and b_2 can be written as follows:

$$\mathbf{b}_1 = \begin{bmatrix} b_{11} & 0 \\ 0 & b_{1b} \end{bmatrix}, \quad \mathbf{b}_{11} = \begin{bmatrix} 1 & 0 & 0 & 0 & 0 & 0 \\ 0 & 1 & 0 & 0 & 0 & L_1 \\ 0 & 0 & 1 & 0 & -L_1 & 0 \\ 0 & 0 & 0 & 1 & 0 & 0 \\ 0 & 0 & 0 & 0 & 1 & 0 \\ 0 & 0 & 0 & 0 & 0 & 1 \end{bmatrix}, \quad \mathbf{b}_{1b} = \begin{bmatrix} 1 & 0 & 0 & 0 & 0 & 0 \\ 0 & 1 & 0 & 0 & 0 & 0 \\ 0 & 0 & 1 & 0 & 0 & 0 \\ 0 & 0 & 0 & 1 & 0 & 0 \\ 0 & 0 & 0 & 0 & 1 & 0 \\ 0 & 0 & 0 & 0 & 0 & 1 \end{bmatrix} \tag{45}$$

$$\mathbf{b}_2 = \begin{bmatrix} \mathbf{b}_{2d} & 0 \\ 0 & \mathbf{b}_{22} \end{bmatrix}, \quad \mathbf{b}_{2d} = \begin{bmatrix} 1 & 0 & 0 & 0 & 0 & 0 \\ 0 & 1 & 0 & 0 & 0 & 0 \\ 0 & 0 & 1 & 0 & 0 & 0 \\ 0 & 0 & 0 & 1 & 0 & 0 \\ 0 & 0 & 0 & 0 & 1 & 0 \\ 0 & 0 & 0 & 0 & 0 & 1 \end{bmatrix}, \quad \mathbf{b}_{22} = \begin{bmatrix} 1 & 0 & 0 & 0 & 0 & 0 \\ 0 & 1 & 0 & 0 & 0 & L_2 \\ 0 & 0 & 1 & 0 & -L_2 & 0 \\ 0 & 0 & 0 & 1 & 0 & 0 \\ 0 & 0 & 0 & 0 & 1 & 0 \\ 0 & 0 & 0 & 0 & 0 & 1 \end{bmatrix} \tag{46}$$

The incremental equilibrium equation of a composed member can be written (as follows) for each semi-rigid spring and beam-column element:

$$\begin{bmatrix} \mathbf{K}_1 & 0 & 0 \\ 0 & \mathbf{K}_b & 0 \\ 0 & 0 & \mathbf{K}_2 \end{bmatrix} \begin{Bmatrix} \delta\mathbf{d}_1 \\ \delta\mathbf{d}_b \\ \delta\mathbf{d}_c \\ \delta\mathbf{d}_2 \end{Bmatrix} + \begin{Bmatrix} \mathbf{g}_1 \\ \mathbf{g}_b + \mathbf{F}_{b,beam} \\ \mathbf{F}_{c,beam} + \mathbf{g}_c \\ \mathbf{g}_2 \end{Bmatrix} - \begin{Bmatrix} \mathbf{P}_1 \\ 0 \\ 0 \\ \mathbf{P}_2 \end{Bmatrix} = 0 \tag{47}$$

where the tangent stiffness matrix $\mathbf{K}_b$ and force vector at each end node of b and c, $\mathbf{F}_{b,beam}$ and $\mathbf{F}_{c,beam}$, are the components of the elasto-plastic beam-column element with plastic hinges that were explained in the previous chapter, and $\mathbf{P}_1$ and $\mathbf{P}_2$ are the external load vector for each outer node, 1 and 2. Thus, $\mathbf{g}_1, \mathbf{g}_b, \mathbf{g}_c, \mathbf{g}_2$ are the semi-rigid spring force vectors and can be written as follows:

$$\begin{Bmatrix} \mathbf{g}_1 \\ \mathbf{g}_b \end{Bmatrix} = \mathbf{b}_1^T \begin{Bmatrix} \mathbf{F}_{1,s1} \\ \mathbf{F}_{b,s1} \end{Bmatrix} = \mathbf{b}_1^T \begin{Bmatrix} \mathbf{F}_{a,s1} \\ \mathbf{F}_{b,s1} \end{Bmatrix}, \quad \begin{Bmatrix} \mathbf{g}_c \\ \mathbf{g}_2 \end{Bmatrix} = \mathbf{b}_2^T \begin{Bmatrix} \mathbf{F}_{c,s2} \\ \mathbf{F}_{2,s2} \end{Bmatrix} = \mathbf{b}_2^T \begin{Bmatrix} \mathbf{F}_{c,s2} \\ \mathbf{F}_{d,s2} \end{Bmatrix} \tag{48}$$

The reassembled form of Eq. 47 for each inner (b, c) and outer (1, 2) node is as follows:

$$\begin{bmatrix} \mathbf{A} & \mathbf{B} \\ \mathbf{B}^T & \mathbf{C} \end{bmatrix} \begin{Bmatrix} \delta\mathbf{d}_{12} \\ \delta\mathbf{d}_{bc} \end{Bmatrix} + \begin{Bmatrix} \mathbf{G}_{12} \\ \mathbf{G}_{bc} \end{Bmatrix} = \begin{Bmatrix} \mathbf{P}_{12} \\ 0 \end{Bmatrix} \tag{49}$$

$$\delta\mathbf{d}_{12} = \begin{Bmatrix} \delta\mathbf{d}_1 \\ \delta\mathbf{d}_2 \end{Bmatrix}, \quad \delta\mathbf{d}_{bc} = \begin{Bmatrix} \delta\mathbf{d}_b \\ \delta\mathbf{d}_c \end{Bmatrix} \tag{50}$$

$$\mathbf{G}_{12}=\begin{Bmatrix}\mathbf{g}_1\\ \mathbf{g}_2\end{Bmatrix},\quad \mathbf{G}_{bc}=\begin{Bmatrix}\mathbf{g}_b+\mathbf{F}_{b,beam}\\ \mathbf{F}_{c,beam}+\mathbf{g}_c\end{Bmatrix},\quad \mathbf{P}_{12}=\begin{Bmatrix}\mathbf{P}_1\\ \mathbf{P}_2\end{Bmatrix} \tag{51}$$

From the static condensation procedure, the equilibrium equation of the composed element of Figure 4 can be written as follows:

$$\mathbf{K}\delta\mathbf{d}_{12}=\mathbf{P}_{12}-\mathbf{F} \tag{52}$$

Where

$$\mathbf{K}=\mathbf{A}-\mathbf{B}\mathbf{C}^{-1}\mathbf{B}^{T} \tag{53}$$

$$\mathbf{F}=\mathbf{G}_{12}-\mathbf{B}\mathbf{C}^{-1}\mathbf{G}_{bc} \tag{54}$$

Figure 5 illustrates the various modeling capacities of the proposed semi-rigid, elasto-plastic beam-column element. The formulation of the proposed element was obtained from the previous, well-defined research of Spiller [12], Levy and Spiller [15], Kassimali and Abbasnia [8], Abbasnia and Kassimali [11] and Kato [67]. The numerical accuracy and capacity were verified by the following examples.

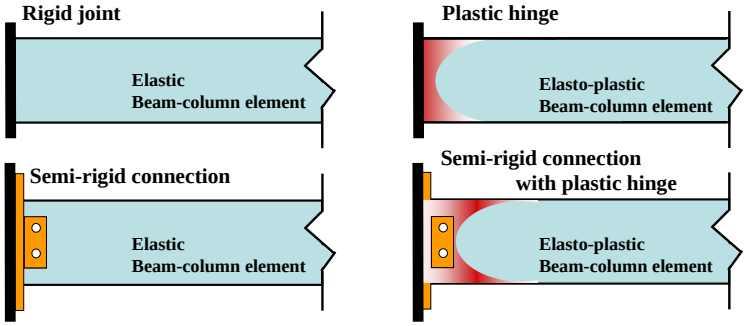

Figure 5. Various Modeling Capacities of the Proposed Element

6. VERIFICATION EXAMPLES

In an effort to assess the computational merits and limitations of the method of large deformation semi-rigid elasto-plastic analysis presented here, various numerical examples were solved with the proposed approach, and comparisons were made with previously published results. To trace the complete load-deflection curve, the arc-length method was adopted.

Examples 6.1 and 6.2 are presented to demonstrate the accuracy of the proposed beam-column element (section 3.1) and approximate beam-column element (section 3.2) in conducting large-deformational elastic post-buckling analysis. Example 6.3 verifies the semi-rigid elastic post-buckling analysis. Example 6.4 verifies the plastic analysis of the bent frame which is governed by the tosional moment. Examples 6.5 and 6.6 verify the semi-rigid plastic collapse analysis.

Example 6.1: Williams' toggle frame

Williams' toggle frame has been analyzed by many researchers to verify the numerical accuracy of their studies. Williams solved this frame using analytical and experimental tests. Papadrakakis [7]

solved this problem by using the beam-column approach. Meek and Tan [47] used the so-called co-rotational finite element approach. Liew et al. [79] used the improved cubic element approach that accounts for some coupling effects. Wood and Zienkiewicz [35] employed a total Lagrangian finite element formulation in a continuous approach with five isoparametric elements per member.

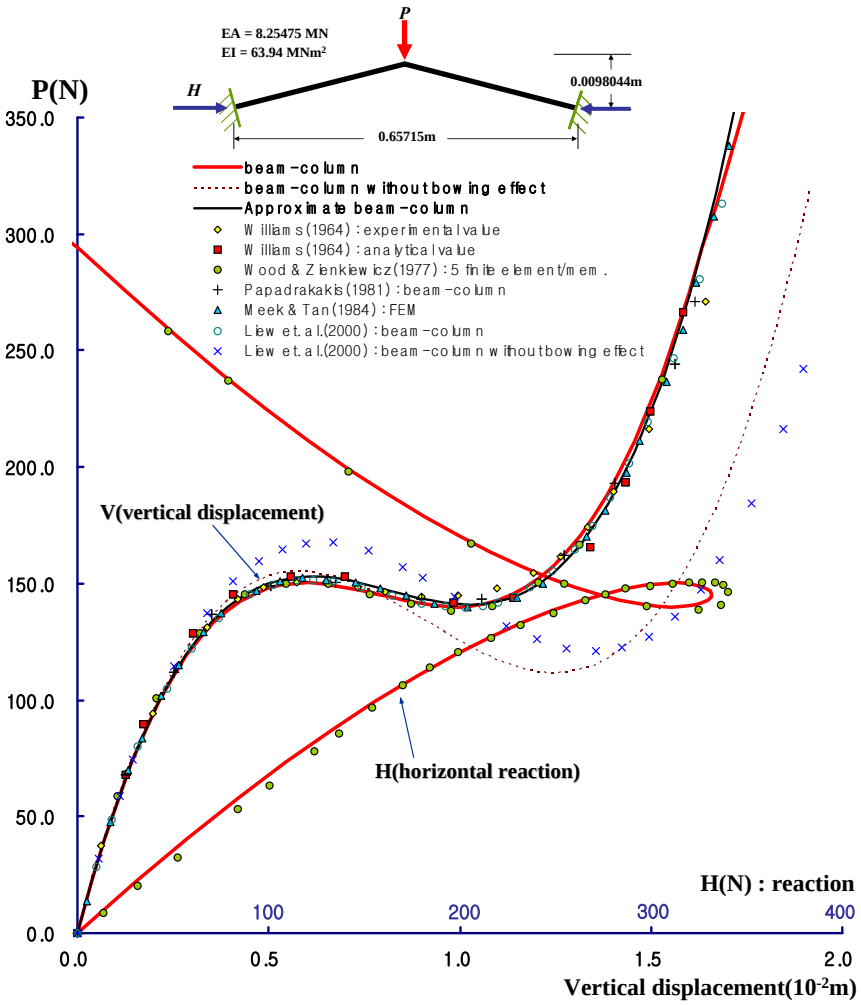

Figure 6. Williams' Toggle Frame: Geometry and Load-deflection Curves

The results of this problem, as obtained in this study, are illustrated in Figure 6 with one element per member as Papadrakakis [7], Meek and Tan [47] and Liew et al. [79]. The load-deflection curves are in good agreement with previous result curves. The load-deflection curve determined using the proposed beam-column element with a bowing effect is very close to the results predicted by Paradrakakis [7] and Liew et al. [79]. Our results without the bowing effect are similar to the results of Liew et al. [79] after the limit point of the post-buckling range, which did not consider the bowing effect. The load-deflection curve of the approximate beam-column approach is in good agreement with the curve of Meek and Tan [47].

Example 6.2: 12-member hexagonal space frame

The geometry and load-deflection curves for the 12-member frame dome are illustrated in Figure 7. The boundary conditions for this problem are roller and pin support. The results curves obtained using the proposed formulation, beam-column and approximate beam-column methods are plotted according to the boundary conditions. The resulting curves are in good agreement with previously published results [7,47,48,58,79,80].

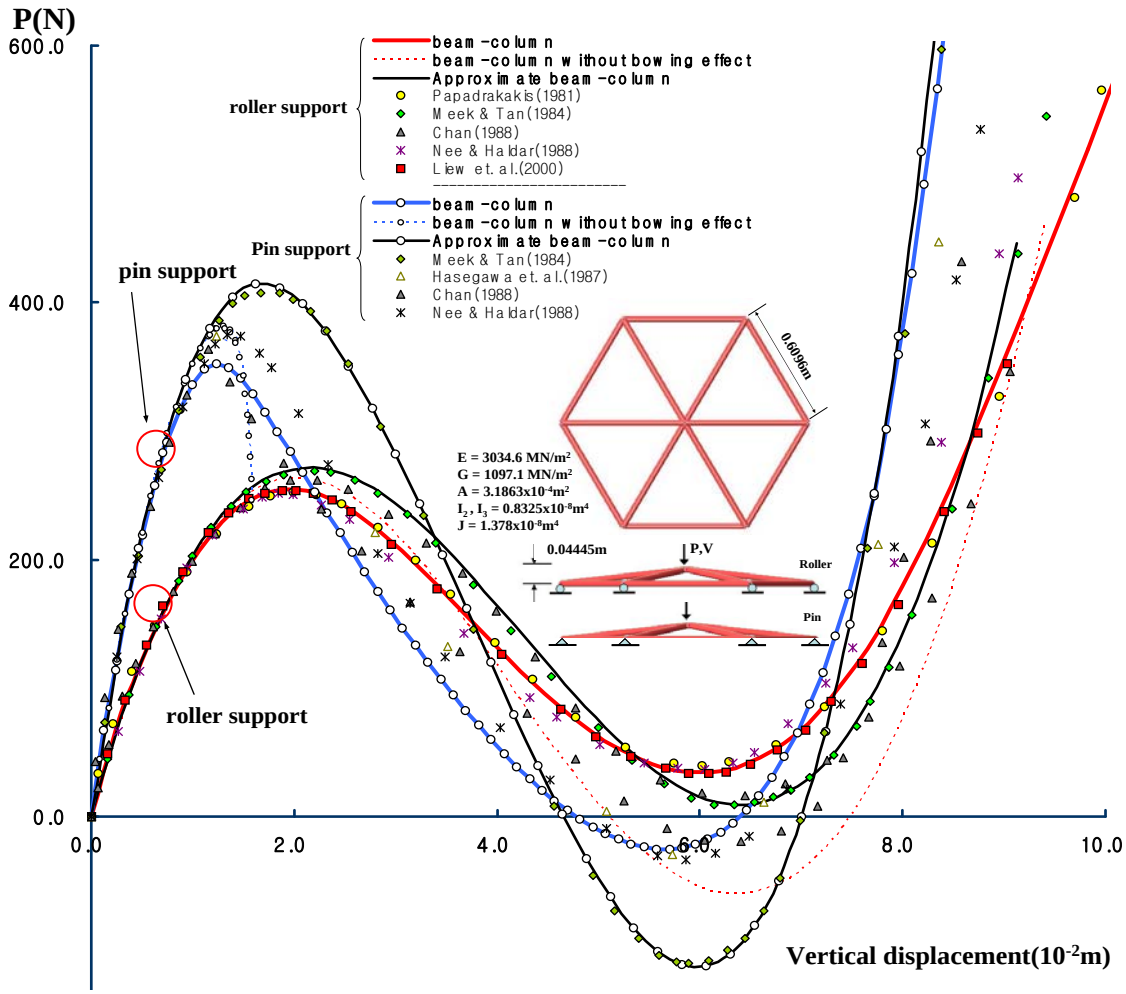

Figure 7. 12-member Frame Dome: Geometry and Load-deflection Curves

The load-deflection curve of the beam-column element is in accordance with Papadrakakis [7], Nee and Haldar [58] and Liew et al. [79] in the roller support condition and underestimates the load-deflection curves compared with the results of Hasegawa [80] and Nee and Haldar [58] in the pin-support condition. The load-deflection curves of the approximate beam-column element are in good agreement with Meek and Tan [47] for each boundary condition case. Chan [48] used two elements per member to analyze this problem using co-rotational cubic elements. Chan's load-deflection curves are plotted between the curves of the beam-column and approximate beam-column elements for the roller support condition. This implies the well-known fact that the beam-column element is more exact than the FE formulate element. Generally, a larger number of elements per member are needed to obtain an exact solution when a finite element formulation space frame is used.

Example 6.3: 24-member hexagonal star-shaped shallow dome

This model is known as the Stardome and is used as a verification example for nonlinear analysis of truss models. However, Meek and Tan [47] solved this problem as a rigid jointed space frame by keeping the member cross sectional area but decreasing the flexural stiffness in the vertical plane. The geometry and section properties are shown in Figure 8. Section type-1 and Section type-2 are rigid joints; Section type-3 is a pin joint. As shown in Figure 9, the load-deflection of the rigid jointed space frame converge to that of the pin-jointed truss load-deflection curve as the stiffness of section decreases. Finally, the structure was found to exhibit snap-through buckling.

To verify the accuracy and applicability of the proposed semi-rigid connected beam-column element, the semi-rigid spring element, as described in Table 1, was introduced in both Section type-1 and Section type-2, and the structural flexibility was predicted with corresponding semi-rigid connection properties.

As shown in Figure 9, the resulting curves determined by the approximate beam-column element are in good agreement with the previous results of Meek and Tan [47]. It can be seen that the load-deflection path of the beam-column element gradually differs from that of the approximate beam-column in the large deformational post-buckling range of high axial force levels. These phenomenon result from the omission of the higher order terms in Eqs. 19-22 of approximate beam-column equation.

By decreasing the semi-rigidity of the connection, the structural behaviors tend to be more flexible and finally converge to a pin-jointed truss model, as shown in Figure 10 and Figure 11, which differ only in section properties.

Table 1. Semi-rigid Spring Rigidities for the 24-member Shallow Dome

	k_x	$k_{\theta 2}$	$k_{\theta 3}$
Semi-rigid type-1	EA	$EI_2 \times 0.5$	$EI_3 \times 0.5$
Semi-rigid type-2	EA	$EI_2 \times 0.1$	$EI_3 \times 0.1$
Semi-rigid type-3	EA	$EI_2 \times 0.02$	$EI_3 \times 0.02$

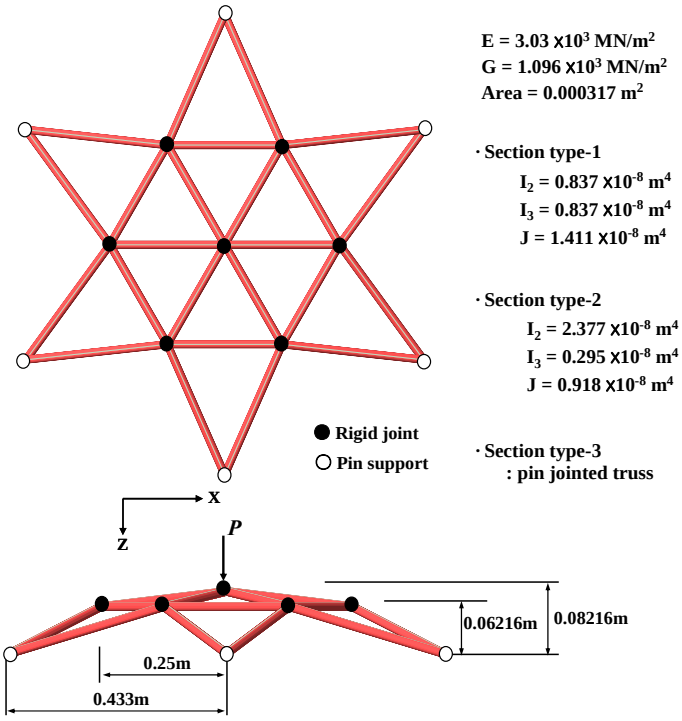

Figure 8. 24-member Shallow Dome: Geometry and Section Properties

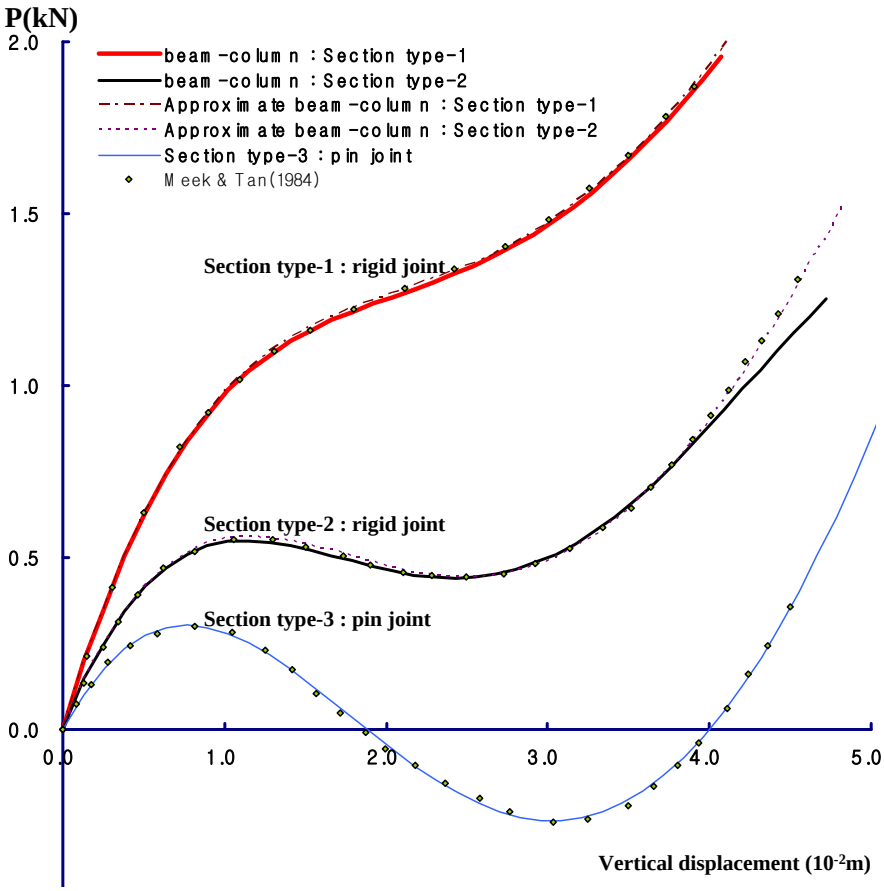

Figure 9. 24-member Shallow Dome: Load-deflection Curves for Each Section Types

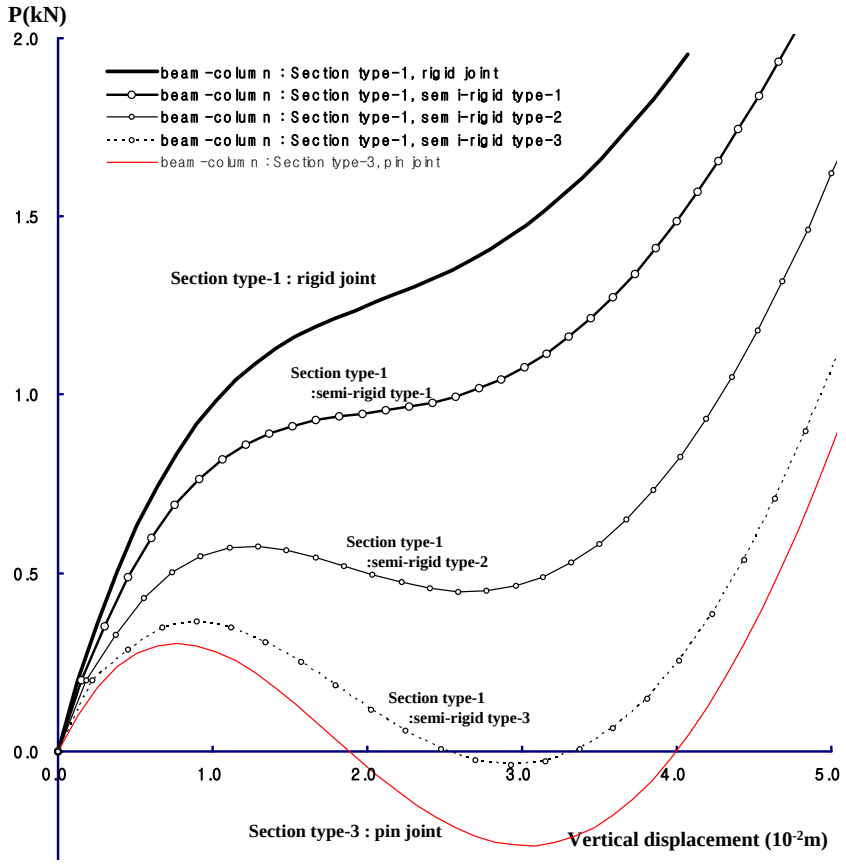

Figure 10. 24-member Shallow Dome: Load-deflection Curve for Semi-rigid Section Type-1

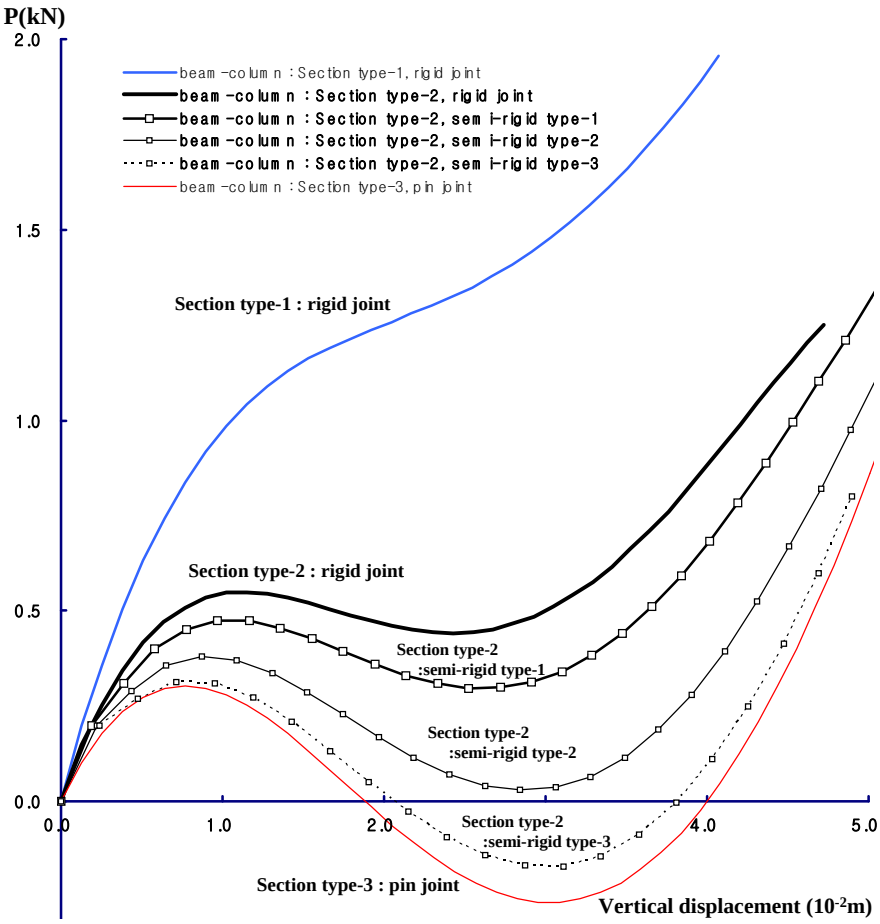

Figure 11. 24-member Shallow Dome: Load-deflection Curve for Semi-rigid Section Type-2

Example 6.4: Horizontal bent frame

The elasto-plastic analysis of a right-angle bent frame, as shown in Figure 12, was performed. The bent frame was subjected to a concentrated out-of-plane load in the vertical direction. A plastic hinge occurs at A→D→B nodes, sequentially. Shi and Atluri [57] used a yield function in which the interaction between the bending and torsional moments is considered, but the effect of axial force is neglected. Nee and Haldar [58] reported a load-deflection curve shape identical to that of Shi and Atluri [57] with a different yield function. Abbasnia and Kassimali [11] analyzed this problem with different cross section properties than those used by Nee and Haldar [58] and reported the behavior of large deformational rigid-body rotations.

To verify the response to the problem, two types of input models were considered for Nee and Haldar [58] and Abbasnia and Kassimali [11]; the elasto-plastic analysis was performed for the two models. Figures 12 and 13 illustrate the results of the load-deflection curves and deformed configurations. The results of the maximum load parameter (6.68) and the load-deflection curve obtained in this study are in good agreement with the results of Abbasnia and Kassimali [11], as shown in Figure 12. When the effects of plastic torsional deformation, given by Eq. 35, are not considered, a small deformation response may be obtained for a bent frame, and the load-deflection curves converge to those of Nee and Haldar [58] and Shi and Atluri [57], as shown in Figure 13.

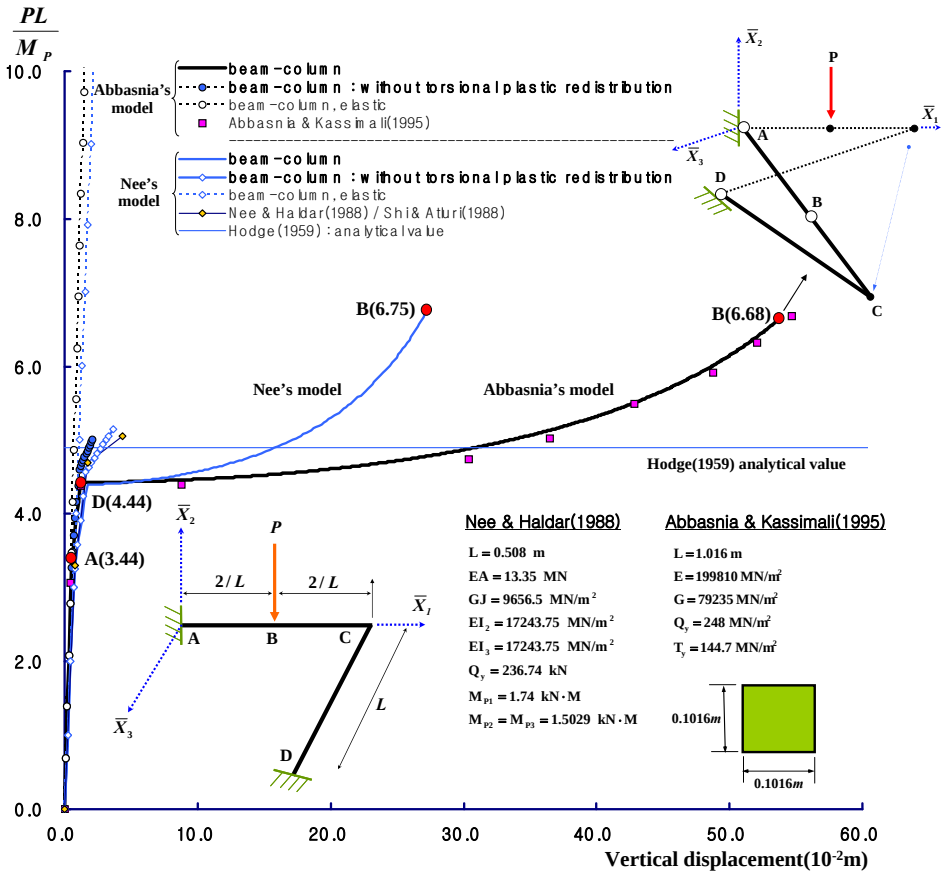

Figure 12. Horizontal Bent Frame: Geometry and Load-deflection Curve

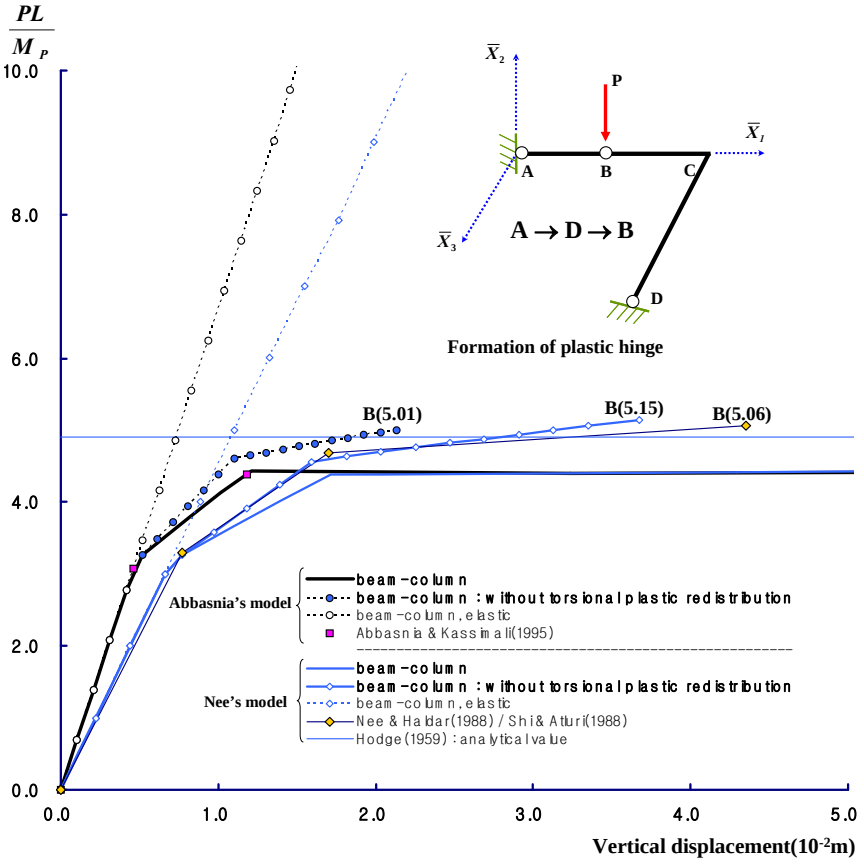

Figure 13. Horizontal Bent Frame: Detailed Load-deflection Curve

As noted by Abbasnia and Kassimali [11], after a plastic hinge develops at nodes A and D, the structure becomes geometrically unstable and undergoes large rigid-body rotations to develop resistance to the applied load until a plastic hinge develops at node B.

The results of the maximum load parameter (6.68) and the load-deflection curve obtained in this study are in good agreement with the results of Abbasnia and Kassimali [11], as shown in Figure 12. When the effects of plastic torsional deformation, given by Eq. 35, are not considered, a small deformation response may be obtained for a bent frame, and the load-deflection curves converge to those of Nee and Haldar [58] and Shi and Atluri [57], as shown in Figure 13. As noted by Abbasnia and Kassimali [11], after a plastic hinge develops at nodes A and D, the structure becomes geometrically unstable and undergoes large rigid-body rotations to develop resistance to the applied load until a plastic hinge develops at node B.

Hodge [81] reported the corresponding value of the load parameter to be 4.9. Ueda and Yao [82] showed that the load parameter obtained by Hodge was the lower bound. Thus, the result of this example may be understood as acceptable and reasonable for elasto-plastic analysis.

Example 6.5: 18-member frame dome

This verification example is an 18-member frame dome used to analyze the semi-rigid elasto-plastic large deformational response, as shown in Figures 14 and 15. The overall comparative load-deflection curves that are plotted in these figures show good agreement with previously reported results. Paradrakakis [83] used a finite element-formulated 48-member system for this problem. However, many other researchers [11,34,56,57] used one element per member, as in this study.

The results obtained using the proposed beam-column element show good agreement with the results of Kassimali and Abbasnia [8] until the buckling range is reached; our load-deflection curve proceeded until the large deformational post-buckling range, as shown in Figure 14. The elastic analysis capacity of the proposed elements has acceptable merit and applicability. Moreover, the elasto-plastic response of this problem shows good agreement with the results of Agyris et al. [34] and Abbasnia and Kassimali [11] until the plastic limit point. Conversely, in this study, after this limit point, the analysis procedure and structural response continued until plastic hinges occurred at node 3 with elasto-plastic large deformational behaviors.

The bowing effect of the proposed beam-column element influences the comprehensive effect for the elastic response governed by the geometric nonlinearity but not for the plastic case. The load-deflection curves are closely plotted for the low axial-force level, plastic analysis case, as shown in Figure 14. Therefore, for the plastic analysis case, it is not necessary to consider the bowing effect. Such a phenomenon also occurred in Example 6.6 (below). The collapse mechanism for this example goes sequentially to nodes ①→②→③; the load levels and the points at which the plastic hinges occurred are marked in the figure.

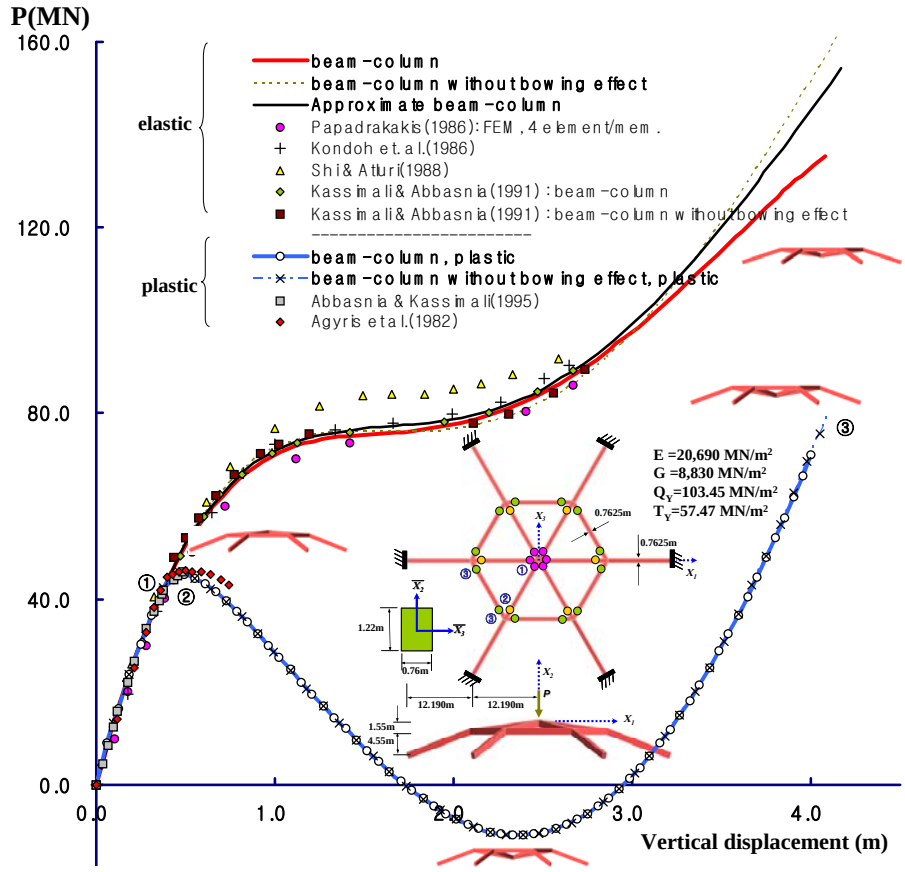

Figure 14. 18-member Frame Dome: Geometry and Load-deflection Curve

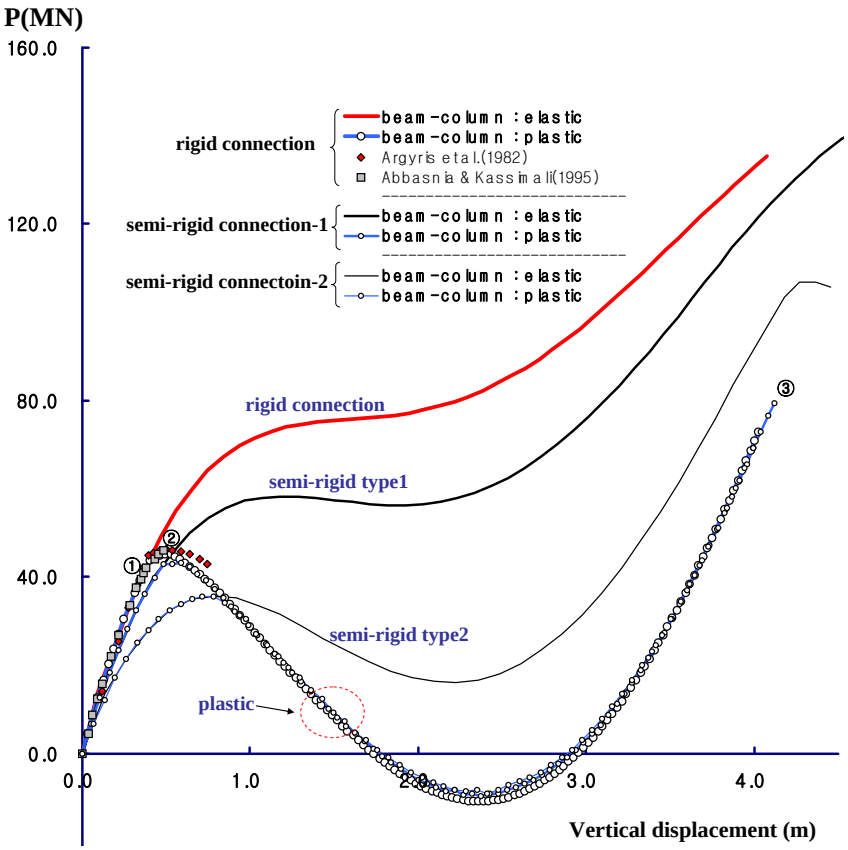

Figure 15. 18-member Frame Dome: Semi-rigid Elasto-plastic Response

Table 2. Semi-rigid Spring Rigidities for the 18-member Frame Dome

	k_x	$k_{\theta 2}$	$k_{\theta 3}$
Semi-rigid type-1	EA	$EI_2 \times 0.3$	$EI_3 \times 0.3$
Semi-rigid type-2	EA	$EI_2 \times 0.05$	$EI_3 \times 0.05$

Figure 15 shows the semi-rigid elasto-plastic response of this example. The elastic semi-rigid spring rigidities are described in Table 2. From the analyzed response, it can be seen that the elastic and plastic limit load levels are influenced by the applied semi-rigidities. The plastic hinges of perfect plastic material model without strain-hardening of joint ① and ② make the structure as ideally pin jointed dome structures. Therefore, the load-deflection paths after plastic limit load trace similar curves. The elastic semi-rigid joint flexibility influences the response of elastic load-deflection curves but not plastic case.

Example 6.6: two-story frame

A two-story frame, as shown in Figure 16, was verified for the semi-rigid elasto-plastic analysis. Plastic zone and plastic hinge approaches were used by Argyris et al. [34] and Abbasnia and Kassimali [11] respectively. The load-deflection curves at node (a) in Figure 16 are illustrated in Figure 17. As a result, the response curve shows good agreement with results of previous work by Argyris et al. [34] and Abbasnia and Kassimali [11]. The bowing effect slightly influences the plastic response in this example, as also seen in Example 6.5 for the plastic case. The sequence of the plastic hinge formation or collapse mechanism is from ①→②→③→④→⑤ nodes of Figure 16. Figure 18 shows the deformed shape of structures according to the analysis results.

The four-parameter Ramberg-Osgood hysteresis model of Hart and Wilson [84] was adopted in this example for the y- and z-axis rotational terms. The initial stiffness of the semi-rigid springs are illustrated in Table 3, and the relative spring yielding values for each axis are assumed as the value of the connected member. According to the semi-rigid flexibility of connections with Ramberg-Osgood control parameters α and γ, the load-deflection curves are plotted in Figure 17.

Table 3. Semi-rigid Spring Rigidities for a Two-story Frame

	k_x	$k_{\theta 2}$	$k_{\theta 3}$
Semi-rigid	EA	$EI_2 \times 0.04$	$EI_3 \times 0.04$

7. CONCLUSION

The elasto-plastic post-buckling analysis of a semi-rigid space frame is presented. The Eulerian finite deformation formulations were included for large deformations and small strains. The formulation to represent the space frame was a conventional beam-column element with a bowing effect. The lateral-torsional effect was included in asymmetric rotational tangent stiffness. However, the shear, axial-torsional and warping effects were not considered for the sake of simplicity. The joint connection characteristics were represented by semi-rigid spring elements. The well-known static condensation processes were adopted for the element stiffness and equilibrium equations. Highly nonlinear load-deflection curves were traced by the arc-length method with an asymmetric tangent stiffness matrix.

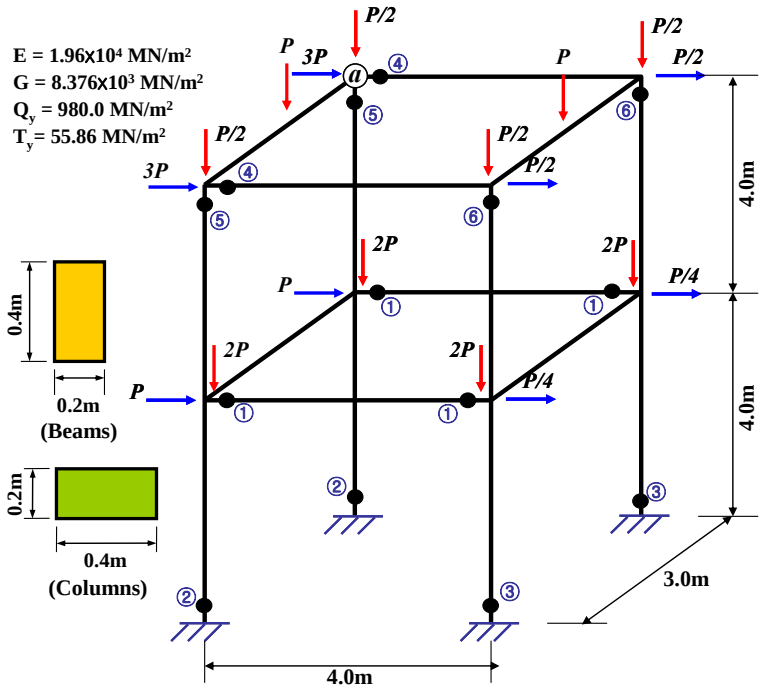

Figure 16. Two-story frame: geometry and properties

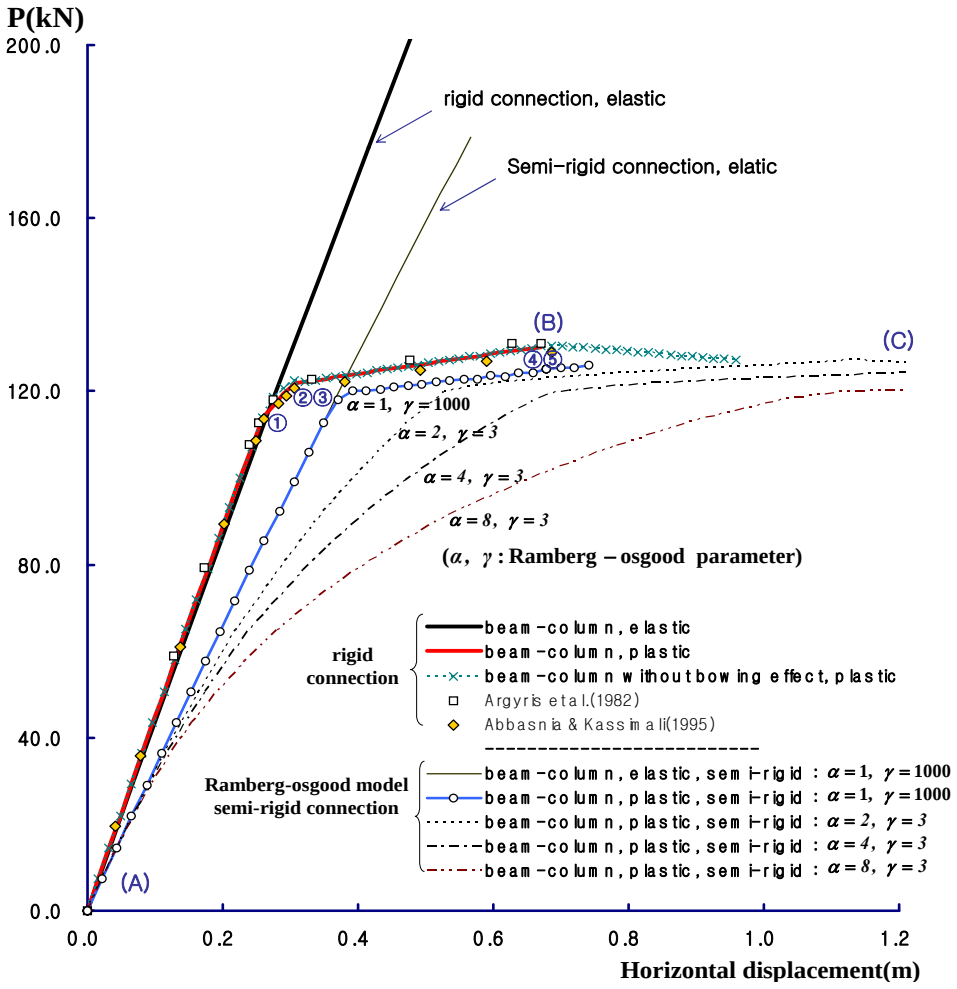

Figure 17. Two-story Frame: Load-deflection Curves

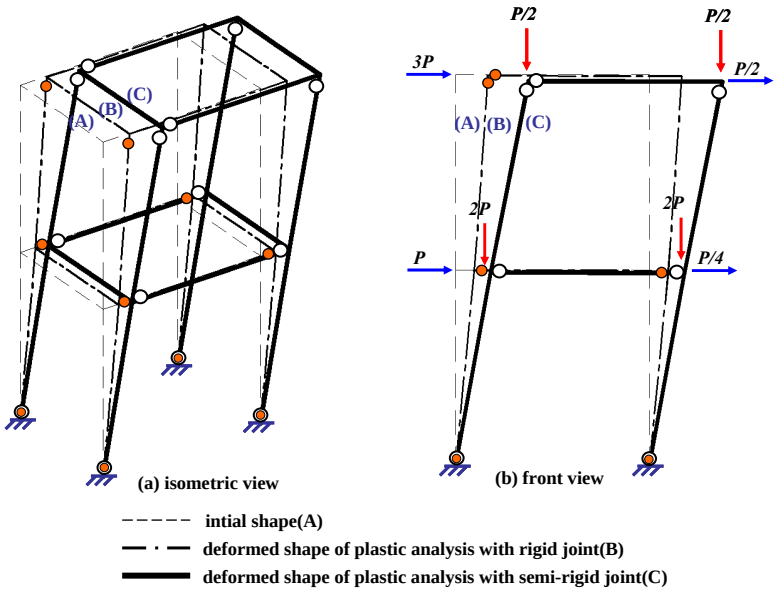

Figure 18. Two-story Frame: Deformed Shape

The proposed simple and effective space frame element with a semi-rigid connection is the result of well-defined and previously reported research. The theories were combined for the purposes of numerical capacity and applicability. The results of the verified examples show good agreement with results in the literature. Moreover, in some cases, newly reported result curves and values are obtained. It was observed that the proposed method is reliable and accurate for studying the post-buckling behavior of finite deformed space frames and is applicable to various nonlinear problems.

ACKNOWLEDGEMENTS

This research was supported by a grant (code#'09 R&D A01) from Cutting-edge Urban Development Program funded by the Ministry of Land, Transport and Maritime Affairs of Korean government.

REFERENCES

[1] Renton, J.D., "Stability of Space Frames by Computer Analysis", J. Sruct. Div., ASCE, 1962, Vol. 88, No. 8, pp. 81-103.

[2] Saafan, S.A., "Nonlinear Behavior of Structural Plane Frames", J. Sruct. Div., ASCE, 1962, Vol. 89, No. 4, pp. 557-579.

[3] Oran, C., "Tangent Stiffness in Space Frame", J. Struc. Div., ASCE, 1973, Vol. 99, No. 6, pp. 987-1001.

[4] Chen, W.F. and Lui, E.M., "Stability Design of Steel Frames", CRC Press, 1991.

[5] Chen, W.F., Goto, Y. and Liew, J.Y.R., "Stability Design of Semi-Rigid Frames", John Willey & Sons, Inc, 1996.

[6] Chen, W.F. and Kim, S.E., "LRFD Steel Design using Advanced Analysis", CRC Press Boca Raton (FL), 1997.

[7] Papadrakakis, M., "Post Buckling Analysis of Spatial Structures by Vector Iteration Methods", Computers & Structures, 1981, Vol. 14, pp. 393-402.

[8] Kassimali, A. and Abbasnia, R., "Large Deformation Analysis of Elastic Space Frames", J. Struct. Eng., ASCE, 1991, Vol. 117, No. 7, pp. 2067-2087.
[9] Kassimali, A., "Large Deflection Analysis of Elastic-plastic Frames", J. Struct. Eng., ASCE, 1983, Vol. 109, No. 8, pp. 1869-1886.
[10] Chandra, R., Krishna, P. and Trikha, D.N., "Elastic-plastic Analysis of Steel Space Structures", J. Struct. Engng, ASCE, 1990, Vol. 26, No. 3, pp. 939-955.
[11] Abbasnia, R. and Kassimali, A., "Large Deformation Elastic-plastic Analysis of Space Frames", J. Construct. Steel Research, 1995, Vol. 35, pp. 275-290.
[12] Spillers, W.R., "Geometric Stiffness Matrix for Space Frames", Computers & Structures, 1990, Vol. 36, No. 1, pp. 29-37.
[13] Spillers, W.R. and Shams, M.H., "Three-Dimensional Beam-Columns", Computers & Structures, 1994, Vol. 52, No. 3, pp. 449-460.
[14] Spillers, W.R. and Rashidi, S., "Member Stiffness for Three-Dimensional Beam-Columns", J. Struct. Eng., ASCE, 1997, Vol. 127, No. 7, pp. 971-972.
[15] Levy, R. and Spillers, W.R., "Analysis of Geometrically Nonlinear Structures, 2nd ed.", Kluwer Academic Publishers, 2003.
[16] Kim, S.E., Kim, Y. and Choi, S.H., "Nonlinear Analysis of 3-D Steel Frames", Thin Walled Struct, 2001, Vol. 39, pp.445-461.
[17] Kim, S.E. and Choi, S.H., "Practical Advanced Analysis for Semi-rigid Space Frames", Internat. J. Solids Structures, 2001, Vol. 38, No.50-51, pp. 9111-9131.
[17] Kim, S.E., Park, M.H. and Choi, S.H., "Direct Design of Three-dimensional Frames using Practical Advanced Analysis", Engineering Structures, 2001, Vol. 23, No. 11, pp. 1491-1502.
[18] Gallagher, R.H. and Padlog, J., "Discrete Element Approach to Structural Instability Analysis", AAIA J., 1963, Vol. 1, 1437–1439.
[19] Przemieniecki, J.S., "Theory of Matrix Structural Analysis", New York, McGraw-Hill, 1968.
[20] Jennings, A., "Frame Analysis including Change in Geometry", J. Struct. Div, ASCE, 1968, Vol. 94, pp. 627–44.
[21] Porter, F.L. and Powell, G.H., "Static and Dynamic Analysis of Inelastic Framed Structures", Report No. EERC 71-3. Earthquake Engineering Research Centre, University of California at Berkeley, CA, 1971.
[22] Chen, P.F. and Powell, G.H., "Generalized Plastic Hinge Concepts for 3D Beam-column Elements", Report No. EERC 82-20. Earthquake Engineering Research Centre, University of California at Berkeley, CA, 1982.
[23] Powell, G.H. and Chen, P.F., "3-D Beam-column Element with Generalized Plastic Hinges", J. Engng. Mech. ASCE, 1986, Vol. 112, No. 7, pp. 627-641.
[24] Gattass, M. and Abel, J.F., "Equilibrium Considerations of the Updated Lagrangian Formulation of Beam–columns with Natural Concepts", Int. J. Numer. Meth. Engng., 1987, Vol. 24, pp. 2119-2141.
[25] Makowski, Z.S., "Regular Lattice Plates and Shells", Elsevier, 1990.
[26] White, D.W. and Hajjar, J., "Application of Second-order Elastic Analysis in LRFD: Research to Practice", Engng. J, AISC, 1991, Vol. 28, pp. 133–148.
[27] Yang, Y.B. and Leu, L.J., "Non-linear Stiffnesses in Analysis of Planar Frames", Comput. Methods Appl. Mech. Engrg. 1994, Vol. 117, pp. 233–247.
[28] Yang, Y.B. and Kuo, S.R., "Theory & Analysis of Nonlinear Frames", Prentice-Hall, 1994.
[29] McGuire, W., Gallagher, R.H. and Ziemian, R., "Matrix Structural Analysis, 2nd Ed." New York, John Wiley and Sons, 2000.

[30] Argyris, J., “An excursion into Large Rotations”, Comput. Methods Appl. Mech. Engrg., 1982, Vol. 32, pp. 85–155.

[31] Argyris, J.H., Dunne, P.C. and Scharpf, D.W., “On Large Displacement Small Strain Analysis of Structures with Rotational Degrees of Freedom”, Comput. Methods Appl. Mech. Engrg., 1978, Vol. 14, pp. 401-451.

[32] Argyris, J.H., Balmer, H., Doltsinis, I.S.T., Dunne, P.C., Haase, M., Kleiber, M., Malejannakis G.A., Mlejnek, H.P., Muller, M. and Scharpf, D.W., “Finite Element Method-The Natural Approach”, Comput. Methods Appl. Mech. Engrg., 1979, Vol. 17/18, pp. 1-106.

[33] Argyris, J.H., Hilpert, O., Malejannakis, G.A. and Scharpf, D.W., “On the Geometrical Stiffness of a Beam in Space—A Consistent v.w. approach”, Comput. Methods Appl. Mech. Engrg., 1979, Vol. 20, pp. 105-131.

[34] Argyris, J.H., Boni, B., Hindenlang, U. and Kleiber, M., “Finite Element Analysis of Two and Three Dimensional Elasto-plasic Frames-The Natural Approach”, Comput. Methods Appl. Mech. Engrg., 1982, Vol. 35, pp. 221-248.

[35] Wood, R.D. and Zienkiewicz, O.C., “Geometrically Non-linear Finite Element Analysis of Beam, Frames, Arches and Axisymmetric Shells”, Computers & Structures, 1977, Vol. 7, pp. 725-735.

[36] Bathe, K.J. and Bolourchi, S., “Large Displacement Analysis of Three-dimensional Beam Structures”, Int. J. Num. Meth. Eng., 1979, Vol. 14, pp. 961-986.

[37] Reissner, E., “On Finite Deformation of Space-curved Beams”, J. Appl. Math. Phys., 1981, Vol. 32, pp. 734–744.

[38] Simo, J.C., “A Finite Strain Beam Formulation, Part I, The Three-dimensional Dynamic Problem”, Comput. Methods Appl. Mech. Engrg., 1985, Vol. 49, pp. 55–70.

[39] Simo, J.C. and Vu-Quoc, L., “A Three-dimensional Finite-strain Rod Model, Part II, Computational Aspects”, Comput. Methods Appl. Mech. Engrg., 1986, Vol. 58, pp. 79–116.

[40] Simo, J.C. and Vu-Quoc, L., “On the Dynamics in Space of Rods Undergoing Large Motions–A Geometrically Exact Approach”, Comput. Methods Appl. Mech. Engrg., 1988, Vol. 66, pp. 125–161.

[41] Simo, J.C. and Vu-Quoc, L., “A Geometrically Exact Rod Model Incorporating Shear and Torsion-warping Deformation”, Int. J. Solids Struct., 1991, Vol. 27, pp. 371–393.

[42] Simo, J.C., “The (Symmetric) Hessian for Geometrically Nonlinear Models in Solid Mechanics: Intrinsic Definition and Geometric Interpretation”, Comput. Methods Appl. Mech. Engrg., 1992, Vol. 96, pp. 189–200.

[43] Cardona, A. and Geradin, M., “A Beam Finite Element Non-linear Theory with Finite Rotations”, International Journal for Numerical Methods in Engineering, 1988, Vol. 26, pp. 2403-2438.

[44] Ibrahimbegovic, A., “Computational Aspects of Vector-like Parametrization of three-dimensional finite rotations”, Int. J. Num. Meth. Eng., 1995, Vol. 38, pp. 3653-3673.

[45] Zupan, D. and Saje, M., “Finite-element Formulation of Geometrically Exact Three-dimensional Beam Theories based on Interpolation of Strain Measures”, Comput. Methods Appl. Mech. Engrg., 2003, Vol. 192, pp. 5209–5248.

[46] Mata, P., Oller, S. and Barbat, A.H., “Static Analysis of Beam Structures under Nonlinear Geometric and Constitutive Behavior”, Comput. Methods Appl. Mech. Engrg., 2007, Vol. 196, pp. 4458–4478.

[47] Meek, J.L. and Tan, H.S., “Geometrically Nonlinear Analysis of Space Frames by an Incremental Iterative Technique”, Comput. Methods Appl. Mech. Engrg., 1984, Vol. 47, pp. 261-282.

[48] Chan, S.L., "Geometric and Material Nonlinear Analysis of Beam-Columns and Frames Using the Minimum Residual Displacement Method", Int. J. Num. Meth. Eng., 1988, Vol. 26, No. 12, pp. 2657-2669.

[49] Crisfield, M.A. and Cole, G., "Co-rotational Beam Elements for Two and Three-dimensional Nonlinear Analysis, Discretisation Methods in Structural Mechnics", Ed. Kuhn, G. and Mang, H., Spring-Verlag, 1989, pp. 115-124.

[50] Crisfield, M.A., "A Consistent Co-rotational Formulation for Nonlinear Three Dimensional Beam Elements", Comput. Methods Appl. Mech. Engrg., 1990, Vol. 81, pp. 131-150.

[51] Nour-Omid, B. and Rankin, C.C., "Finite Rotation Analysis and Consistent Linearization using Projectors", Comput. Methods Appl. Mech. Eng., 1991, Vol. 93, pp. 353-384.

[52] Teh, L.H. and Clarke, M.J., "Co-rotational and Lagrangian Formulations of Elastic Three-dimensional Beam Finite Elements", J. Construct. Steel Research, 1998, Vol. 48, pp. 23–44.

[53] Battini, J.M. and Pacoste, C., "Co-rotational Beam Elements with Warping Effects in Instability Problems", Comput. Methods Appl. Mech. Engrg., 2002, Vol. 191, pp. 1755–1789.

[54] Battini, J.M. and Pacoste, C., "Plastic Instability of Beam Structures using Co-rotational Elements", Comput. Methods Appl. Mech. Engrg., 2002, Vol. 191, pp. 5811–5831.

[55] Izzuddin, B.A. and Elnashai, A.S., "Eulerian Formulation for Large Displacement Analysis of Space Frames", J. Eng. Mech., ASCE, 1993, Vol. 119, No. 3, pp. 549-569.

[56] Kondoh, K. and Atluri, S.N., "Simplified Finite Element Method for Large Deformation, Post-Buckling Analysis of Large Frame Structures, Using Explicurly Derived Tangent Stiffness Matrices", Int. J. Num. Meth. Eng., 1986, Vol. 3, No. 1, pp. 69-90.

[57] Shi, G. and Atluri, S.N., "Elasto-plastic Large Deformation Analysis of Space-frames : A Plastic-hinge and Stress-based Explicit Derivation of Tangent Stiffness", Int. J. Num. Meth. Eng., 1988, Vol. 26, pp. 589-615.

[58] Nee, K.M. and Haldar, A., "Elastoplastic Nonlinear Post-Buckling Analysis of Partially Restrained Space Structures", Comput. Methods Appl. Mech. Engrg., 1988, Vol. 71, pp. 69-97.

[59] Downer, J.D., Park, K.C. and Chiou, J.C., 'Dynamics of Flexible Beams for Multibody Systems: A Computational Procedure', Comput. Methods Appl. Mech. Engrg., 1992, Vol. 96, pp. 373-408.

[60] Park, M.S. and Lee, B.C., "Geometrically Non-linear and Elastoplastic Threedimensional Shear Flexible Beam Element of Von-Mises-type Hardening Material", Int. J. Numer. Methods Engrg., 1996, Vol. 39, pp. 383–408.

[61] Clarke, M.J. and Hancock, G.J., "Finite Element Nonlinear Analysis of Stressed-arch Frames", J. Struct. Engng., ASCE, 1991, Vol. 117, No.28, pp. 19–37.

[62] Attalla, M.R., Deierlein, G.G. and McGuire, W., "Spread of Plasticity: Quasi-plastic Hinge Approach", J. Struct. Eng., ASCE, 1994, Vol. 120, No. 8, pp. 2451-2473.

[63] Clarke, M.J. and Hancock, G.J., "A Study of Incremental-Iterative Strategies for Nonlinear Analysis" , Int. J. Numer. Methods Engrg., 1990, Vol. 29, pp. 1365-1391.

[64] The, L.H. and Clarke, M.J., "Plastic-zone Analysis of 3D Steel Frames using Beam Elements", J. Struct. Engng. 1999, Vol. 125, pp. 1328–1337.

[65] Gruttmann, R., Sauer, R. and Wagner, W., "Theory and Numerics of Three-dimensional Beams with Elastoplastic Behaviour", Int. J. Numer. Meth. Engrg., 2000, Vol. 48, pp. 1675–1702.

[66] Jiang, X.M., Chen, H. and Liew, J.Y.R., "Spread-of-plasticity Analysis of Three-dimensional Steel Frames", J. Construct. Steel Research, 2002, Vol. 58, No. 2, pp. 193-212.

[67] Kato, S., Mutoh, I. and Shomura, M., "Collapse of Semi-rigidly Jointed Reticulated Domes with Initial Geometric Imperfections", J. Construct. Steel Research, 1998, Vol. 48, pp. 145-168.

[68] Kato, S., Kim, J.M. and Cheong, M., "A New Proportioning Method for Member Sections of Single Layer Reticulated Domes Subjected to Uniform and Nonuniform Loadings", Engineering Structures, 2003, Vol. 25, pp. 1265–1278.

[69] Liu, Y., Xu, L. and Griersonb, D.E., "Compound-element Modeling Accounting for Semi-rigid Connections and Member Plasticity", Engineering Structures, 2008, Vol. 30, pp. 1292-1307.

[70] Sekulovic, M., Nefovska-Danilovic, M., "Contribution to Transient Analysis of Inelastic Steel Frames with Semi-rigid Connections", Engineering Structures, 2008, Vol. 30, pp. 976-989.

[71] Chiorean, C.G., "A Computer Method for Nonlinear Inelastic Analysis of 3D Semi-rigid Steel Frameworks", Engineering Structures, 2009, Vol. 31, No. 12, pp. 3016-3033.

[72] Crisfield, M.S., "A Fast Incremental Iterative Solution Procedure that Handles 'Snap Through'", Computers & Structures, 1981, Vol. 13, pp. 55-62.

[73] Ramm, E., "Strategies for Tracing the Nonlinear Response Near Limit Points", in : Wunderlich, W., Stein, E. and Bathe, K.J., Eds., Nonlinear Finite Element Analysis in Structural Mechanics. Springer, 1981, pp. 63-89.

[74] Crisfield, M.A., "Nonlinear Finite Element Analysis of Solids and Structures", Vol.1, Essentials, John Wiley & Sons, 1991.

[75] Crisfield, M.A., "Nonlinear Finite Element Analysis of Solids and Structures", Vol.2, Advanced Topics, John Wiley & Sons, 1997.

[76] Chan, S.L. and Zhou, Z.H., "Pointwise Equilibrium Polynomial Element for Nonlinear Analysis of Frames", J. Struct. Eng., ASCE, 1994, Vol. 120, pp. 1703–1717.

[77] Izzuddin, B.A., "Quartic Formulation for Elastic Beam-columns subject to Thermal Effects", J. Eng. Mech., ASCE, 1996, Vol. 122, pp. 861–71.

[78] Chan, S.L. and Zhou, Z.H., "Nonlinear Integrated Design and Analysis of Skeletal Structures by 1 Element per Member", Engineering Structures, 2000, Vol. 22, pp. 246–57.

[79] Liew, J.Y.R., Chen, H., Shanmugam, N.E. and Chen, W.F., "Improved Nonlinear Plastic Hinge Analysis of Space Frame Structures", Engineering Structures, 2000, Vol. 22, pp. 1324-1338.

[80] Hasegawa, A., Liyanage, K.K. and Nishino, F., "Non-iterative Nonlinear Analysis Scheme of Frames with Thin-walled Elastic Members", Structural Engrg./Earthquake Engrg., 1987, Vol. 4, pp. 45-55.

[81] Hodge, D.G., "Plastic Analysis of Structures", McGraw -Hill, New York, 1959.

[82] Ueda, Y., Yao, T., "The Plastic Node Method : A New Method of Plastic Analysis", Comput. Methods Appl. Mech. Engrg., 1982, Vol. 34, pp. 1089-1104.

[83] Papadrakakis, M. and Ghionis, P., "Conjugate Gradient Algorithms in Nonlinear Structural Analysis problems", Comput. Methods Appl. Mech. Engrg., 1986, Vol. 59, No. 1, pp. 11-27.

[84] Hart, J.D. and Wilson, E.L., "Simplified Earthquake Analysis of Buildings Including Site Effects", Report No.UCB/SEMM-89/23, Department of Civil Engineering, University of California, Berkeley, December, 1989.

EXPERIMENTAL STUDY ON VIBRATION BEHAVIOR OF COLD-FORM STEEL CONCRETE COMPOSITE FLOOR

Xuhong Zhou[1, 2], Yongjun He [1,*], Ziwen Jia [3] and Shaofeng Nie [4]

[1] *Professor, College of Civil Engineering, Hunan University, Changsha, 410082, PR China*
[2] *Professor, Lanzhou University, Lanzhou, 730000, PR China*
[3] *Graduate,* [4] *Lecturer, Chang'an University, Xi'an, 710064, PR China*
**(Corresponding author : E-mail: hyj0087@163.com)*

Received:23 December 2010; Revised: 28 February 2011; Accepted: 11 March 2011

ABSTRACT: This paper introduces the experimental study on vibration behavior of 4 full scale cold-formed steel composite floors. The research is focused on the fundamental frequency of composite floor, which considering the influence of screw spacing and rigid blocking under different loading cases during normal use. The test apparatus and test methods are introduced in details. Then, the finite element analysis model of cold-formed steel composite floors is set up to study the vibration behavior. Finite element analysis results in this paper are close to those of the experiments. The results of the tests and finite element analysis show that the flexural rigidity of composite floor can be improved by changing the spacing of screws. The fundamental frequency of composite floor with large spacing of screws, that connect profiled steel sheet and the flange of joists, is smaller than the composite floor with small screw spacing. The lateral stability of joists can be strengthened; the flexural rigidity and frequency of composite floor can be increased by setting rigid blocking at mid-span of the adjacent joist of the composite floor. The fundamental frequency of composite floor increases if the end restraints are enhanced. It is suggested that the fundamental frequency of cold-formed steel concrete composite floor should be more than 10Hz.

Keywords: Composite floor, Cold-formed steel, Fundamental frequency, Experimental study, Finite element analysis

1. INTRODUCTION

Vibrations caused by human activities have long been recognized as a major serviceability concern for residential floor systems. Cold-formed steel composite steel concrete slab residential floor systems provide an alternative for traditional wood residential floor systems. Steel framed floors are lighter, with high-strength and have less damping than traditional wood floors. However, lightweight floors will be more easily to vibrate under human activities, such as walking, running and jumping. The research on vibration behavior of cold-formed steel concretes composite floor due to walking in light-frame construction is carried out in this paper. Several acceptability criteria have been developed for such kinds of floor systems based on the static deflection of the floors. Onysko's criterion (CWC [1]) is based on the results of an extensive field study conducted in Canada. The survey involved the assessment of perceived acceptability of 646 floors in five cities of all types of wood construction. Great care was taken to obtain the subjective evaluation of the suitability of the floor from the homeowner, not the vibration performance. The study showed that the dynamic response due to an impact load and the deflection due to a static concentrated load were the two parameters that best correlated with perceived acceptability. In conjunction with a consortium of timber researchers and engineers, he has proposed a new design procedure for limiting vibrations of timber floors in the design stage. The method results in a value for span length, calculated from the fundamental properties of the floor and construction variables (i.e. sub-flooring type, glued or fastened flooring, spacing and bridging), which satisfies the deflection criterion. ATC Design Guide suggests the natural frequency of light-frame floor should be greater than 8Hz (ATC [2]). If the natural frequency is less than 8Hz, resonance occurs, the floor deflection under a point load of 1.0kN remains less than 2.0mm. Ohlsson's Criterion is applicable to all floor constructions (material independent) which have a lowest resonance frequency greater than 8 Hz (Ohlsson [3]). However, use of the method is limited to lightweight floors with span lengths less

than 6-8 meters. Resonance frequencies for a floor system are calculated assuming a simply supported rectangular orthotropic plate and have not taken into account composite behavior between the joists and flooring. This criterion also requires a check on the static deflection. The deflection of this single joist in a floor system is to be limited to 1.5mm under the action of a 1.0kN static concentrated load. The second requirement is a check on the response to an impulse load of 1.0N-s. The Australian Standard Domestic Metal Framing Code (AS3623 [4]) was developed for residential steel framed construction and uses much of the criterion proposed by Ohlsson. The dynamic serviceability requirements provided in this Code are limited to floors with a lowest natural frequency greater than 8 Hz. Two requirements are be used to assess the dynamic performance of a steel framed floor system. The first requires that under the application of a static concentrated load of 1.0kN anywhere on the floor, the floor deflection shall not exceed 2.0mm. The second requirement is likely to control in the design of long span floors, but guidance is not given as to what span lengths correspond to long span floors. Johnson [5] developed a design criterion for timber floors based on the results of 86 in-situ floors under construction. Johnson proposed that the fundamental frequency be greater than 15Hz for a floor supporting only its own weight. Typically, the fundamental frequency is calculated from a single joist in the floor system. However, if a girder is contributing to the response of the floor, the system frequency is taken as the fundamental frequency. In addition, Xu [6], and Kraus [7] put forward a different construction method to the floor frequency's effects. In this paper, an experimental study on vibration behavior of 4 full-scale cold-formed steel composite floors is carried out. The research of the fundamental frequency of composite floor, which considering the influence of screw space and rigid blocking under different loading cases during normal use is carried out in this paper. Then, a finite element analysis model of cold-formed steel composite floors is presented to study their vibration behavior.

2. SUMMARY OF TEST

2.1. Construction Details

The cold-formed steel composite floor is composed of cold-formed steel and sheeting-concrete composite slabs as shown in Figure 1. The joists of the floor are cold-formed steel with C section, and connecting with the boundary beams, which have U section, by self drilling screws through blocking. The spacing of the joists, which parallel to the wall studs, is 400mm or 600mm.

2.2. Specimens Design

Four composite floors, with consideration in the different spacing of self-drilling screws and the existence of the blockings, are designed in this paper (Figures 2 and 3). The specimens FL-1 and FL-2 have the same screw space type A as shown in Table 1. The difference of FL-1 and FL-2 is that there are rigid blocking between the joists in FL-2 and none in FL-1. The specimens FL-3 and FL-4 have the same screw space type B as shown in Table 1. And the difference of FL-3 and FL-4 is that there are rigid blockings between the joists in FL-4 but none in FL-3. The research on the fundamental frequency of composite floor, which considers the influence of screw spacing and rigid blocking under different loading cases during normal use, is carried out. The configurations of the specimens are described in Table 1.

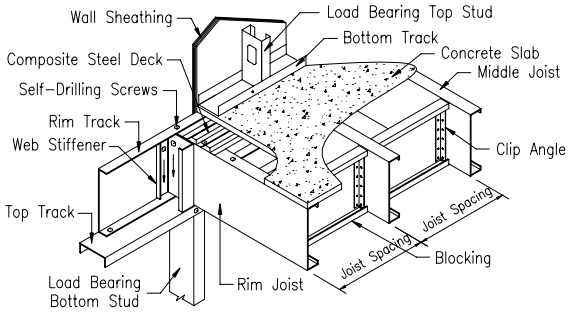

Figure 1. Details of Composite Floor

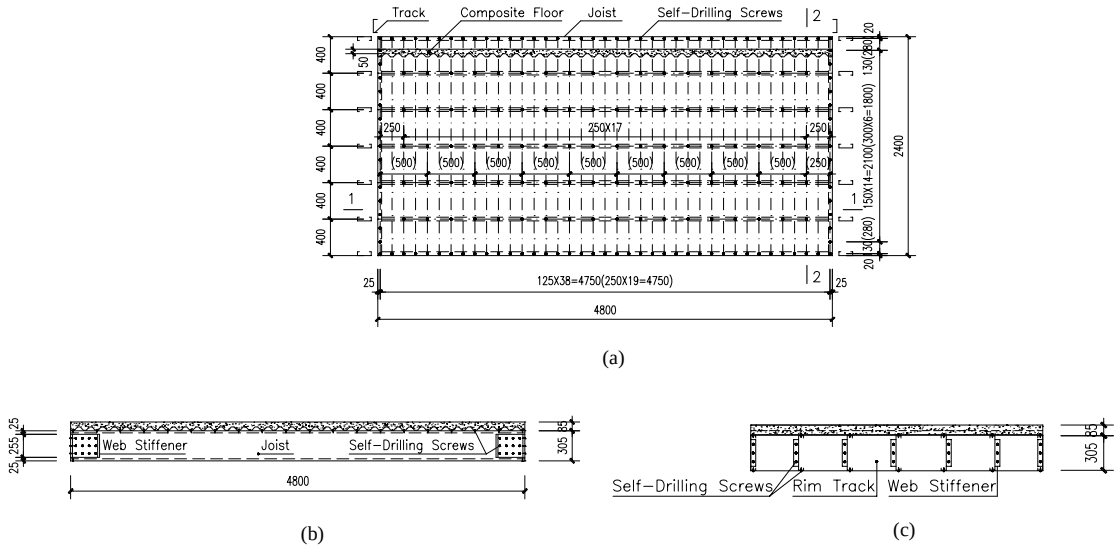

(a) (b) (c)

Figure 2. Construction Details of FL - 1(3):
(a) Layout Chart (The Data in the Bracket belong to FL-3); (b) Section 1-1; (c) Section 2-2

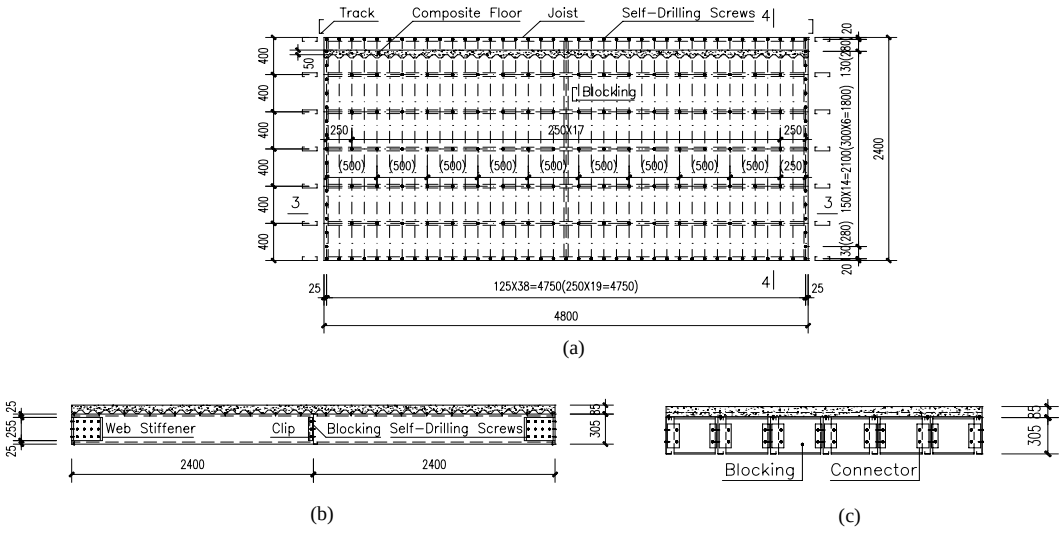

(a) (b) (c)

Figure 3. Construction Details of FL - 2(4):
(a) Layout Chart (The Data in the Bracket belong to FL-4); (b) Section 3-3; (c) Section 4-4

Table 1. Configuration of Specimens

SPECIMENS	LOAD CASES	SCREW SPACE /mm	BLOCKING	LIVE LOAD / N/MM^2	BEARING SUPPORT
FL-1	FL-1-A-1-A-0.0	A: 150mm along the direction of tracks, 125mm at the side joists and 250mm in the middle field of floor	A: No	0.0	1: Simple support
	FL-1-A -1-A-0.8			0.8	
	FL-1-A -1-A-2.0			2.0	
	FL-1-A -2-A-0.0			0.0	2: Fix support
	FL-1-A -2-A-0.8			0.8	
	FL-1-A -2-A-2.0			2.0	
FL-2	FL-2-A -1-B-0.0		B: Yes	0.0	1: Simple support
	FL-2-A -1-B-0.8			0.8	
	FL-2-A -1-B-2.0			2.0	
	FL-2-A -2-B-0.0			0.0	2: Fix support
	FL-2-A -2-B-0.8			0.8	
	FL-2-A -2-B-2.0			2.0	
FL-3	FL-3-B -1-A-0.0	B: 300mm along the direction of tracks, 250mm at the side joists and 500mm in the middle field of floor	A: No	0.0	1: Simple support
	FL-3-B -1-A-0.8			0.8	
	FL-3-B -1-A-2.0			2.0	
	FL-3-B -2-A-0.0			0.0	2: Fix support
	FL-3-B -2-A-0.8			0.8	
	FL-3-B -2-A-2.0			2.0	
FL-4	FL-4-B -1-B-0.0		B: Yes	0.0	1: Simple support
	FL-4-B -1-B-0.8			0.8	
	FL-4-B -1-B-2.0			2.0	
	FL-4-B -2-B-0.0			0.0	2: Fix support
	FL-4-B -2-B-0.8			0.8	
	FL-4-B -2-B-2.0			2.0	

Note: FL-1-A-1-A-0.0 denotes floor specimen FL-1, Screw spacing A, Bearing support 1, Blocking A, Live load 0.0 N/mm^2.

The framework of the composite floor is composed of 7 joists (C305×41×14×1.6mm) and 2 tracks (U307×35×1.6mm). The length of each joist is 4800mm, and that of track is 2400mm. The spacing of the joists is 400mm. The section of the seat blocking, which connects the web of joist and track by self-drilling screws, is C305×41×14×1.6mm with a length of 255mm. The section of blocking is C305×41×14×1.6mm and with a length of 380mm. The connectors are self-drilling screws and their numbers and arrangements are determined according to the Standard of China (JG/T 182-2005 [8]). The sheeting-concrete composite slabs are composed of profiled steel sheet and concrete with grade C30, whose thickness is 0.74mm and 50mm, respectively. The rib of slab is vertical to the joist, and connects to the flange of joist with self-drilling screws (4816). There are no shear resistance studs and reinforcing steel bars between the steel sheets and concrete.

According to the material experiments, it is known that the material properties of the specimens are as follows. the yielding strength of the cold-formed steel is 330.4 N/mm^2, Young's modulus is 2.17×10^5 N/mm^2, passion ratio is 0.3; and the yielding strength of the steel slabs is 382.43 N/mm^2, Young's modulus is 2.06×10^5 N/mm^2, passion ratio is 0.3; the standard compression strength of concrete is 23.9 N/mm^2, Young's modulus is 3.0×10^4 N/mm^2, passion ratio is 0.2.

The dimensions and loading cases of specimens are shown in Table 2. According to *Loading Code for the Design of Building Structures* (GB 50009-2001 [9]), 2.0 kN/m^2 is adopted as the live load in this paper; quasi-permanent value of the variable load is 0.8 kN/m^2 and 0.0 kN/m^2 when no live load is considered.

Table 2. Dimension of Specimens and the Comparisons of Test Results and Numerical Results

SPECIMENS	LOAD CASES	LENGTH /MM	WIDTH /MM	THICKNESS /MM	TEST FREQUENCY /Hz	FEM FREQUENCY /Hz	FEM /TEST
FL-1	FL-1-A-1-A-0.0	4800	2400	50	12.4	12.35	1.00
	FL-1-A -1-A-0.8				11.3	11.60	1.03
	FL-1-A -1-A-2.0				10.4	10.02	0.96
	FL-1-A -2-A-0.0				12.8	12.50	0.98
	FL-1-A -2-A-0.8				11.8	12.25	1.04
	FL-1-A -2-A-2.0				11.3	11.64	1.03
FL-2	FL-2-A -1-B-0.0	4800	2400	50	12.3	13.56	1.10
	FL-2-A -1-B-0.8				11.3	12.08	1.07
	FL-2-A -1-B-2.0				10.5	10.15	0.97
	FL-2-A -2-B-0.0				12.5	13.76	1.10
	FL-2-A -2-B-0.8				12.8	13.53	1.06
	FL-2-A -2-B-2.0				11.5	12.55	1.09
FL-3	FL-3-B -1-A-0.0	4800	2400	52	13.2	11.96	0.91
	FL-3-B -1-A-0.8				12.2	11.32	0.93
	FL-3-B -1-A-2.0				11.3	9.84	0.87
	FL-3-B -2-A-0.0				13.8	12.05	0.87
	FL-3-B -2-A-0.8				12.5	11.84	0.95
	FL-3-B -2-A-2.0				11.5	11.29	0.98
FL-4	FL-4-B -1-B-0.0	4800	2400	52	13.3	13.20	0.99
	FL-4-B -1-B-0.8				12.3	11.92	0.97
	FL-4-B -1-B-2.0				11.3	10.02	0.89
	FL-4-B -2-B-0.0				14.5	13.30	0.92
	FL-4-B -2-B-0.8				12.4	13.18	1.06
	FL-4-B -2-B-2.0				11.5	12.34	1.07

Note: Thickness is the actual value of floor.

2.3. Experiment Program

There are two kinds of supporting conditions for composite floor: simply supported slabs (Figures 4(a) and 5(a)) and rigid supported slabs (Figures 4(b) and 5(b)).

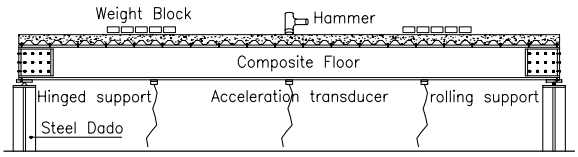

(a)

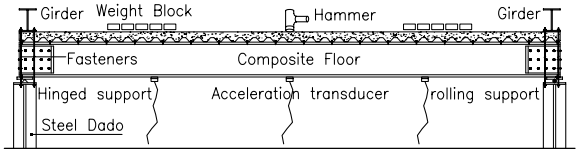

(b)

Figure 4. Test Set-up: (a) Simply Supported Slab; (b) Fix Supported Slab

Figure 5. Constraint Condition Setup: (a) Simple Support Boundary; (b) Fixed Support Boundary

As shown in Figures 4(a) and 5(a), the hinged support is adopted in one supporting boundary, and the other is rolling support. In order to simulate the rigid support boundary, a steel beam with weight of 205kg is used on one edge of the composite floor as shown in Figures 4(b) and 5(b), and the steel beam is tightly fixed to the dado. Many weight blocks are placed on the composite floor, in order to considering the influence of live load on floor as shown in Figure 6.

Figure 6. Weight Loading

The equipment for shock excitation is impact hammer. Many acceleration transducers are arranged on the bottom flange of the cold-formed steel joists, and they can record the dynamic response of the composite floor. All the test data were collected by LMS (Test. Lab Modal Impact) data collector. The measuring points of the acceleration transducer are shown in Figure 7. The measuring point 11 is shocking point.

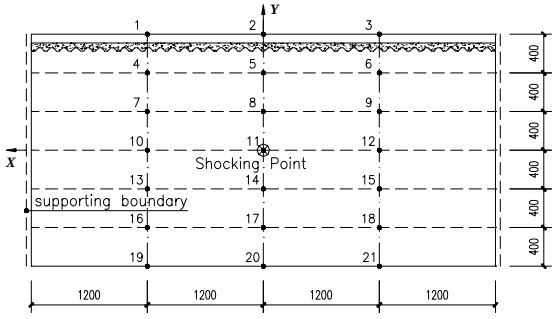

Figure 7. Layout of Measuring Points

2.4. Experimental Results and Analyses

The test results of fundamental frequency in different loading conditions are listed in Table 2. The fundamental frequencies of these given four specimens, which have the same length-width ratio but different structural mode, are more than 10Hz. There exist differences with the regulations in China code *Technical specification for Steel Structures of Tall Buildings* (JGJ99-98 [10]). However, they meet requirements that the vibration frequency of light floor should be over 8Hz presented in Refs. [2-4].

The fundamental frequency comparisons of these four specimens under different loading conditions are summarized as follows.

(i) With the increase of the floor live loads, the fundamental frequency of the specimens gradually decreases in the same constraint condition. It can decay to 3Hz.

(ii) The bigger the screw spacings of specimens FL-3(4) are, the bigger the fundamental frequency is. The largest difference between them is 1Hz. The fundamental frequency of thicker profiled steel sheet and bigger joist flange screw spacing is less than that of the smaller. The FEM results show that changing screw spacing can improve flexural rigidity of composite floors, which is the same with test results in Ref. [6]. With the decreasing of screw spacing, associative effects becomes more remarkable, also the flexural rigidity and vibration frequency become larger.
The causes for larger frequency are as follows, these four composite floors are site concreting in the process of fabrication. Because of the unevenness concrete surface and the difference of thickness, the mass of these four composite floors show an uneven distribution, and the real thickness of the floor has some difference with the design. So it shows the fundamental frequency becomes larger with the screw spacing increasing.

(iii) The profiled steel sheet and joist flange screw spacing of FL-1 is the same as FL-2, just like FL-3 as FL-4. The changing of rigid boundary has little effects on the frequency increasing of the composite floors. The corresponding fundamental frequency in different working conditions is basically identical to each other. The FEM shows the fundamental frequency of the composite floors with rigid blocking is somewhat larger than that without rigid blocking. Rigid blocking can not only improve the lateral stability of the joists, but also increase the flexural rigidity of the composite floors. The rigid blocking is always assembled after the joist frame emplacement. As the small torsion stiffness of the joists with open sections can easily lead to torsion deformation, and the construction space is also small, the installation precision and fastening degree of rigid blocking are always problems in practice, which become the obstacles to fully provide the lateral supports and improve greatly the flexural rigidity of the composite floors. This paper suggests using self-tapping screws instead of self-drilling screws, and setting flat steel belts to link the bolts at the joist bottom flanges.

(iv) The fundamental frequency become higher if the end restraints are enhanced in the corresponding working conditions. It shows steel beams simulating end restraint of the wall frame stud can limit the beam-end rotation, improve flexural rigidity of the composite floor, and increase frequency. The strength of the end restraint simulated by steel beams is related to the beam mass, fastening degree between beam and pedestal, and leveling degree. Therefore the improvement of measured fundamental frequency is not obvious.

(v) The acceleration response of the composite floors is related to energy under impact hammer effect. PSD means how the energy distributes in vibration frequency domain. The maximum of power spectrum density means the fundamental frequency of the composite floors. The acceleration and PSD in different measuring points are different, but the fundamental frequency and frequency domain are unrelated to different measuring points. The FL-1-A-1-C-0.0 measuring point distribution of PSD is showed in Figures 8 and 9. The Figures 8 and 9 include obvious peak value. Peak value always represents the fundamental frequency of the composite floors, which means most of energy concentrates in fundamental frequency limits.

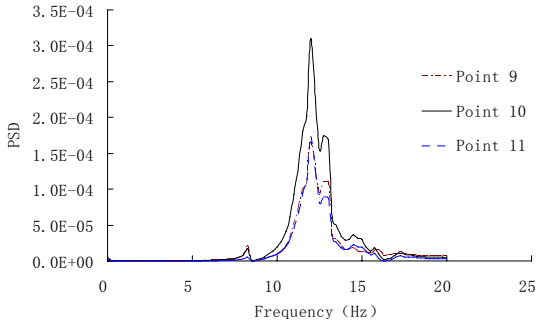

Figure 8. FL-1-A-C-0.0 along X-axis PSD

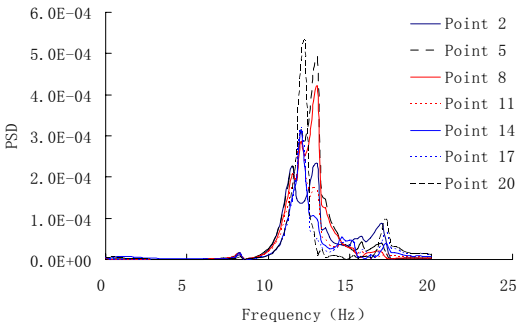

Figure 9. FL-1-A-C-0.0 along Y-axis PSD

As shown in Figure 8, the distribution value of PSD is changing with the measuring points varying. However, all the measuring points are distributed under one joist, so the PSD distribution forms are similar. Energy in point 11 is max, which gradually decreased far from impact point. The distribution value of PSD in different joists is a little different, shown in Figure 9, as the deformation of every joist is unified, when hammering on composite beams. Different structural composite beams have different PSD distribution forms and fundamental frequency, which is like FL-1-A-1-C-0.0.

In addition, we cannot feel vibration of composite floors when the author walks on the floor. However, when we hop on it we can feel a little vibration.

Former research [2 and 11] showed that, the most uncomfortable frequency of human response for residential housing stays in the range of 4-8Hz. And it was then provided that the fundamental frequency of the lightweight floor should be no less than 8Hz. However, resonance may also take place when the frequency of the pulse load is close to 10Hz if the span of the floor exceeds 3m. Based on this, the fundamental frequency of the composite floor under standard load combination in serviceability stage should not be less than 10Hz, the large vibration of the floor in serviceability stage can then be avoided. Therefore, in order to avoid resonance caused by walking and jumping, this paper suggests that the controlled fundamental frequency should be more than 10Hz, referred to the measured results and Refs. 2-4.

3. NUMERICAL STUDY

In order to compare with the test results of the finished four specimens in 24 kinds of loading cases, the numerical analysis is executed for each loading case of the composite floor by finite element program ANSYS. The following assumptions are used:

(i) Profiled steel sheets and concrete are completely bonded. The slip is not considered if there is any. The steel and concrete are considered to be elastic materials in numerical analysis.

(ii) The relative slip is allowed for the composite floor; profiled Steel Sheet-concrete composite floor and the flange of joists could impinge on the position of no screws under gravity load and live load.

(iii) The live load is converted to the equivalent density of floor board to consider its influence in the finite element analysis.

3.1. Finite Element Model

The plastic shell element SHELL181 is used to simulate the C-section joists, U-section tracks, profiled steel sheets, support stiffening members and rigid blockings, the element SOLIDE65 is used to simulate the concrete; the screws that connect the profiled steel sheets and the flanges of joists are simulated by element BEAM188. At the positions with no screws they are simulated by 3-D contact element CONTAC52; the screws among the support stiffening members, joists and tracks are simulated by coupling, the screws between rigid blocking and joist webs. When building a model, the real measured concrete thickness is used. The finite element models of composite floor are shown in Figure 10.

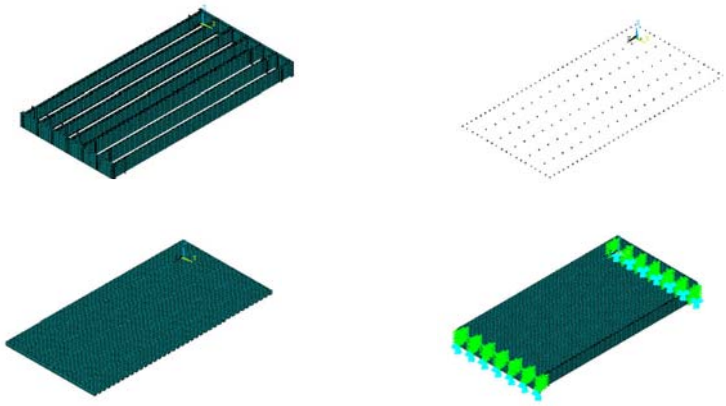

Figure 10. Finite Element Model of Composite Floor: (a) Joist;
(b) Self-drilling Screw; (c) Composite Floor; (d) Coupling

3.2. Results of Finite Element Model Analyses

The finite model analysis is executed for four specimens under 24 kinds of loading cases by finite element program ANSYS, the fundamental frequency of numerical simulation is shown in Table 2.

The numerical simulation method used by this paper can reflect the vibration behavior of composition floor exactly, and has high precision and calculation efficiency. The calculated fundamental frequency agrees well with experimental model fundamental frequency. The results between experiment and finite element simulation have some difference under individual loading cases because of the fabrication error of the specimens, the discrimination of boundary constraint, and the fastening degree of rigid support connections.

4. CONCLUSIONS

In this paper, the experimental research has been carried out for the vibration behavior of composite floor with different configuration modes, and by setting up numerical models the tested specimens have been analyzed with finite element program ANSYS. Comparison of the results from tests and finite element numerical analysis, the feasibility of precise frequency calculation by finite element program ANSYS is verified. The obtained results allow the following conclusions to be drawn.

(i) Under the same boundary constraints, the measured fundamental frequency of one specimen under different loading cases gradually decreases with the increase of floor live loads; the maximal attenuation is about 3Hz. The assumption that the live load is converted to the equivalent density of floor board in the finite element analysis is reasonable.

(ii) The flexural rigidity of composite floor can be improved by changing the spacing of screws. The fundamental frequency of composite floor with large spacing of the screws, that connect profiled steel sheets and the flange of joists, is smaller than the composite floor with small spacing. The lateral stability of joists can be strengthened and the flexural rigidity and frequency of composite floor will be increased by setting rigid blocking at mid-span of adjacent joist of composite floor. The fundamental frequency of composite floor is increasing if the end restraints are enhanced.

(iii) Different measuring points have different acceleration and PSD value, but the fundamental frequency and frequency domain are unrelated to different measuring points.

(iv) It is suggested that the construction quality should be strictly controlled and the fundamental frequency should be more than 10Hz.

ACKNOWLEDGEMENTS

This work was financially supported by the National Natural Science Foundation of China (Grant No. 50578013), College Doctor Foundation of Ministry of Education (No.20050710004), and the Fundamental Research Funds for the Central Universities of Hunan University, which are gratefully acknowledged.

REFERENCES

[1] CWC, “Development of Design Procedures for Vibrations Controlled Spans using Engineered Wood Members, Final Report Prepared for Canadian Construction Material Centre and Industry Partnership Consortium”, Canadian Wood Council, 1996.

[2] ATC, “Design Guide 1: Minimizing Floor Vibration”, Applied Technology Council Redwood, California, USA, 1999.

[3] Ohlsson, S.V., “Springiness and Human-Induced Floor Vibrations - A Design Guide - D12”, Swedish Council for Building Research, Stockholm, Sweden, 1988.

[4] AS3623, “Domestic Metal Framing Code”, Standards Association of Australia, Homebush, NSW, 1993.

[5] Johnson, J.R., “Vibration Acceptability of Floor Under Impact Vibration”, Department of Civil Engineering, Virginia Polytechnic Institute and State University, Blacksburg, Virginia, USA, 1994.
[6] Xu, L., Tangorra, F.M., “Experimental Investigation of Lightweight Residential Floors supported by Cold-formed Steel C-shape Joists”, Journal of Constructional Steel Research, 2007, Vol. 63, No. 3, pp. 422-435.
[7] Kraus, C.A., “Floor Vibration Design Criterion for Cold-formed C-Shaped Supported Residential Floor Systems”, Virginia Polytechnic Institute and State University, Blacksburg, Virginia, USA, 1997.
[8] JG/T 182-2005, “Technical Requirements for Low-Rise Assembled Residential Buildings with Light-Weight Steel Framing”, Wanfang Data Electronic Press, China, 2005.
[9] GB 50009-2001, “Load Code for the Design of Building Structures”, China Architecture & Building Press, Beijing, 2001.
[10] GJ 99-98, “Technical Specification for Steel Structure of Tall Buildings”, China Architecture & Building Press, Beijing, 1998.
[11] AISC, “AISC/CISC Steel Design Guide Series 11: Floor Vibrations due to Human Activity”, Chicago, 1997.